Emissive Langmuir Probe Theory with Application to Low Work Function Electrodynamic Tethers

by

Luca Chiabò

Thesis submitted in partial fulfillment of the requirements for the degree of Doctor in

Aerospace Engineering

Universidad Carlos III de Madrid

Tutor:
Prof. Gonzalo Sánchez-Arriaga

September 2022

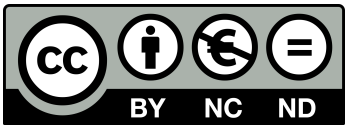

Abstract

Motivated by the need of mitigating the increase in the debris population that has been accumulating in the Low Earth Orbit (LEO) in more than 60 years of intense human activity in space, Electrodynamic Tethers (EDTs) have been proposed as efficient devices to deorbit satellites at the end of life. Consisting in long conductors that are deployed from the satellite at the end of its mission, EDTs exploit the interaction with the ionospheric plasma to create a current that, flowing along the device, interacts with the geomagnetic field giving rise to a magnetic drag that deorbits the satellite. Low Work-function tethers (LWTs) are particularly attractive because no expellant is needed for their operations. Once deployed, the LWT exchanges electrons with the ionospheric plasma, collecting them at one segment and, upon being coated with a material of low-enough work function, emitting them back at the complementary segment. Accurate models of the plasma-LWT interaction are necessary to quantify the performances of the device with software for mission analysis. Since the characteristic length of a space tether is several orders of magnitude larger than the Debye length in LEO, the current distribution along the tether can be computed from the current-voltage characteristic of a two-dimensional probe of same cross-section.

This dissertation presents a numerical investigation of the interaction between two-dimensional (electron-emitting) objects and Maxwellian plasmas representative of the LEO environment. A kinetic approach is adopted to study the features of the plasma sheath. In particular, a model based on the Orbital Motion Theory (OMT) is applied to study geometries that, although favourable for LWTs applications, received little attention in past works. To this extent, a novel stationary Eulerian Vlasov-Poisson solver based on a backward Liouville method is presented in detail. After a thorough verification procedure versus more mature numerical tools, a discussion of the physical and numerical limitations of stationary Vlasov-Poisson solvers is presented. Its results are used to provide a list of guidelines for their practical use in plasma-material interaction problems.

Using the same code, an analysis was carried out in order to characterise deeply the sheath around electron-emitting objects with elliptic cross sections. By varying the size, eccentricity and emission level of the probe, the study assessed the parameter domains for which Orbital-Motion-Limited (OML) current collection and Space-Charge-Limited (SCL) current emission hold. The local curvature of the probe revealed to have an important impact on its operational regime and, as compared with cylindrical ones, elliptic bodies were found to be more likely to meet non-OML and SCL conditions. Electron emission was also shown to be favourable for OML current collection. Regarding LWTs applications, an interesting equivalence between the emitted current in SCL conditions by ellipses and cylinders was found.

In the last part of the dissertation the hypothesis about the steady-state of the system is relaxed and a novel semi-Lagrangian Vlasov-Poisson solver developed as an extension of the stationary one is introduced. The impact of the population of trapped particles on the macroscopic magnitudes of the sheath is discussed. The results of a comparison between Eulerian solvers and a Particle-In-Cell (PIC) code for emissive probes are also presented to investigate the importance of the numerical noise of the PIC code. Particle trapping is shown to depend on both the history of the system and on the emission level. For high electron-emission, the trapped population reduces SCL effects.

Resumen

Ante el reto de mitigar el aumento de la población de basura espacial que se ha ido acumulando en la órbita terrestre baja (*Low Earth Orbit* - LEO) en los más de 60 años de intensa actividad humana en el espacio, las amarras electrodinámicas (*Electrodynamic Tether* - EDT) surgen como dispositivos eficientes para el desorbitado de satélites al final de su vida útil. Los EDTs, largos cables conductores, aprovechan su interacción con el plasma ionosférico para crear una corriente que, al fluir a los largo del cable, interactúa con el campo geomagnético y generan una fuerza de frenado que desorbita el satélite. Las llamadas *amarras con baja función de trabajo* (*Low Work-function tethers* - LWTs) son especialmente atractivas porque no involucran ningún consumible ni elemento activo para su funcionamiento. Una vez desplegado, el LWT intercambia electrones con el plasma ionosférico de manera totalmente pasiva. Los electrones son recogidos en un segmento llamado anódico y se emitien de vuelta al plasma en el segmento complementario catódico gracias a los efectos termoiónico y fotoeléctrico que facilitan el recubrimiendo con baja función de trabajo de la propia amarra. Para poder evaluar las prestaciones del dispositivo, se necesitan modelos precisos de la interacción entre el plasma y el LWT. Dado que la longitud de una amarra espacial es varios órdenes de magnitud mayor que la longitud de Debye en LEO, los perfiles de corriente y voltaje se pueden calcular a partir de las curvas características de una sonda bi-dimensional con la misma sección transversal.

La tesis presenta un analísis numérico de la interacción entre objetos bidimensional que emiten electrones y plasmas representativos del entorno espacial en LEO. Se adopta un enfoque cinético para estudiar las características de la vaina del plasma. En particular, se aplica un modelo basado en la *Orbital Motion Theory* (OMT) para el estudio de geometrías que, pese a ser ventajosas para aplicaciones de LWTs, recibieron poca atención en el pasado. Para ello se ha desarrollado un nuevo código Vlasov-Poisson euleriano y estacionario basado en el metodo de *backward Liouville*. Tras un extenso proceso de verificación frente a resultados obtenidos con código más maduros, se discuten las limitaciones de tipo físico y numérico intrínsecas a los códigos Vlasov-Poisson estacionarios. Los resultados se han utilizado para preparar una lista de recomendaciones prácticas sobre el uso de estos códigos en problemas de interacción plasma-material.

El código se ha utilizado para caracterizar en profundidad las vainas que se forman alrededor de objetos con sección transversal elíptica y que emiten electrones. En el análisis se ha variado el tamaño, la eccentricidad y el nivel de emisión del objeto, lo cual ha permitido determinar los dominios paramétricos en donde la captura de corriente está dada por la llamada teoría *Orbital Motion Limited* (OML) y la emisión ocurre bajo condiciones de *Space Charge Limited* (SCL). Se ha observado que la curvatura local de la

elipse juega un papel importante en determinar el regimen de operación y se encontró que los cuerpos elípticos son más propensos a cumplir con las condiciones de no-OML y SCL que los cilíndricos. También ha permitido concluir que la emisión de electrones favorece la captura de corriente en condiciones OML. Con respecto a los LWTs, se ha encontrado que existe un radio equivalente para calcular la corriente emitida por un cuerpo eliptico bajo condiciones SCL a partir de los resultados de un cuerpo cilíndrico.

La última parte de la tesis estudia los transitorios que ocurren entre una condición iniciales dada y el estado estacionario que se alcanza en el equilibrio. Para ello se ha desarrollado un código semilagrangiano para resolver el sistema Vlasov-Poisson no estacionario, el cual constituye una extensión del código estacionario usado en la primera parte de la tesis. El nuevo código ha permitido discutir el impacto de la población de particulas atrapadas en el transitorio sobre las magnitudes macroscopicas de la vaina del plasma en el equilibrio. Se presentan tambien los resultados de una comparación entre el código euleriano y un código *Particle-In-Cell* (PIC) para sondas emisivas con el fin de investigar la importancia del ruido numérico del código PIC. Se demuestra que la cantidad de atrapados depende tanto de la historia del sistema como del nivel de emisión. Para una alta emisión de electrones, la población de atrapados reduce los efectos SCL.

Acknowledgements

My first and most important thanks goes to my supervisor Gonzalo for giving me the chance to engage in one of the most fruitful and interesting experiences of my life. Interacting with such a capable and committed person has been an invaluable opportunity for my professional and personal growth. His constant support and guidance were indispensable for the achievement of this goal, and I am extremely grateful for it.

Secondly, I would like to thank Dr. Gian Luca Delzanno and the people of the plasma-material interface group at the Los Alamos National Laboratory for welcoming me and advising me during my stay there. I feel lucky to have had the possibility of interacting with them and learning from their great experience. A special mention goes to Pedro, without whose help I would probably be lost in the wilds of New Mexico by now.

I also take this opportunity to extend sincere thanks to Dr. Omar Leon from University of Michigan and Dr. Pierre Sarrailh of ONERA for the time dedicated to review the manuscript and for providing me with useful feedback and interesting ideas that improved the quality of the work.

My deepest thanks to all the people of the Aerospace Engineering Department at UC3M. Thank you for the fruitful interactions and for the time spent together inside and outside the university. A special mention goes to Gabriel, Sadaf and Samira for providing a friendly and relaxed atmosphere in the office, and to Xin, whose enthusiasm and knowledge helped me during my first months at the university.

Thanks to the *old* Italian friends for being exceptional companions during past, present and future steps of my life. I feel privileged to be surrounded by such extraordinary people. Being far from home becomes much less of a burden when you know that there is always somebody ready to greet you whenever you go back. A big thanks also the new friends met in Madrid, who truly enriched this experience with their presence. I am sure we will share more precious moments together in the future, no matter where we end up. A special mention to Ana and Rocco, much more than just roommates, for always making me feel at home.

Finally, I would like to dedicate this last paragraph to those who are my most important points of reference: my family. Thanks to my brother Michele for being a fundamental link between the Spanish and Italian realities. Thanks to my parents for being a constant source of support and inspiration. Although I know how difficult it is for you to have me so far from home, I do not remember a gesture or a word from you that was not in the interest of my happiness. I dedicate this work to you in the hope that it will make you proud.

This work was supported by PIPF Scholarship awarded on a competitive basis by Universidad Carlos III de Madrid. During the thesis I had the opportunity to participate in the European Union's Horizon 2020 Research and Innovation Programme under grant agreement No 828902 (E.T.PACK project) and the FET Innovation Launchpad project No 101034874 (BMOM).

Published and Submitted Contents

The following publications have been included in this thesis:

Journals

- **L. Chiabò**, S. Shahsavani, G. Sánchez-Arriaga,*Kinetic analysis of the plasma sheath around an electron-emitting object with elliptic cross section*, Physical Review E, Volume 104 (2021), 055204.
- **L. Chiabò**, G. Sánchez-Arriaga, *Limitations of stationary Vlasov-Poisson solvers in probe theory*, Journal of Computational Physics, Volume 438 (2021), 110366.

Other Research Merits

Journals

Although related, the following publications have not been included in this disseration:

- G. Sánchez-Arriaga, G. Borderes-Motta, **L. Chiabò**, *A Code for the Analysis of Missions With Electrodynamic Tethers*, Acta Astronautica, Volume 198 (2022), 471-481.

Conferences

Some of the results of the present work have been presented at the following conferences:

- **L. Chiabò**, G. Sánchez-Arriaga, P.A. Resendiz-Lira, G.L. Delzanno, *Impact of trapped particles on the plasma sheath around infinitely-long electron-emitting objects in Maxwellian plasmas*, 48^{th} EPS Conference on Plasma Physics (2022)
- **L. Chiabò**, G. Sánchez-Arriaga, *Plasma Sheath Around Long Conductors with Elliptic Cross-Sections*, 62nd Annual Meeting of the APS Division of Plasma Physics (2020).
- **L. Chiabò**, X. Chen, G. Sánchez-Arriaga, *Numerical Analysis of Tape-Like Low Work Function Tether Interaction with Ionospheric Plasma*, The Sixth International Conference on Tethers in Space (2019).

Software

The present work contributed to the development of the software *Free-Of-Noise Kinetic Solver for Generic Geometries (FONKS-G)*, with Autorship: **L. Chiabò 80%**, G. Sánchez-Arriaga 20%, and Owned by Universidad Carlos III de Madrid (UC3M). The code was registered in the *Registro Territorial de la Propriedad Intelectual de la Cominudad de Madrid* with number 16/2021/8105.

Projects

The present work contributed to the following international projects

- H2020 FET Innovation Launchpad No. 101034874, *Business Model for Modular Orbital Maneuvering kit (BMOM)*, European Commission, PI: Prof. G. Sánchez-Arriaga (Universidad Carlos III de Madrid), 01/05/2021-30/04/2022, 100k €.

- H2020 FET Open No. 828902, *Electrodynamic Tether Technology for Passive Consumable-less Deorbit Kit (E.T.PACK)*, European Commission, PI: G. Sánchez-Arriaga (Universidad Carlos III de Madrid), 01/03/2019-30/11/2022, 3M €.

International mobility

In partial fulfillment of the requirements for *Doctorado Internacional* distinction, the candidate carried out a research visit of the duration of 4 months at the *T-5 Theoretical Division (Pallied Mathematics and Plasma Physics)* of the *Los Alamos National Laboratory (LANL)* in New Mexico (USA), under the supervision of Dr. Gian Luca Delzanno.

Contents

List of Figures

List of Tables

Glossary

Acronyms

BCs	Boundary Conditions
BPT	Bare Photovoltaic Tether
CN	Crank-Nicolson numerical integrator
CPIC	Curvilinear Particle-In-Cell code
EDT	Electrodynamic Tether
EP	Emissive Probe
ESA	European Space Agency
E.T.PACK	Electrodynamic Tether technology for Passive Consumable-less Deorbit Kit
FDM	Finite Difference Method
FEM	Finite Element Method
FONKS-C	Free-Of-Noise Kinetic Solver for Cylindrical geometries
FONKS-G	Free-Of-Noise Kinetic Solver for Generic geometries
LEO	Low Earth Orbit
LF	Leapfrog numerical integrator
LP	Langmuir Probe

LWT	Low Work-fuction Tether
OML	Orbital Motion Limited theory
OMT	Orbital Motion Theory
PIC	Particle-In-Cell
RK	Runge-Kutta numerical integrator
SCL	Space Charge Limited
SLVP	Semi-Lagrangian Vlasov-Poisson solver
VP	Vlasov-Poisson

Symbols

a_p, b_p	Probe semi-major and semi-minor axes
c_p	Probe linear eccentricity
e_p	Probe eccentricity
e_α	Normalised charge of the α-species
f_α	Phase space probability distribution function of the α-species
I_α	Current per unit length of the α-species
j_{em0}	Current emitted per unit area consistent with a half-Maxwellian distribution function
j_α	Current per unit area of the α-species
j_α^{OML}	Current per unit area of the α-species given by the OML theory
k_B	Boltzmann constant
N	Total number of nodes in the space domain
$N_r,\ N_\theta$	Number of nodes along the polar coordinate directions

N_{tr}	Number of loops after which a particle is classified as trapped
N_x, N_y	Number of nodes along the Cartesian coordinate directions
N_ξ, N_η	Number of nodes along the elliptic coordinate directions
N_{χ^1}, N_{χ^2}	Number of nodes along the generic curvilinear coordinate directions
n_α	Density of the α-species
n_0	Background plasma density
p_Γ	Perimeter of the probe
p_θ	Angular momentum
$\boldsymbol{r}$, $\boldsymbol{v}$	Position and velocity vectors
r, θ	Polar coordinates
r_G^α	Larmor radius of the α-species
r_{SCL}	Fraction of the probe perimeter under SCL conditions
T_α	Temperature of the α-species
$v_{th\alpha}$	Thermal velocity of the α-species
x, y	Physical space coordinates
α	Identifies the charged species (subscript, superscript)
β	Probe emission level
Γ	Plasma-probe interface contour
Γ_{max}	Outer boundary of the computational domain
δ_α	Normalised temperature of the α-species
ε_α	Total energy of the α-species particles
ε_0	Electric permittivity of vacuum

ζ	Angle in the velocity space
κ_α	Kinetic energy of the α-species particles
λ_{De}	Debye length
μ_0	magnetic permeability of vacuum
$\xi,\ \eta$	Elliptic coordinates
ρ	Space charge density
τ	Non-dimensional time
ϕ	Electrostatic potential
ϕ_p	Probe bias
ω_{pe}	Electron plasma frequency

Chapter 1

Introduction

1.1 Background: the space debris problem

Dating back to 1957, the launch of the Sputnik 1 marked the beginning of the *Space Age* [1, 2]. Since then, human activities in space have constantly grown, driven by a thirst for knowledge and the will to improve the quality of life on Earth. This effort fostered progress in the understanding of the universe and enabled the development of life-changing services, like the Global Positioning System. In order to achieve such extraordinary outcomes, thousands of mission were designed and launched, leading to an exponential increase, which persists to these days, of the number of man-made objects in orbit. Figure 1.1, taken from the 2022 space environment report redacted by the European Space Agency (ESA) [3], shows that an estimation of more than 30000 objects is currently in orbit around the earth, the majority of which resides in a relatively small portion of the sky known as Low Earth Orbit (LEO), which extends approximately to an altitude of 2000 km. Most of these objects no longer serve any useful purpose and thus classifies as *space debris* [4, 5]. Their presence poses a severe problem to space operations, for a collision with an operative payload could result in serious damaging of the latter, potentially leading to a mission failure. As a side effect, new debris might form as well, thus polluting further the space environment and increasing the probability for more impacts to occur.

In fact, the amount of debris in orbit already reached a point where collisional break-ups could ignite a cascade of collisions provoked by their byproducts, resulting in an exponential increase of the debris flux in the long-term period. Under such circumstances, it appears clear how space operations could become highly risky, whether not totally unfeasible. The catastrophic scenario just discussed is known as *Kessler syndrome*, and was originally brought to attention in 1978 [6]. More recent studies based on numerical simulations have highlighted how the LEO environment is already unstable, with the population of debris estimated to continue growing even in absence of new launches [3, 7] (see Fig. 1.2). Obviously, this is not the case as the number of launches is increasing stably and will continue growing. For instance, the building of various *mega-constellations*

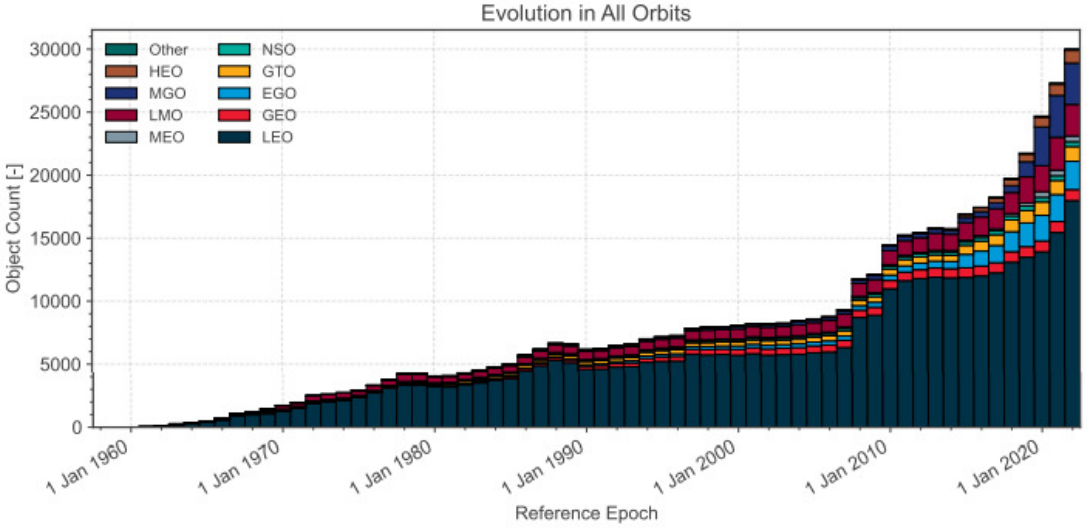

FIGURE 1.1: Number of objects in orbit around the Earth, classified according to their orbit [3]

in LEO is currently on-going, which will increase considerably the number of satellites in orbit around the earth in the next future [8].

In view of this, concern about the space debris issue has grown considerably in the recent past. In order to face the problem, space agencies worldwide have agreed upon several guidelines that outline a more sustainable operative framework for space activities [5]. Overall, their aim is to reduce the injection of new debris in orbit. To achieve this, new missions should be properly designed for minimising the release of debris during normal operations and being able to perform collision avoidance manoeuvres. In addition, proper post-mission disposal of the spacecraft should also be implemented either by moving it into a safe (*graveyard*) orbit or by deorbit. According the ESA report, the last years have recorded a positive trend towards compliance with such objectives. However, the population of debris is already so high that active debris removal is also deemed necessary as a complementary measure. In view of all the reasons mentioned above, several deorbiting technologies have been proposed, developed and/or are currently being investigated. Recent reviews about devices for active space debris removal can be found at [9, 10].

1.2 Electrodynamic Tethers

Among de-orbiting technologies, *Electrodynamic Tethers* (EDTs) represent an attractive alternative [11–17]. Their working principle is relatively simple: a long ($\sim 10^2 - 10^3$ m), narrow ($\sim 10^{-2}$ m) and thin ($\sim 10^{-6}$ m) conductor is deployed from a spacecraft at the end of its mission. If a stable current flows across the cable, the Lorentz force resulting from the interaction between the current and the magnetic field of the Earth acts as a drag that opposes the motion of the spacecraft with respect to the ambient plasma, thus

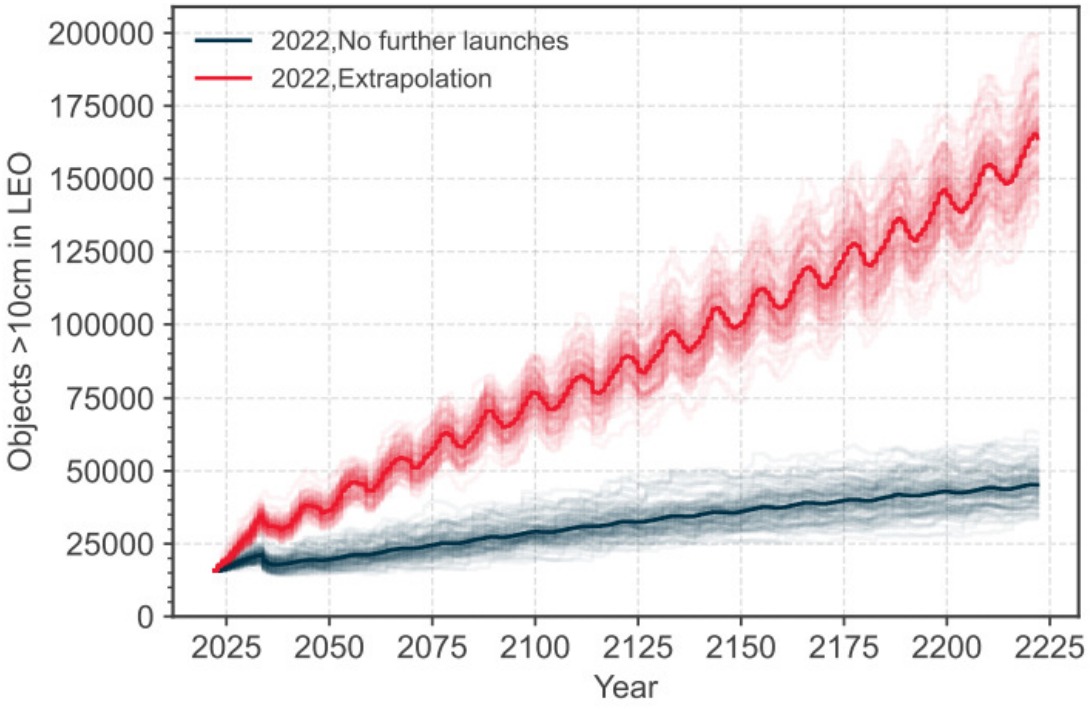

FIGURE 1.2: Forecast of the evolution of the number of objects in *stable launch rate* (red curves) and *no further launches starting from 2022* (blue curves) scenarios [3]

making it re-enter towards the atmosphere of the Earth, where it eventually burns (see Sec. 1.2.1 for more details). The history of the space tether concept goes long back [18] and different designs were proposed during more than 50 years of research (see Sec. 1.2.2). This section provides a detailed overview of the EDT technology, with particular focus on the so-called *Low Work-function electrodynamic Tethers* (LWTs).

1.2.1 Working Principle

Consider the system depicted schematically in Fig. 1.3. A long conductor is attached to a spacecraft orbiting at LEO altitude, where a plasma with a density of charged particles of the order of $\sim 10^{11}\,\mathrm{m}^{-3}$ is present. Being the plasma a conductor at equilibrium, the electric field $\boldsymbol{E'}$ measured from the frame of reference $\mathscr{F}'$ linked to it is zero. However, according to the transformations of Lorentz, at a frame of reference $\mathscr{F}$ moving jointly with the conductor an electric field equal to

$$\boldsymbol{E} \approx \boldsymbol{v}_{rel} \times \boldsymbol{B} \tag{1.1}$$

appears, with $\boldsymbol{v}_{rel}$ the relative velocity between the tether-S/C ensemble and the unperturbed plasma, and $\boldsymbol{B}$ the magnetic field of the Earth [19].

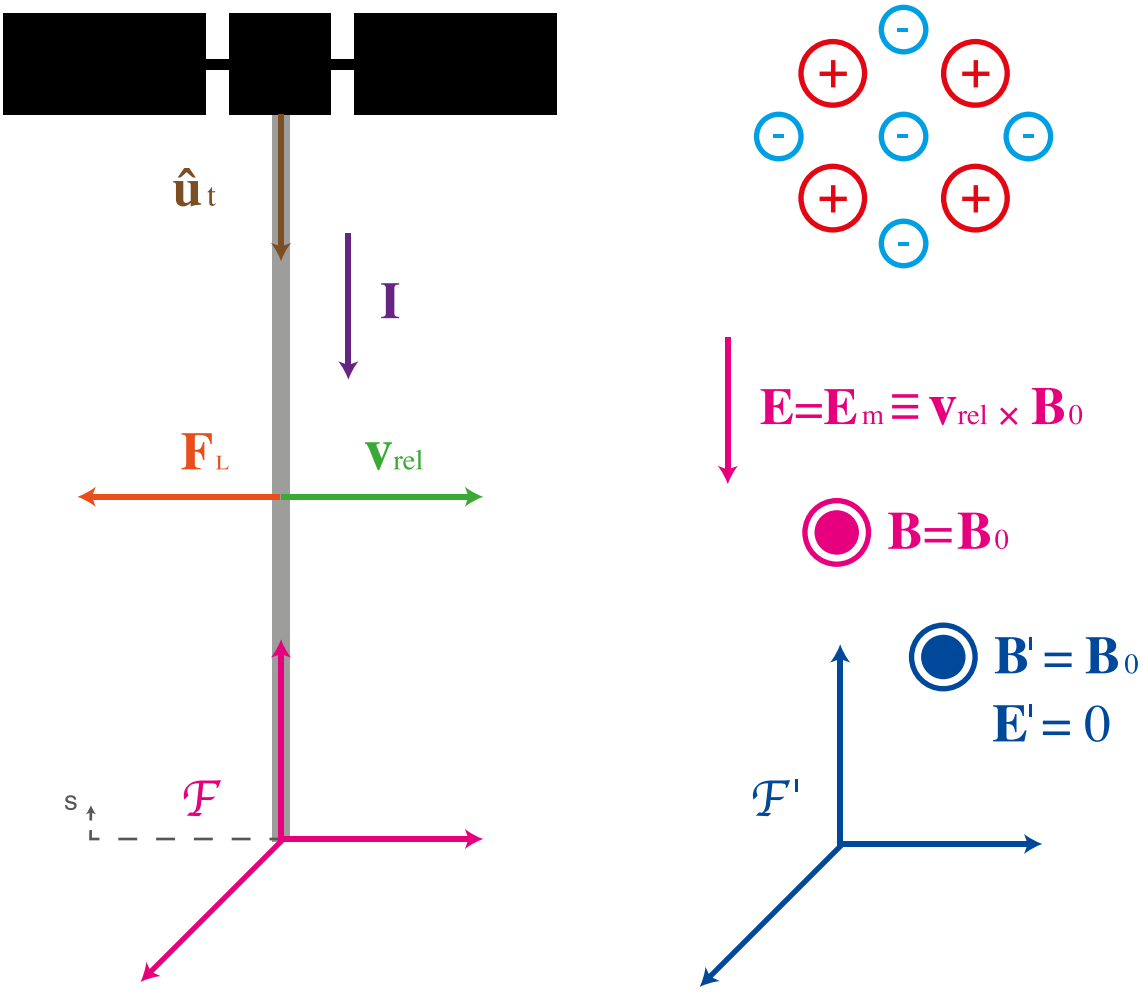

FIGURE 1.3: Sketch of the EDT working principle [20].

Equation (1.1) is valid upon assuming $|\boldsymbol{v}_{rel}| << c$, with c the speed of light. As observed by Drell et al. [18], such electromotive field causes the separation of charged particles in the direction normal to the $\boldsymbol{v}_{rel}$-$\boldsymbol{B}$ plane. If a low enough impedance exists between the plasma and the conductor (both anodic and cathodic), then a stable current $\boldsymbol{I}$ circulates along it. In presence of a magnetic field, the charged particles moving along the tether experience the action of the Lorentz force

$$\boldsymbol{F_L} = \int_0^L \boldsymbol{I}(s) \times \boldsymbol{B}\, ds, \tag{1.2}$$

where L is the total length of the tether and s identifies the coordinate along the tether direction. Acting as a magnetic drag, such a force can be exploited for deorbiting purposes. In order to provide an estimation of its effectiveness, it is necessary to compute the current per unit length along the tether, given by

$$\frac{dI}{ds} = p_t \cdot J(\phi). \tag{1.3}$$

where p_t is the perimeter of the tether cross-section, ϕ is the bias of the tether relatively to the faraway plasma and $J(\phi)$ identifies the current (per unit area) collected/emitted at a certain point along the tether. Since the characteristic dimension(s) of the cross-section for a cylindrical (tape) tether is (are) orders of magnitude lower than its length, and this is much bigger than the typical Debye length in LEO, $J(\phi)$ is equivalent to the current to a two-dimensional probe biased at potential ϕ with respect to the background plasma (see Secs. 1.3 and Chapter 2 for more details). The variation of the electrostatic potential profile ϕ along the tether reads

$$\frac{d\phi}{ds} = \frac{I(s)}{\sigma_t A_t} - E_m. \tag{1.4}$$

In Eq. (1.4), the first term corresponds to the drop of potential associated with the ohmic effects due to the presence of a flowing current and σ_t and A_t stand for the conductivity and the cross-sectional area of the tether, respectively. The second term $E_m \equiv \boldsymbol{E} \cdot \boldsymbol{u}_t$ is the variation of the potential at the faraway plasma, with $\boldsymbol{u}_t$ the unit vector tangent to the straight tether and along the direction of the electrical current. For a tether operating in LEO in the so-called *passive* mode, one has $\boldsymbol{E}_m \cdot \boldsymbol{I} > 0$.

Solving the system of Eqs. (1.3)-(1.4) with appropriate boundary conditions, which change accordingly to the type of tether, allows to describe the current and voltage profiles along the tether. Once these are known, the deorbit force that the device can exert is computed from Eq. (1.2). For the case of interest of a floating LWT (see Sec. 1.2.2.1 for details), one has $I(0) = I(L) = 0$. If a standard bare-EDT were to be considered, the second boundary conditions would become $V(L) = V_C < 0$, being V_C the potential drop at the active electron emitter.

While in a deorbit scenario the tether operates in passive mode, a second mode of operation can be achieved if an adequate source of power is available. In this latter case, the direction of the current (and therefore that of the force) can be inverted. In LEO, one gets $\boldsymbol{E}_m \cdot \boldsymbol{I} < 0$ and the tether generate thrust. Electrodynamics Tethers are thus completely reversible devices that can be exploited not only as a deorbit technology, but also as a propulsion system for re-boost manoeuvres and station-keeping purposes [21–26].

Regardless of the application, the performances of the tether clearly depend on the amount of current that the device is able to sustain. Providing a good electrical contact with the surrounding environment is thus of uttermost importance for an effective operative capability of the tether. In view of this, different architectures have been proposed and investigated, some of which were (and currently are) being tested in several missions. An historical overview of the development of space tether devices is given in the next section.

1.2.2 Historical overview

This section presents an overview of the main designs that have been proposed for EDT systems. A summary of the main missions, along with their successes and failures, that

were proposed and flown is also provided in order to furnish a thorough description of the state-of-the-art of the electrodynamic tether technology.

1.2.2.1 Tether design: from the origin to the the Low Work-function Tether

In more than half a century of research and experimentation, the design of EDT-based devices evolved dramatically in order to address critical technical aspects related to their concrete application [27]. The very first proposal of a device based on EDT technology dates back to 1965, when Drell et al. presented their *Alfén waves propulsion engine* [18]. In this first design, the electrical contact between the tether and the surrounding plasma was achieved by two large and passive conductors placed at the ends of a long insulated cable. Their corresponding impedance was computed by the authors based on Alfven radiation. A sketch of the device proposed by Drell et al. is depicted in panel (a) of Fig. 1.4.

The idea was surely intriguing but, just one year later, Moore pointed out that their computations were in fact too optimistic [28]. In order to overcome the difficulties related to provide a good electrical contact between the device and the ambient plasma, Moore proposed an alternative architecture featuring two active plasma contactors for electron collection and emission at the ends of the tether. This very configuration was implemented in the successful *PMG* mission, while the two *TSS* NASA missions in the first half of the 1990s (see next section for more details) tested a setup closer to that of the modern design of EDT devices. Such concept involved the use of a big collective sphere as the anodic contact, while at the cathodic end an electron gun would take care of returning the electrons back to the plasma [see panel (b) in Fig. 1.4].

In the early years, the main concern of the researchers working on EDT-based devices was that of guaranteeing a good electrical contact with the rarefied ionospheric plasma. In this regard, a revolutionary idea was brought about in 1993 by Sanmartin et al. [29]. In their influential work, the authors proposed to exploit the tether itself as an electron collector. By leaving a portion of the tether un-insulated, *bare* according to the terminology used in the paper, the device itself collects charged particles. Similarly to a (giant) Langmuir probe, the portion positively polarised with respect to the plasma collects electrons, while the portion of the tether negatively polarised receives the impact of positively charged ions. The huge collective surface resulting from the great length of the tether ($\sim 10^2 - 10^3$ m) provides an effective way of capturing charged particles that allows to get rid of active devices to fulfil this purpose. At the other tether end, electrons can be re-emitted into the ambient plasma by means of an active electron emitter (e.g., hollow cathode, thermionic emitter, etc..). In order to test this revolutionary device, whose sketch is presented in panel (c) of Fig. 1.4, a mission was proposed and developed but ultimately had to be canceled due to the outcomes of the accident of shuttle Columbia (see Sec. 1.2.2.2 for more details).

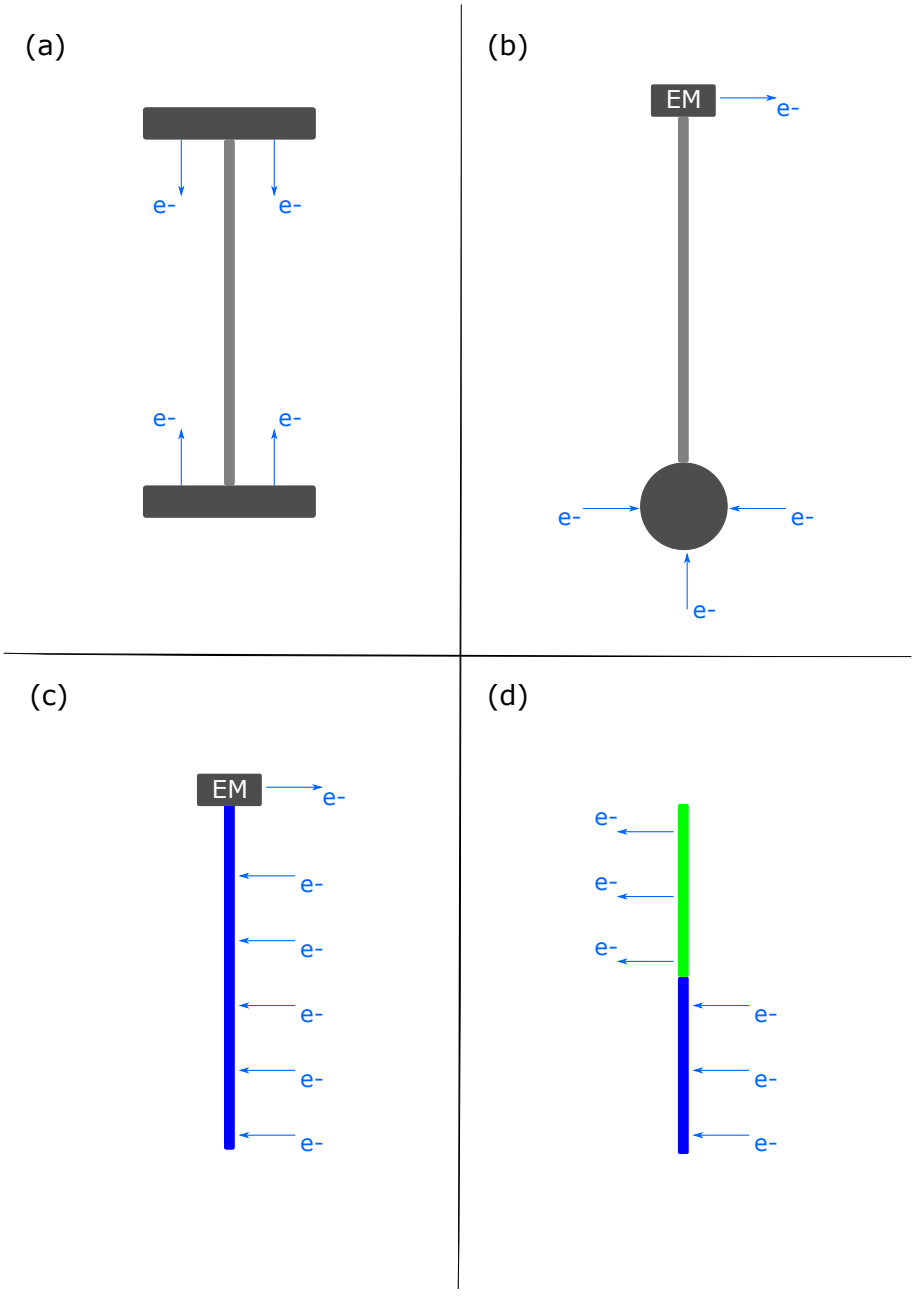

FIGURE 1.4: Sketch of different EDT-based devices: *Alfén waves propulsion engine* (a), TSS missions (b), *bare* electrodynamic tether (c), and *low work-funciton electrodynamic tether* (d) [27].

Despite this significant obstruction, interest in tether technology remained alive and further design innovations were introduced in the last 20 years. Regarding the electrodynamic model, a second revolutionary step in EDT-based concept occurred in 2012, when Williams and Sanmartin proposed to get rid of the active electron emitter by exploiting thermionic emission from the tether itself. This can be achieved if (a portion of) the tether is coated with a material of low-enough work-function [30]. According to the emissive mechanism proposed, the authors referred to this device as *thermionic EDT* [31]. In this newer version, the EDT is a completely passive device as no active element is needed, at least in the so-called *passive* (*generation*) mode that is of interest in de-orbit scenarios [32].

More recently, Sánchez-Arriaga and Chen pointed out how the photoelectric effect can enhance electron-emission by the coated segment of the tether, thus improving its effectiveness [33]. In view of the combined effects of *thermo-* and *photo*-emission, this latest version of the device is commonly referred to as *Low Work-function Tether* (LWT). A sketch of the latter is shown in panel (d) of Fig. 1.4, where the green portion of the tether represent the low W coating. In principle, the coating can extend to the whole tether. However, at the anodic end, the electrons emitted will be reflected and collected back by the tether due to the attraction of the electric field.

Unlike electric and chemical propulsion devices, which need for propellant and expellant in order to operate [17], LWTs could provide an affordable and convenient alternative to get rid of space debris and represent a potentially disruptive technology towards the achievement of a more sustainable use of the space environment. However, LWTs are a relatively new technology and their readiness is yet to be achieved. Currently, an important effort is carried out within the framework of *E.T.PACK*, a project funded by the European Commission that is aimed at pushing forward the LWT technology up to TRL 4 [27].

The analysis at the core of the present dissertation was carried out within the framework of E.T.PACK and its main target is the modeling of the interaction between LWTs and the ionospheric plasma (see Sec. 1.3), which is a key aspect for estimating the performances of the device. A better understanding of the mechanisms of current collection and emission is indispensable to improve the current models at the basis software for mission analysis of tethers, or at least to identify better the range of validity of the simplified ones that the latter implement [34].

For sake of completeness, it is worth mentioning that, as a side product of the investigation carried out in the E.T.PACK project, a novel architecture going by the name of *Bare-Photovoltaic Tether* (BPT) was proposed. Said concept, which is not discussed in the present dissertation, features a segment made of thin film solar cells to enhance the performances of the tether by providing an additional source of power [35].

1.2.2.2 Past and current tether missions

In order to provide an overview of the state-of-the art of space tethers, this section presents a brief summary of the most relevant missions involving the use of such devices. Despite the present dissertation focuses on the modeling of the LWT-plasma interaction, and its interest is thus limited to EDTs only, several missions featuring the use of non-conducting tethers are mentioned in order to present a thorough description of the maturity of the technology. In fact, they provide key information about aspects that, though falling beyond the scope of the present work, are relevant for EDTs (e.g., deployment mechanism and dynamics of the tether during the mission).

The first missions involving the use tethers in space date back to the early years of the space era. In the mid 1960s, the latest two missions of the *Gemini* program by NASA [36] were equipped with a non-conducting wire tether. Though several difficulties were experienced by the members of the crews, the two missions demonstrated the possibility of stabilizing a satellite with the use of a tether, either by exploiting the gravity-gradient or by rotating the system of two coupled spacecraft connected by the cable. The latter configuration proved also valuable for generating artificial gravity. During the 80s and early 90s, a series of suborbital experiments (*TPE, CHARGE, ECHO, OEDIPUS*) allowed to gather interesting information about the behaviour of the ionospheric plasma and its interaction with electron beams and the mitigation of charging induced by the release of gas. On top of that, these missions helped making progress towards the understanding of how to correctly perform the deployment of long tethers in vacuum and micro-gravity conditions [37, 38].

In the 1990s space tethers lived their so-to-speak *golden era*: interest in this technology was arguably at its top and several missions were launched in order to test it. The biggest two were undoubtedly *TSS-1* and *TSS-1R* by NASA, which flew in 1992 and 1996, respectively. They involved a quite complex system consisting of a satellite attached to a shuttle by a 20 km-long insulated wire tether. Their purpose was that of verifying the performances of the electrodynamic tether technology, studying its interaction with the ambient plasma and investigating the dynamics of the tethered system. After several problems experienced by TSS-1, during which the tether did not properly deploy, the system was flown again 4 years later. During TSS-1R, 19.7 km of the total 20 km of the tether were successfully and smoothly deployed, before the tether suddenly broke causing the satellite-tether ensemble to be lost to space. Post-mission analysis revealed that severance occurred in response to the formation of an electric arc that burned part of the tether, causing it to eventually break under the action of the tension. The arc resulted from a damage of the insulation caused either by some imperfection in the manufacturing or handling of the tether or by a debris [39].

Despite the mission could not be completed, the experiment is arguably far from being a failure. In fact, although the tether broke before its full deployment, this proceeded smoothly for several km. In addition, the duration of the mission allowed to collect numerous data regarding the electrodynamic characteristics of the system that proved the working principle of EDTs [40–45]. The experiment also helped improving considerably

the understanding of tether dynamics and the unforeseen loss of the system provided further evidence of the capability of the tether to stabilize itself along its local vertical, as observations of the severed system from Earth later confirmed.

On a smaller scale, several tethered missions were flown as secondary payloads attached to upper stages of launchers. Among these, both *SEDS-1* and *SEDS-2* were carried out successfully, further demonstrating the feasibility of the deployment and the vertical stabilization of the system through gravity-gradient. In 1993, the *PMG* mission involving a 500 m-long conducting tether was launched in order to prove that a current could be generated and exploited to create an electromagnetic drag (thrust) exploitable as a way of changing the orbit of a satellite without the use of propellant. During its 7 hours-duration, the mission successfully demonstrated that in the passive mode the tether was able to generate electrical power. Therefore, it proved that the total energy of the tether-satellite ensemble can be turned into electrical energy, causing the whole system to move to a lower orbit, which is the case of interest in a de-orbit scenario. On top of that, the experiment proved that the current was completely reversible and, provided an adequate amount of power is fed to the system, the tether can work in thrust mode [46–49]. A few years later the *TiPS* experiment proved a case against concerns about the safety of tether operations in space. Launched in 1997, the tethered device survived in orbit for more than 10 years without neither being severed nor posing a significant risk for other payloads.

Following the successful *SEDS* and *PMG* missions, the *proSEDS* experiment was designed in order to test the performances of the revolutionary bare-EDT concept, but the mission could not take place in view of the aftermath of the accident of the shuttle Columbia in 2003 [50–52]. Despite the numerous difficulties faced during some of the above-mentioned missions and the cancellation of proSEDS curbed the development of the EDT-technology, the interest remained alive and several missions, albeit smaller, were flown in the first decade of the 21^{st} century. Other worth-mentioning missions include the *YES* series of two experiments, the later of which holds the record for the longest tether ever deployed in space (31.7 km) and demonstrated the feasibility of de-orbiting of a spacecraft by exploiting momentum-exchange only. In 2010, the JAXA-sponsored mission *T-REX* performed the first deployment of bare tether with a tape cross-section and tested successfully the fast ignition of a hollow cathode immersed in the space environment [53].

Overall, the tethered missions that flew in the past gathered mixed results, which, despite all difficulties, proved that the working principle is solid and that the potential of the device is promising. In the last decade, it seems that enthusiasm towards EDTs has revived, also in view of new ideas that might bring significant improvements to the technology (e.g., the implementation of LWTs for a completely passive de-orbit system). Projects like E.T.PACK [27, 54] and missions such as *TEPCE* , *MiTEE*, *Prox-1*, *DE-SCENT* and *Dragracer* [55–66] provide a strong evidence of such renewed interest. The positive results of these latest efforts seem to suggest that in the near future this promising technology may finally see its full potential realized, thus providing a novel, sustainable and competitive alternative to the (for the time-being) more mature chemical and electric propulsion systems [17].

1.3 LWT-Plasma interaction modeling

The perfomarnces of EDTs as de-orbit or propulsion systems highly depend on their ability to exchange charged particles, electrons mainly, with the ionospheric plasma in which they are immersed. This interaction determines the amount of current that the device is able to sustain, which then affects directly the magnitude of the drag (propulsive) force according to Eq. (1.2). Reliable plasma-tether interaction models, which constitute a challenging problem in plasma physics, are thus indispensable for predicting accurately the behaviour of LWTs and carrying out an accurate design of missions through numerical simulations [34, 67–69].

In presence of an external body, the charged particles of a plasma arrange so as to shield such object-induced perturbation. The resulting *plasma sheath*, a region in which quasi-neutrality does not hold, governs the dynamics of the particles in the area surrounding the body and thus determines the amount of particles that are collected and/or emitted by it. Plasma sheaths come in a wide variety of forms (find reviews at [70, 71]) and the investigation of their features is a common problem in plasma physics that appear in a broad range of applications. In fact, although the present research starts from an interest in EDT devices [72–74], modelling of plasma-wall interaction has applications in many other fields such as Langmuir Probes (LPs) and Emissive Probes (EPs) for plasma diagnostics [75–81] and charging processes of dust grains [82–85] and spacecraft [86–89], to mention a few significant examples.

Typically, an accurate characterization of the plasma sheath requires the implementation of a *kinetic* approach. In the most general case, this demands for solving self-consistently the Boltzmann equation, which governs the evolution of the plasma species distribution function, coupled with the electromagnetic field provided by the Maxwell equations [90]. However, the plasma parameters characteristic of the ionospheric LEO environment, which is the case of interest for LWTs applications, allows to make several assumptions that ease the analysis. A common choice is that of disregarding the influence of collisions and the magnetic field on the dynamics of the charged particles (see Chapter 2 for more details). Further simplifications apply when objects of simple geometries such as planes, cylinders and spheres are considered.

Under such circumstances, the plasma-material interaction problem features symmetries that yield conservation laws (e.g., conservation of momentum or angular momentum of the charged particles). In turn, these can be exploited in order to find relatively simple models for the description of the sheath structure and the estimation of macroscopic magnitudes such as collected and emitted currents, or the charge of the object [91–105]. In addition, in the particular case of space tethers, their characteristic dimensions are such that, at different locations along the tether, their interaction with the plasma reduces to a two-dimensional problem. In other words, the current and voltage profiles along the tether [see Eqs. (1.3)-(1.4)] are equivalent to the current-voltage characteristics of a two-dimensional probe sharing the same cross-sectional shape of the tether and facing the same environmental conditions (i.e., the same plasma).

The previous discussion highlights how the electrodynamic performances of a LWT depend significantly on the geometry of its cross-section, which has also a high impact on the deployment and the storage of the tether [106]. Therefore, its selection constitutes a key aspect that needs to be addressed during the design of a mission. The model implemented to estimate the LWT-plasma interaction must thus follow from such a decision. Early tether designs implemented long conducting *wires* (i.e., round cylinders), which have been extensively investigated with the so-called *Orbital Motion Theory* (OMT). In this regard, a powerful and interesting result for current collection by bare-EDTs is the fact that the OMT retrieves the results of the simpler and very well-known *Orbital Motion Limited* (OML) theory introduced at [107]. The latter rests on the hypothesis that there are no potential barriers that would prevent some of the attracted particles from reaching the probe [108], thus representing a condition of maximum for current collection in absence of trapped particles. This is true at least when the radius of the tether is small enough with respect to the plasma Debye length [94]. At larger radii, the current collection diminishes and, when the bias of the probe is much bigger than that of the plasma, application of analytical corrections helps quantifying said reduction [109].

Despite being useful for estimating the current and voltage profiles along standard bare tethers, these results apply to non-emitting wires only, and are therefore not suitable for addressing the plasma-tether interaction at the the cathodic (emissive) segment of a LWT. Analysis of the latter requires taking into account emission of electrons at the plasma-material interface. Analytical models for cylindrical emissive probes have been proposed [100, 110, 111], (find a review in [112]). These analytical works help understanding the peculiarities of sheaths around emissive wires, such as the formation of a *virtual cathode* that gives rise to *Space-Charge-Limited* (SCL) emission, a condition in which part of the emitted electrons are reflected back to the probe by the opposing electric field. The application of analytical models is subject to the fulfillment of several hypotheses (e.g., cold and radially-moving ions, emission in vacuum). Relaxation of (some of) these hypotheses usually requires for the implementation of self-consistent numerical models. A recent one based on the OMT can be found at [113].

Unlike cylindrical probes, configurations involving an object with tape or tape-like cross-section immersed in a plasma have received little attention in past works. Arguably, this is in part due to the fact that the analysis is complicated by the absence of conserved quantities. For instance, moving from a cylindrical geometry to a tape one leads to the breaking of the axial symmetry of the problem. As a consequence, the angular momentum of the charged particles is no longer conserved along their collisionless orbits and analytical models for computation of their macroscopic quantities are therefore difficult to develop, unless special circumstances are considered.

However, as far as space tether applications in de-orbit or re-boost scenarios are concerned, numerous studies have highlighted how a tape geometry is favourable over a cylindrical one from a three-fold point of view. First, being the current per unit length proportional to the perimeter [see Eq. (1.3)], a tape shape guarantees higher performances as it maximises the perimeter for a given cross-sectional area (i.e., for a given mass). Second, a tape-like tether is more robust against impacts with small debris [114–116], thus

improving significantly the reliability of tethered devices. Eventually, the higher number of characteristic dimensions of a tape tether (length, width, thickness) versus a cylindrical one (length, radius) ensures a better scalability of the design, which can adjust better to the requirements of the mission [117]. Besides space tethers, interesting examples in which investigation of the plasma sheath around two-dimensional object with non-cylindrical cross-sections applies include charging of non-spherical dust grains [118] and applications related with plasma-sheath lenses [119–121].

Several works have dealt in the past with configurations involving objects with tape or tape-like cross-sections, although in a number significantly smaller compared to those addressing more regular geometries such as cylinders and spheres. For instance, a remarkable work by Laframboise and Parker showed that the current collection falls in the OML regime for *sufficiently convex* objects when a monotonic Laplacian potential is considered [108]. Further assessment of the validity of the OML theory in the limit of high bias was carried later out by Sanmartin and Estes, who first considered a thin taped cross-section [94], and then generalized their analysis to prisms of infinite length and arbitrary cross-section [122]. Once again, these analytical and semi-analytical models prove surely useful for understanding the current collection by LWT device, but their validity undergoes compliance to various additional hypotheses (e.g., high bias).

A more general description of plasma sheaths requires the implementation of numerical algorithms in order to relax some of the assumptions at the basis of analytical models. In the regime of plasma parameters suitable for LWTs, current collection by a tape was studied numerically with a direct *Vlasov-Poisson* (VP) solver in [123]. *Particle-in-cell* (PIC) codes are also a popular choice when it comes to the numerical investigation of plasma-material interaction, and have for instance been applied for studying the sheath around elongated dust grains in flowing plasmas [124]. A particle-particle code was also implemented for investigating the charging of non-spherical dust grains [125], and its results benchmarked again the analytical ones of Ref. [126].

Numerical simulations seem also to be the most appropriate tool to investigate the features of the sheath in presence of electron emission at the plasma-material interface. As discussed for the cylindrical case, electron emission further complicates the analysis of the sheath, since the additional population of electrons can significantly modify the electrostatic potential around the emitting body, thus altering the fluxes of charged particles. The above-mentioned appearance of a potential dip (virtual cathode) as consequence of the augmented population of electrons in the region surrounding a negatively biased object is a relevant example. Resulting in SCL emission, such feature is detrimental for the electrodynamic performances of a LWT. Since the low energetic electrons are reflected back to the tether by the reversal of the electric field, the presence of a potential well limits the amount of current that is effectively emitted by the cathodic segment. Longer tethers would thus be necessary to meet mission requirements in terms of current magnitude.

Understanding which conditions trigger the SCL operational regime, and quantifying how much this affects the overall performances of the LWT device is thus crucial for the proper design of a mission. Nonetheless, under such circumstances, deriving analytical

models is complicated. This is all the more true for a tape-like electron emitting body, as one can no longer exploit the conservation laws provided by the axial symmetry of the problem. If, for cylindrical emissive probes, a self-consistent numerical model based on the OMT has already been developed [113] and used to investigate the kinetic features of the sheath [127], there do not appear to be an equivalent analysis for the sheath around two-dimensional electron-emitting bodies with tape-like cross-section yet. The work presented here fills such theoretical gap between OMT for (emissive) probes with cylindrical [93, 113] and tape-like cross-sections [94, 123]. Its major objectives are summarized in the next section.

1.4 Research objectives

The present work aims at providing a solid description of the interaction between two-dimensional (electron-emitting) objects and the plasma environment faced by LWTs in de-orbiting scenarios. This is a relevant engineering problem that is motivated largely by the impending need to develop reliable and cost-effective technologies designed to guarantee a more sustainable use of the space environment. In view of the above considerations, the scope of the present work can be summarised in the following points

- Application of the Orbital Motion Theory to geometrical configurations that, despite having proven to be advantageous in LWTs application, and being of interest for applications ranging from plasma diagnostics to charging of spacecraft or dust particles, have received little attention in the past.
- Development and verification of a robust and versatile numerical tool to carry out the numerical analysis of the features of the plasma sheath that forms around electron-emitting objects with tape-like cross-sections are immersed in a LEO plasma.
- Analysis of different operational regimes through an extensive parametric analysis varying both the geometry of the configuration and the macroscopic properties of the background plasma. Particular attention is devoted to the investigation of the transition between the OML and non-OML regime for current collection, and that between non-SCL and SCL electron emission.
- Investigation of interesting physical features such as the appearance of chaotic dynamics and the subsequent filamentation of the distribution function, and their impact on the numerical solutions.
- Comparison between Eulerian and PIC solvers in the context of plasma-material interaction.
- Assessment of the role of trapped particles on the formation of the sheath in presence of electron emission at the plasma-material interface.

1.5 Disseration overview

The followings sections of the present thesis are presented as:

Chapter 2 - Stationary Vlasov-Poisson solver: Model and Numerical Algorithm introduces the mathematical model used to describe the stationary problem and justifies the introduction of the simplifying hypotheses. After the presentation of the mathematical equations that govern the problem and a discussion about the boundary conditions, the main blocks and the features of the numerical algorithm are described in detail.

Chapter 3 - Results of the Stationary Vlasov-Poisson solver summarises the main results of the investigation activity carried out with the stationary code. A first section discusses the verification of the novel code against previous numerical and analytical results. In a second part, a thorough analysis of the numerical properties of the code is presented. Both cylindrical and elliptical configurations are investigated in order to discuss some numerical and physical limitations that are inherent to the implementation of stationary Vlasov-Poisson solvers. Particular attention is dedicated to the ability of the code to recover conservation laws of the system, as well as to the rise of filamentation of the distribution function when moving from an integrable to a non-integrable configuration. Outcomes of such analysis are used to identify a set of good practices that are recommendable when developing a stationary direct Vlasov-Poisson solver. Eventually, the main results of a comprehensive study regarding the characterization of the sheath around (electron-emitting) elliptical bodies are presented, with particular focus on the assessment of the transition between different operational regimes.

Chapter 4 - Non-stationary Vlasov-Poisson solver outlines the mathematical model obtained by relaxing the stationary hypothesis previously taken into account. The main differences in the system of the governing equations and their normalisation are highlighted. A thorough description of the novel modules that had to be implemented to extend the stationary code is presented. Results of a first analysis assessing the impact of particle trapping on the sheath are discussed.

Chapter 5 - Conclusions and Future work summarises the main contributions of the thesis and provides a discussion of their relevance in the field of plasma physics and aerospace engineering. A brief mention of the future activities planned for continuing the research is also present.

Chapter 2

Stationary Vlasov-Poisson solver: Model and Numerical Algorithm

This chapter introduces[1] the mathematical model and the numerical algorithm developed to compute the structure of the steady-state sheath around a two-dimensional (emissive) object immersed at rest in a Maxwellian, unmagnetised, collisionless plasma. A *kinetic* description of the plasma is sought for by solving self-consistently the Poisson and Vlasov equations in order to obtain a discrete approximation of the continuous phase space distribution functions of the charged species. The latter are computed through a versatile numerical algorithm that was developed from scratch. By combining different numerical techniques, it can handle any kind of two-dimensional geometries, providing descriptions of different accuracy based on the necessities of the user. Exploiting the properties of the model, it reconstructs the discrete distribution functions onto an appropriately selected region of the phase space by applying the method of characteristics to the Vlasov equation. In practice, this involves integrating backward in time the orbits of the charged particles until they connect to a boundary of the computational domain where the distribution function is known (i.e., imposed as boundary condition). In previous works, such procedure was referred to as *inside-out* [123], but here the term *backward Liouville method* [130] is preferred as it highlights that it relies on the applicability of the *Liouville theorem*, which undergoes compliance with a certain set of hypotheses. The next section introduces one by one the assumptions of the kinetic model and derives the governing equations of the problem of interest, along with the appropriate boundary conditions.

2.1 Kinetic model of two-dimensional emissive probes

A plasma consists of a gas in which a significant number of electrically charged particles are present. If no external fields are taken into account, the charged particles interact

[1] The descriptions of the model and the numerical algorithm that follow are adapted from those provided in Ref. [128, 129].

among each others under the influence of the electromagnetic field consistent with their distribution. Therefore, the most fundamental description of the system would require solving Maxwell equations

$$\nabla \cdot \boldsymbol{E} = \frac{\rho}{\varepsilon_0}, \tag{2.1a}$$

$$\nabla \cdot \boldsymbol{B} = 0, \tag{2.1b}$$

$$\nabla \times \boldsymbol{E} = -\frac{\partial \boldsymbol{B}}{\partial t}, \tag{2.1c}$$

$$\nabla \times \boldsymbol{B} = \mu_0 \left(\boldsymbol{j} + \varepsilon_0 \frac{\partial \boldsymbol{E}}{\partial t} \right), \tag{2.1d}$$

self-consistently with the dynamics of each of the N_p charged particles

$$\frac{d\boldsymbol{r}_\alpha^i}{dt} = \boldsymbol{v}_\alpha^i, \quad m_\alpha \frac{d\boldsymbol{v}_\alpha^i}{dt} = q_\alpha (\boldsymbol{E} + \boldsymbol{v}_\alpha^i \times \boldsymbol{B}), \quad i = 1, 2, \ldots, N_p \tag{2.2}$$

In Eqs. (2.1)-(2.2), sub-index α identifies the species of the particle, $\boldsymbol{E}$ ($\boldsymbol{B}$) is the electric (magnetic) field, ε_0 (μ_0) the electric permittivity (magnetic permeability) of vacuum, ρ ($\boldsymbol{j}$) the charge (current) density, $\boldsymbol{r}_\alpha^i$ ($\boldsymbol{v}_\alpha^i$) is the position (velocity) vector of the i^{th}-particle and m_α (q_α) its mass (charge). Despite being achievable in principle, the number of particles involved in most phenomena is so huge that a discrete description taking into account the dynamics of each of the charges is not of practical interest, since it falls beyond the capabilities of present computational resources. A convenient alternative is implementing a *statistical approach* and representing the plasma species in terms of their continuous *distribution functions* in the position-velocity *phase space*. The latter identifies all the possible values of position and velocity of a particle, and the distribution function $f_\alpha(t, \boldsymbol{r}, \boldsymbol{v})$ represents the density of the particles of type α that are contained at time t in a certain region of the phase space. All the macroscopic quantities of interest that characterise a certain species (e.g., number densities, currents, temperatures, etc..) can be derived from their continuous distribution function. Adopting this *kinetic* description of a plasma, the unknowns of the problem become the distribution functions of the species, whose evolution is described, in the most generic case, by the *Boltzmann* equation

$$\frac{\partial f_\alpha}{\partial t} + \boldsymbol{v}_\alpha \cdot \nabla f_\alpha + \frac{\boldsymbol{F}_{tot}}{m_\alpha} \cdot \nabla_{v_\alpha} f_\alpha = \left(\frac{\partial f_\alpha}{\partial t} \right)_{coll}, \tag{2.3}$$

where $\boldsymbol{F}_{tot}$ is the total force, while $(\partial f_\alpha / \partial t)_{coll}$ represents a source term that measures the production/loss of charges due to collisions. Assuming external forces are absent (or negligible), the total force term that drives the dynamics coincides with the Lorentz force $F_{tot} = q_\alpha(\boldsymbol{E} + \boldsymbol{v} \times \boldsymbol{B})$, with $\boldsymbol{E}$ and $\boldsymbol{B}$ solutions of Eqs. (2.1).

Under appropriate circumstances, it is possible to apply some additional simplifications that facilitate the description of the sheath-formation, mainly by disregarding effects that are of little or no importance. Since it is the most interesting region for LWT applications, the present work focuses on plasmas that are representative of the LEO environment.

Table 2.1 summarises the values of the characteristic magnitudes of the plasma parameters that have been taken as reference in the present work.

LEO Plasma		
Magnitude	Symbol	Value
Background density	n_0	$\sim 10^{11}$ [m^{-3}]
Particles temperatures	$T_{e,i}$	$\sim 10^{-1}$ [eV]
Magnetic field	B_0	$\sim 10^{-1}$ [G]

TABLE 2.1: Typical values of plasma characteristic magnitudes in LEO [19, 90, 131–133]

The resulting *Debye length*, which identifies the characteristic length over which the shielding of the particles against perturbations of the equilibrium takes place, is approximately

$$\lambda_{De} \equiv \sqrt{\frac{\varepsilon_0 k_B T_e}{e^2 n_0}} \sim 10^{-2} \text{ [m]}, \tag{2.4}$$

with k_B the constant of Boltzmann and e the elementary charge. In a plasma, λ_{De} provides an indication of the extension of the non-neutral sheath and, in numerical analysis, it is a key parameter that need to be taken into account for the definition of an adequate computational domain, both in terms of extension and resolution. A second fundamental figure for the description of the behaviour of the system is the so-called *plasma parameter*

$$g \equiv \frac{3}{4\pi n_0 \lambda_{De}^3} \sim \frac{n_0^{1/2}}{T_e^{3/2}}, \tag{2.5}$$

which not only measures the number of particles contained in a *Debye sphere* (i.e., a sphere of radius λ_{De}), but also assesses the importance of collisional events inside the sheath. In fact, an increase in the unperturbed density n_0 implies a growth of the frequency of binary collisions among particles, while the opposite holds true for the temperature T_e. Therefore, in the limit $g \to 0$, collisions are rare enough to be neglected [19]. The plasma parameter is typically small for space plasmas and, for the reference conditions considered in the present work, one obtains $g \sim 10^{-5}$. Accordingly, the plasma is assumed to be *collisionless*. Dropping the term appearing at the right-hand-side of Eq. (2.3), the evolution of the distribution function obeys the *Vlasov* equation

$$\frac{\partial f_\alpha}{\partial t} + \boldsymbol{v}_\alpha \cdot \nabla f_\alpha + \frac{q_\alpha}{m_\alpha}(\boldsymbol{E} + \boldsymbol{v} \times \boldsymbol{B}) \cdot \nabla_{v_\alpha} f_\alpha = 0. \tag{2.6}$$

Appendix A in Ref. [93] discusses a limit condition for the validity of the approximation above. Summarising, quantitative and qualitative arguments show that a description of the

plasma based on the the Vlasov equation holds as long as

$$\frac{l_p}{\lambda_{De}} \leq \frac{9\pi}{g\ln(12\pi/g)} \sim 10^5, \tag{2.7}$$

where l_p identifies the characteristic length of an object immersed in the plasma. Since the present analysis deals with configurations such that $l_p/\lambda_{De} \approx 1$, one concludes that the results here presented fall well within the range of validity of the collisionless hypothesis.

The problem further simplifies if the influence of the magnetic field on the dynamics of the particles is negligible. In presence of a magnetic field, a charge moves along a helix resulting from the combination between a longitudinal motion (along the field line) and a circular motion (around the field line). The latter is characterised by the *Larmor radius* (*gyroradius*), defined for a particle of type α as

$$r_G^\alpha = \frac{m_\alpha v_\perp}{|q_\alpha| B}. \tag{2.8}$$

In the equation above, $v_\perp$ identifies the magnitude of the velocity in the plane perpendicular to the magnetic field line. Taking $|q_\alpha| = e$, and assuming that $v_\perp$ is of the order of the *thermal velocity* of the α-species

$$v_{th\alpha} \equiv \sqrt{\frac{k_B T_\alpha}{m_\alpha}}, \tag{2.9}$$

one can compute the typical values of r_G^α for the different species populating the ionosphere at LEO altitudes. After normalization against the Debye length, these are listed in Table 2.2, where the non-dimensional parameter $\mu_\alpha \equiv m_\alpha/m_e$ (i.e., the ion-to-electron mass ratio) is introduced as well.

Species	μ_α	r_G/λ_{De}
e^-	1	$\sim 10^1$
H^+	1836	$\sim 10^2$
O^+	29164	$\sim 10^2$

TABLE 2.2: Typical values of the Larmor radius (normalised to the Debye length) for the main components of a LEO plasma.

Since the Larmor radius is (at least) one order of magnitude bigger than λ_{De}, which provides a rough estimation of the extension of the sheath, one concludes that the magnetic field has little impact on the dynamics of the particles within the sheath. Table 2.2 features only hydrogen and atomic oxygen ions. However, for heavier molecules that can be found in the LEO ionosphere (e.g., NO^+ and O_2^+), the estimated larmor radius-to-Debye length ratio is even bigger as $r_G^\alpha/\lambda_{De} \sim \sqrt{\mu_\alpha}$. In addition, particles that accelerate in the sheath can acquire velocities that are several times their thermal one, resulting in a further increase of r_G^α.

Regarding the effect of the current-induced magnetic field on current collection, its possible relevance for space tethers applications was discussed in Refs. [134, 135], but was later shown to be negligible for most tether operational modes and designs in [136]. Therefore, it seems reasonable to consider the plasma as *unmagnetised* and to assume that the charged particles accelerate under the sole influence of the electric field. Subsequently, equation (2.6) becomes

$$\frac{\partial f_\alpha}{\partial t} + \boldsymbol{v}_\alpha \cdot \nabla f_\alpha - \frac{q_\alpha}{m_\alpha} \nabla \phi \cdot \nabla_{v_\alpha} f_\alpha = 0, \tag{2.10}$$

where the electric field $\boldsymbol{E}$ was expressed in terms of the electrostatic potential ϕ as

$$\boldsymbol{E} = -\nabla \phi. \tag{2.11}$$

Substituting the above equation in Eq. (2.1a), the electrostatic potential profile is determined upon solving the equation of Poisson

$$\Delta \phi = -\frac{\rho}{\varepsilon_0} \equiv -\frac{\sum q_\alpha n_\alpha}{\varepsilon_0}, \tag{2.12}$$

where the densities appearing at the right hand side are found from the self-consistent distribution functions through their integration in the velocity space

$$n_\alpha(\boldsymbol{r}) = \int_{-\infty}^{+\infty} f_\alpha(\boldsymbol{r}, \boldsymbol{v}) d\boldsymbol{v}_\alpha. \tag{2.13}$$

In the kinetic model just introduced, the plasma sheath obeys the non-linear system of partial differential equations given by Eqs. (2.10)-(2.11)-(2.12)-(2.13). Finding solutions requires imposing appropriate *boundary conditions* (BCs) that depend on the problem at hand. As anticipated in Chapter 1, the geometrical characteristics of a LWT allow to disregard three-dimensional end effects as the typical length of a space tether ($\sim 10^2 - 10^3$ m) is several orders of magnitude the Debye length in LEO ($\sim 10^{-2}$ m). Therefore, the configurations addressed in the present work feature a *two-dimensional* (emissive) object (probe, body) of contour Γ immersed in an unmagnetised, collisionless plasma. The conductive 2-dimensional body is kept at a fixed bias ϕ_p relatively to the unperturbed plasma. Due to its shielding effect, the plasma particles organize as to contain this body-induced perturbation and, beyond the limit of the sheath, the potential retrieves its unperturbed value. Following the previous reasoning, one imposes the following boundary conditions for the Poisson equation

$$\phi(\Gamma) = \phi_p, \quad \phi(|\boldsymbol{r}| \to \infty) \to 0, \tag{2.14}$$

with $\boldsymbol{r}$ the position vector measured in a frame of reference centred inside Γ. Regarding the background plasma, this is supposed to be populated by *Maxwellian* electrons and singly-charged positive ions with temperatures T_e and T_i and background densities $n_{e0} =$

$n_{i0} = n_0$. In presence of emission, *half-Maxwellian* electrons are emitted at the plasma-body interface with temperature T_{em} and density n_{em0}. Accordingly, at Γ one has

$$\begin{aligned} &f_{e,i}(\Gamma, \boldsymbol{v}\cdot\boldsymbol{u}_n > 0) = 0, \\ &f_{em}(\Gamma, \boldsymbol{v}\cdot\boldsymbol{u}_n > 0) = f_{HM} \equiv \frac{n_{em0} m_e}{\pi k_B T_{em}} \exp\left[-\frac{m_e}{2k_B T_{em}}(\boldsymbol{v}\cdot\boldsymbol{v})\right], \end{aligned} \tag{2.15}$$

with $\boldsymbol{u}_n$ the (outward) normal unit vector to Γ, while at an infinite distance from the probe one sets

$$\begin{aligned} &f_{e,i}(|\boldsymbol{r}| \to \infty, \boldsymbol{v}) = f_M \equiv \frac{n_0 m_{e,i}}{2\pi k_B T_{e0,i0}} \exp\left[-\frac{m_{e,i}}{2k_B T_{e0,i0}}(\boldsymbol{v}\cdot\boldsymbol{v})\right], \\ &f_{em}(|\boldsymbol{r}| \to \infty, \boldsymbol{v}) = 0, \end{aligned} \tag{2.16}$$

Together with the geometry of the plasma-material interface, the above BCs identify a set of governing parameters for the sheath described by the Vlasov-Poisson system. A sketch of the model described above is shown in Fig. 2.1.

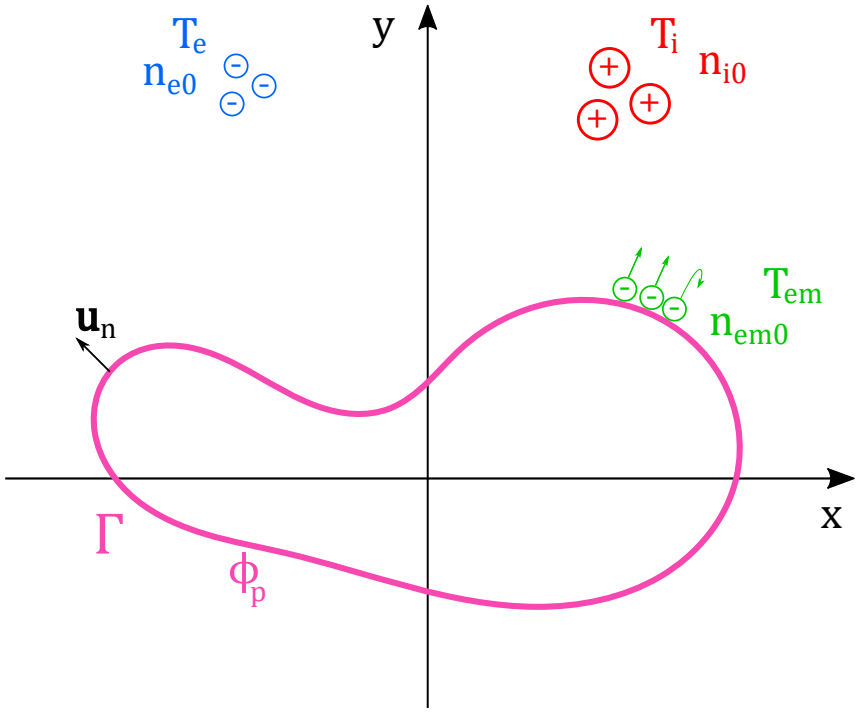

FIGURE 2.1: Sketch of the model for an arbitrarily-shaped electron-emitting probe of contour Γ immersed in a Maxwellian plasma

In a first approximation, the conductive object is assumed to be *at rest* with respect to the background plasma. Perhaps, this is the strongest hypothesis of the model as one may argue that neglecting relative motion is not a reliable representation for LWTs orbiting

around the Earth. Nonetheless, it is convenient to recall that the main purpose of the investigation is to characterise the current collection and emission by objects with tape-like cross-sections. The main novelty of the analysis resides in the geometry of the plasma-material interface and the model is tailored for a more fundamental analysis aimed at understanding the influence of the geometry on the mechanisms of current collection and emission. This allows to extend previous theoretical works (e.g., [113]) to a broader set of configurations, whose application is not restricted to LWTs. The presence of relative motion between the plasma and the object, and its impact on the current collection and emission, would not only bring further complications in the model, but also superimpose the effect of the cross-sectional geometry, making its influence less obvious. For this reason, it is neglected in the present analysis. However, it is clear that such investigation represents the natural continuation of the present research, and will be addressed in the next future. To this extent, Chapter 4 introduces the efforts that are currently being carried out to develop an appropriate algorithm for such analysis.

2.2 Stationary Vlasov-Poisson solver

Provided that a steady-state exists, it is possible to seek directly for the solution of the Vlasov-Poisson system disregarding the transient that leads to the equilibrium. In stationary conditions, the distribution functions $f_\alpha(t,\boldsymbol{r},\boldsymbol{v}_\alpha) = f_\alpha(\boldsymbol{r},\boldsymbol{v}_\alpha)$ do not depend on time and the Vlasov equation becomes

$$\boldsymbol{v}_\alpha \cdot \nabla f_\alpha - \frac{q_\alpha}{m_\alpha}\nabla\phi \cdot \nabla_{v_\alpha} f_\alpha = 0. \tag{2.17}$$

For convenience, one introduces the following dimensionless quantities

$$\begin{gathered}\frac{\boldsymbol{r}}{\lambda_{De}} \to \boldsymbol{r}, \quad \frac{\boldsymbol{v}}{\sqrt{2}v_{th\alpha}} \to \boldsymbol{v}, \quad \frac{n_{e,i}}{n_0} \to n_{e,i}, \quad \frac{n_{em}}{n_{em0}} \to n_{em}, \\ \frac{2k_B T_\alpha f_\alpha}{m_\alpha n_{\alpha 0}} \to f_\alpha(\boldsymbol{r},\boldsymbol{v}), \quad \frac{e\phi}{k_B T_e} \to \phi(\boldsymbol{r}),\end{gathered} \tag{2.18}$$

according to which the normalised Vlasov-Poisson system reads

$$\boldsymbol{v}_\alpha \cdot \nabla f_\alpha - \frac{q_\alpha}{2\delta_\alpha}\nabla\phi \cdot \nabla_{\boldsymbol{v}_\alpha} f_\alpha = 0, \tag{2.19a}$$

$$\Delta\phi = -\rho \equiv n_e + \beta n_{em} - e_i n_i. \tag{2.19b}$$

The equations above involve the dimensionless parameters

$$\delta_\alpha \equiv \frac{T_\alpha}{T_e}, \quad e_\alpha \equiv \frac{q_\alpha}{e}, \quad \beta \equiv \frac{n_{em0}}{n_0}, \tag{2.20}$$

which appear naturally upon introducing the normalization of Eq. (2.18). For a certain geometry of the plasma-material interface Γ and a given set of the parameters in Eq. (2.20),

a solution to the system of Eqs. (2.19a)-(2.19b) is defined by imposing the boundary conditions previously discussed. In dimensionless form, they read

$$\begin{gathered}\phi(\Gamma) = \phi_P, \quad \phi(r \to \infty) \to 0 \\ f_{em}(\Gamma, \boldsymbol{v}\cdot\boldsymbol{u}_n > 0) = f_{HM} \equiv \frac{2}{\pi}\exp\{-(\boldsymbol{v}\cdot\boldsymbol{v})\}, \quad f_{em}(r\to\infty, \boldsymbol{v}) = 0 \\ f_{e,i}(\Gamma, \boldsymbol{v}\cdot\boldsymbol{u}_n > 0) = 0, \quad f_{e,i}(r\to\infty, \boldsymbol{v}) \to f_M \equiv \frac{1}{\pi}\exp\{-(\boldsymbol{v}\cdot\boldsymbol{v})\}.\end{gathered} \tag{2.21}$$

In the stationary case, the structure of the sheath is therefore found by solving numerically the system of Eqs. (2.19a)-(2.19b) with the BCs of Eq. (2.21). To this purpose, the present analysis exploits a novel *stationary Eulerian Vlasov* solver whose main blocks and operations are summarised in the diagram of Fig. 2.2. The code, named *Free-of-Noise Kinetic Solver for Generic geometries* (FONKS-G), is based on a *backward Liouville method* [130]. It implements backtracking of the characteristic curves of the Vlasov equation, along which the distribution function is conserved in a collisionless plasma [137], to infer the value of the distribution function onto a discrete representation of the phase space (see Sec. 2.2.3 for more details).

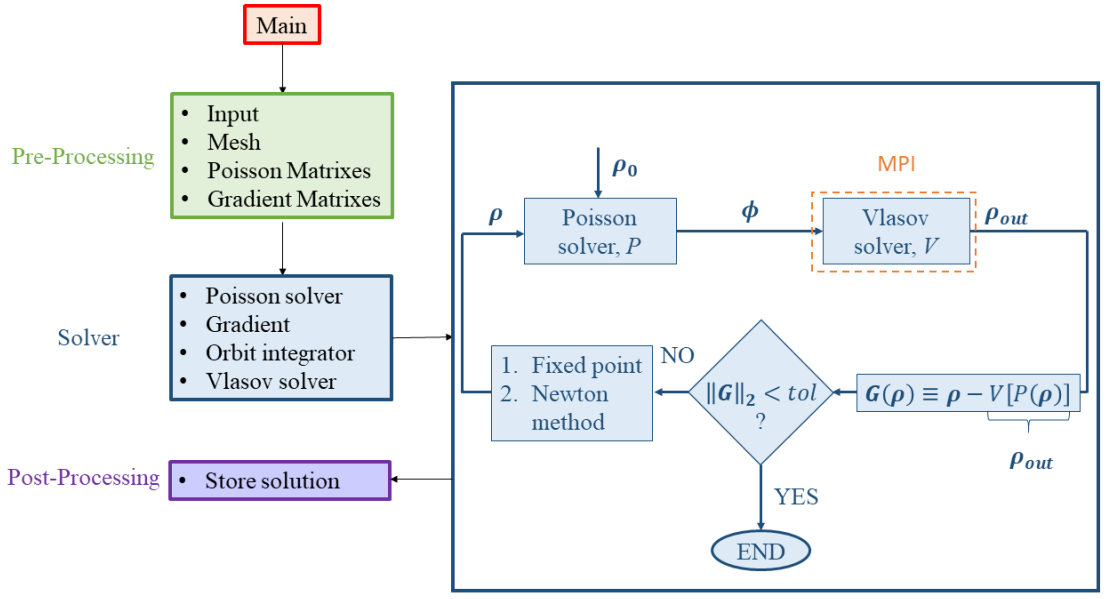

FIGURE 2.2: Flow chart of FONKS-G

Unlike the more popular and widely used PIC codes [138–140], Eulerian solvers discretise the distribution function directly in the phase-space domain and are thus free from the macro-particle-induced statistical noise. Despite being computationally more expensive than their particle-based counterpart, direct Vlasov solvers constitute a convenient choice when seeking for a detailed description of the plasma sheath and the fine structures of the distribution function [141–143], and have been used in a wide variety of applications

[144–151]. The present numerical algorithm is written in *Fortran* [152] and, in addition to routines written from scratch and some adapted from *Numerical Recipes* [153, 154], it implements *MPICH* [155, 156] and *HDF5* [157, 158] libraries to handle parallelised tasks and input/output operations, respectively. The next sections describe in detail its main features.

2.2.1 Computational domain

The code computes self-consistently the structure of the plasma sheath onto a computational domain bounded by the probe contour Γ (inner boundary) and the external (outer) plasma boundary Γ_{max}. In order to allow for quasi-neutrality to be recovered, the latter must be located far enough away from the plasma-body interface so that the body-induced perturbation becomes negligible and the plasma reaches its unperturbed equilibrium. The results of the present work focus on the characterization of the sheaths around cylindrical and elliptical probes immersed at rest in a Maxwellian plasma. Under these circumstances, the problem is symmetrical with respect to both Cartesian axes and, for a generic magnitude of interest $h(x,y)$, it holds that $h(x,y) = h(-x,y) = h(-x,-y) = h(x,-y)$. Therefore, the computational domain is restricted to the first quadrant only, which allows a higher resolution for a given computational cost.

According to the geometry of the probe, the domain is discretised either with (i) an unstructured mesh in Cartesian coordinates (x,y), or (ii) a structured mesh in appropriate curvilinear coordinates (χ^1,χ^2). When using unstructured meshes, these are created prior to the simulation with the open-source software *GMSH* [159]. Typically, the N nodes located at the vertices of the first-order triangular elements are distributed non-uniformly across the domain. Specifically, the density of the nodes is higher closer to the plasma-probe interface, where bigger gradients occur, while the mesh gets coarser towards the outer boundary. Together with freedom in distributing efficiently a higher amount of nodes where necessary, another advantage of unstructured meshes is that they can adjust easily to any kind of geometry, including the most complicated. For the rather simple cylindrical and elliptical probes considered in the present analysis, the inner and outer boundaries of the domain in Cartesian coordinates are defined as

$$\begin{aligned}\Gamma &= \{(x,y) \mid (1-e_p^2)x^2+y^2 = b_p^2,\ 0 \le \arctan(y/x) \le \pi/2\} \\ \Gamma_{max} &= \{(x,y) \mid r \equiv \sqrt{x^2+y^2} = r_{max},\ 0 \le \arctan(y/x) \le \pi/2\},\end{aligned} \tag{2.22}$$

where e_p and b_p are the eccentricity and the semi-minor axis (normalized with the Debye length) of the ellipse describing the plasma-material interface, respectively. The top-left panel in Fig. 2.3 shows an example of an un-structured mesh used to discretise the computational domain around an elliptical probe of $e_p = 0.95$. Despite its versatility, discretisation through unstructured meshes implies a more expensive procedure for the integration of particle orbits (see App. D.2) and has a negative impact on the capability of the code to preserve conservation laws, as discussed in Sec. 3.2.

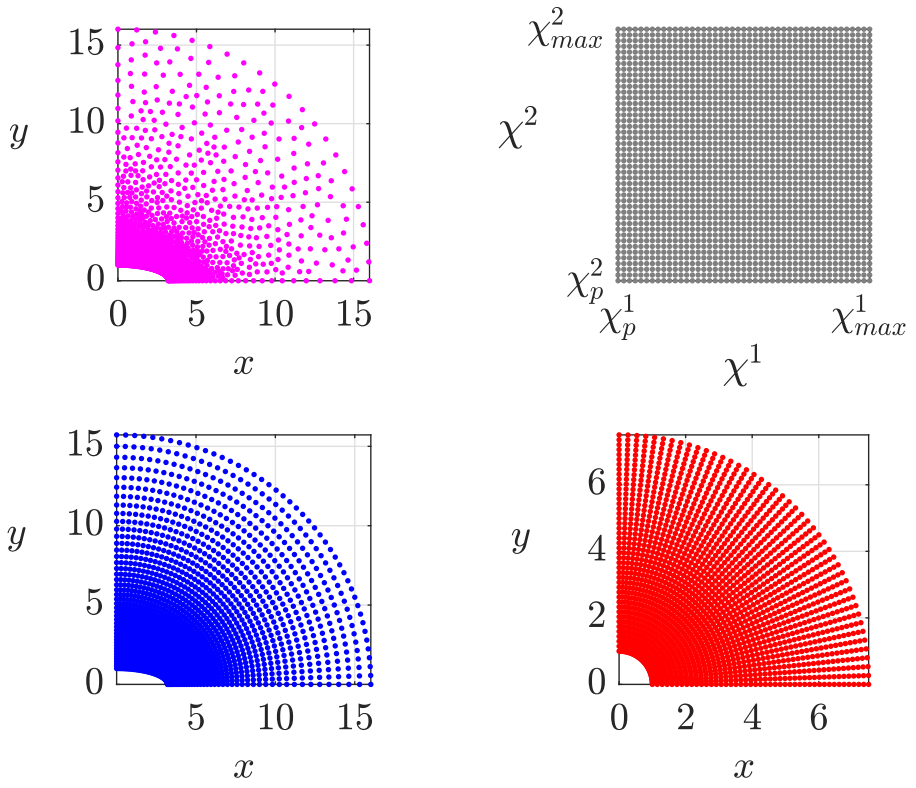

FIGURE 2.3: Examples of computational domains for ellitpic and cylindrical probes: unstructured mesh in physical space (top-left), structured mesh in logical space (top-right), elliptical structured mesh in physical space (bottom-left), cylindrical structured mesh in physical space (bottom-right) [128].

Structured meshes represent a valuable alternative for obtaining simpler and more efficient implementations, and are particularly attractive when the configurations of interest feature a fairly regular geometry. If the latter is curved, an appropriate change of variables is required in order to map the physical space (x,y) onto a Cartesian grid in the *logical space* (χ^1,χ^2), which is discretized onto $N = N_{\chi^1} \times N_{\chi^2}$ nodes (see top-right panel in Fig. 2.3). For the elliptic probes addressed in the present work, one introduces the elliptical coordinates $(\chi^1,\chi^2) = (\xi,\eta)$, which provide the following map

$$x(\xi,\eta) = c_p \cosh\xi \cos\eta, \quad y(\xi,\eta) = c_p \sinh\xi \sin\eta. \tag{2.23}$$

In Eq. (2.23), $c_p \equiv e_p b_p/\sqrt{1-e_p^2}$ is the *linear eccentricity* and the lines $\xi = constant$ and $\eta = constant$ identify confocal ellipses and hyperbolae, respectively. The computational domain is bounded by the region $\xi \in [\xi_p, \xi_{max}] \times \eta \in [0, \pi/2]$ in the logical space, where

ξ_p and ξ_{max} represent the plasma-probe interface and the unperturbed plasma boundary

$$\begin{aligned}\Gamma &= \{(\xi,\eta) \mid \xi = \xi_p,\ 0 \leq \eta \leq \pi/2\},\\ \Gamma_{max} &= \{(\xi,\eta) \mid \xi = L_\xi \times \xi_p = \xi_{max},\ 0 \leq \eta \leq \pi/2\},\end{aligned} \tag{2.24}$$

with the scalar L_ξ selected high enough to guarantee that quasi-neutrality holds at Γ_{max}. The bottom-left panel of Fig. 2.3 shows how the structured mesh in the top-right panel of the same figure looks in the physical (Cartesian) space after applying the elliptical map of Eq. (2.23) to a configuration with $e_p = 0.95$, $b_p = 1$ and $L_\xi \approx 7.25$. For cylindrical probes (i.e., $e_p = 0$), the code uses polar coordinates $(\chi^1, \chi^2) = (r, \theta)$

$$x(r,\theta) = r\cos\theta, \quad y(r,\theta) = r\sin\theta. \tag{2.25}$$

In this case, the computational box is delimited by $r \in [b_p, r_{max}] \times \theta \in [0, \pi/2]$, where b_p represents the normalized probe radius and the boundaries are defined as

$$\begin{aligned}\Gamma &= \{(r,\theta) \mid r = b_p,\ 0 \leq \theta \leq \pi/2\},\\ \Gamma_{max} &= \{(r,\theta) \mid r = r_{max},\ 0 \leq \theta \leq \pi/2\}.\end{aligned} \tag{2.26}$$

The structured cylindrical domain corresponding to $b_p = 1$ and $r_{max} = 7.5$ is shown in the bottom-right panel of Fig. 2.3.

2.2.2 Poisson Solver $\mathscr{P}$

Being one of the main two blocks of the numerical algorithm, the Poisson solver $\mathscr{P}$ represents the set of operations that are carried out in order to solve numerically Eq. (2.19b). Provided as input the charge density vector $\boldsymbol{\rho} \in \mathscr{R}^N$, the Poisson solver returns the corresponding electrostatic potential profile at the N nodes of the mesh. In matrix form it reads

$$\boldsymbol{\phi} = \mathscr{P}(\boldsymbol{\rho}) = \bar{\boldsymbol{A}}\boldsymbol{\rho} + \boldsymbol{\phi}_{BC}, \tag{2.27}$$

with matrix $\bar{\boldsymbol{A}} \in \mathscr{R}^{N\times N}$ and vector $\boldsymbol{\phi}_{BC} \in \mathscr{R}^N$ depending on the properties of the mesh and the boundary conditions. Regarding the latter, condition $\phi(r \to \infty) \to 0$ must be replaced properly in order to keep the computational domain finite and, possibly, at a reasonable size. In this regard, two alternative solutions are implemented in the code. The first one consists simply in displacing the zero of the electrostatic potential to a location which is deemed far enough away from the plasma-probe interface such that the value of the potential relative to the unperturbed plasma be negligible there [i.e., $\phi(\Gamma_{max}) \approx 0$]. Despite being straightforward to implement, this rather simple choice can require considering relatively a big region in order to minimise the error at the outer boundary, with a subsequent reduction in the resolution of the mesh for a given computational cost of the simulation.

An alternative and more convenient approach is that discussed in detail by Choinière in Ref. [123] and references therein. Summarising, one can argue that in view of the

shielding properties of the plasma, the electrostatic potential beyond the sheath decays faster than it would do in free space. In the latter case, the potential is found by solving Laplace equation obtained by setting to zero the right-hand-side of Eq. (2.19b). After imposing that the solution must vanish at $r \to \infty$, one obtains that the potential can be expressed in circular harmonics consistent with an electric field decaying as $1/r^{n+1}$, with $n = 0,\ 1,\ 2,\ \ldots$ the mode of the n^{th}-circular harmonic. Generalizing the asymptotic results of the analysis in Ref. [92], one can assume that, in presence of a plasma, the electric field decays at $\sim 1/r^{n+2}$. Following the previous reasoning, one obtains that at the outer boundary of the computational domain the potential decays as

$$\phi(\Gamma_{max}) \sim A_0 \frac{r_{max}}{r} + \sum_{n=1}^{N_{modes}} \left(\frac{r_{max}}{r}\right)^{n+1} (A_n \cos\theta + B_n \sin\theta), \tag{2.28}$$

where r_{max} measures the distance from the origin of the nodes lying on Γ_{max}, while N_{modes} is a high enough integer. Regarding coefficients A_0, A_n and B_n, these are given explicitly in Eq. (B.1). In order to exploit the double-symmetry of the problem, at the nodes lying on the two Cartesian axes in the physical space one must also impose that $\partial_x\phi|_{x=0} = \partial_y\phi|_{y=0} = 0$ or, equivalently, $\partial_\eta\phi|_{\eta=0} = \partial_\eta\phi|_{\eta=\pi/2} = 0$ and $\partial_\theta\phi|_{\theta=0} = \partial_\theta\phi|_{\theta=\pi/2} = 0$ for structured meshes defined in elliptic and cylindrical logical spaces, respectively.

The numerical algorithm developed in the framework of this thesis implements two different Poisson solvers according to the type of discretisation adopted for the computational domain: (i) a finite element-based solver for unstructured meshes, and (ii) a finite difference-based solver to be used with structured meshes. The next two sections are dedicated to the description of such solvers.

2.2.2.1 Finite Element

Upon discretising the computational domain with an unstructured mesh made up of first-order triangular elements [159], Poisson's equation is solved numerically with a *Finite Element Method* (FEM)-based Poisson solver analogous to that presented in Ref. [123]. Within each triangular element, the electrostatic potential and the space charge density are approximated by

$$\phi^{elm}(x,y) \approx \sum_{k=1}^{3} \phi_k^{elm} g_k(x,y), \tag{2.29a}$$

$$\rho^{elm}(x,y) \approx \sum_{k=1}^{3} \rho_k^{elm} g_k(x,y). \tag{2.29b}$$

In Eqs. (2.29b), the super-script *elm* identifies the element of the domain, while sub-index k represents the k^{th}-vertex of the triangle, numbered in counter-clockwise order. Using *constant strain* triangular elements, $g_k(x,y)$ is a bi-linear function of the spatial

coordinates that reads

$$g_k(x,y) = \frac{a_i + b_i \cdot x + c_i \cdot y}{2\Delta^{elm}}. \tag{2.30}$$

The constant coefficients a_i, b_i and c_i and the area Δ^{elm} depend solely on the geometrical properties of the element, and are defined as

$$\begin{gathered} a_i \equiv x_j \cdot y_k - x_k \cdot y_j, \quad b_i \equiv y_j - y_k, \quad c_i \equiv x_k - y_j, \\ \Delta^{elm} \equiv \frac{1}{2}\left| \sum_{i,j=1}^{3} (x_i \cdot y_j - x_j \cdot y_i) \right|, \\ i = 1,2,3, \quad j = mod(i,3)+1, \quad k = mod(j,3)+1, \end{gathered} \tag{2.31}$$

where the sub-indexes represent the vertices of the triangular element and $mod()$ stands for the built-in Fortran function that returns the remainder of the division between its first and second arguments. Following Eqs. (2.29b), the procedure to derive explicitly matrix $\bar{\boldsymbol{A}}$ and vector $\boldsymbol{\phi}_{BC}$ in Eq. (2.27) for the FEM-based solver is described in a high degree of detail in the work by Choinière [123], and it is not repeated here. Since their value depend only on the spatial discretisation and the boundary conditions of Poisson equation, which remain constant for a given simulation, such computation is done only once during the pre-processing phase. Therefore, solving Poisson equation reduces to the mere multiplication of a matrix by a vector and does not constitute an onerous procedure in the economy of the numerical simulation.

2.2.2.2 Finite Differences

For solving Poisson equation onto structured meshes, the software implements a *Finite Difference Method* (FDM). For curvilinear meshes, Poisson equation is solved in the logical space (χ^1, χ^2), and must thus be derived in the new set of coordinates. If elliptic and cylindrical configurations are considered, applying the change of coordinates defined in Eqs. (2.23)-(2.25) gives

$$\frac{1}{c_p^2\left(\sinh^2\xi + \sin^2\eta\right)}\left(\frac{\partial^2\phi}{\partial\xi^2} + \frac{\partial^2\phi}{\partial\eta^2}\right) = n_e + \beta n_{em} - e_i n_i \tag{2.32}$$

$$\frac{\partial^2\phi}{\partial r^2} + \frac{1}{r}\frac{\partial\phi}{\partial r} + \frac{1}{r^2}\frac{\partial^2\phi}{\partial\theta^2} = n_e + \beta n_{em} - e_i n_i. \tag{2.33}$$

The first and second spatial derivative terms in the equations above are discretized through a *centred* finite difference scheme, which provides the following approximations

$$\left.\frac{\partial\phi}{\partial r}\right|_{i,j} \approx \frac{1}{D}\left[\frac{1}{Q}\phi_{i+1,j} + \left(Q-\frac{1}{Q}\right)\phi_{i,j} - Q\phi_{i-1,j}\right], \tag{2.34a}$$

$$\left.\frac{\partial^2\phi}{\partial r^2}\right|_{i,j} \approx \frac{2}{\tilde{D}}\left[\phi_{i+1,j} - (Q+1)\phi_{i,j} + Q\phi_{i-1,j}\right], \tag{2.34b}$$

where sub-indexes (i,j) identify that the variable is being evaluated at node (χ_i^1, χ_j^2), while coefficients Q, D and $\tilde{D}$ are defined as

$$Q \equiv \frac{\Delta r_{i+1}}{\Delta r_i}, \quad D \equiv \Delta r_{i+1} + \Delta r_i, \quad \tilde{D} \equiv \Delta r_{i+1} \cdot D, \tag{2.35}$$

with $\Delta r_i \equiv r_i - r_{i-1}$ being the distance between two subsequent nodes in the direction of interest (r in the example here considered). Equations (2.34a)-(2.34b) are valid for any distribution of nodes. For the special case of uniform meshes (i.e., $\Delta r_i = \Delta r = constant$), one obtains $Q = 1$, $D = 2\Delta r$ and $\tilde{D} = 2\Delta r^2$, and the approximation of the spatial derivatives terms are

$$\left.\frac{\partial\phi}{\partial r}\right|_{i,j} \approx \frac{\phi_{i+1,j} - \phi_{i-1,j}}{2\Delta r}, \tag{2.36}$$

$$\left.\frac{\partial^2\phi}{\partial r^2}\right|_{i,j} \approx \frac{\phi_{i+1,j} - 2\phi_{i,j} + \phi_{i-1,j}}{\Delta r^2}. \tag{2.37}$$

The second derivatives $\partial^2\phi/\partial\theta^2$, $\partial^2\phi/\partial\xi^2$, and $\partial^2\phi/\partial\eta^2$ appearing in Eqs. (2.32)-(2.33) are found by using analogous formulae to the ones in Eq. (2.34b) for non-uniform meshes and Eq. (2.37) for uniform ones, respectively. The centred finite difference scheme is applied at the internal nodes of the computational domain, while at its boundaries the elements of $\bar{\boldsymbol{A}}$ are computed in agreement with the boundary conditions selected. In the χ_1-dimension, one has $\phi(1,:) = \phi_p$ and that the potential decays as shown in Eq. (2.28) at Γ_{max}.

2.2.3 Vlasov Solver $\mathscr{V}$

In the numerical algorithm here presented, the term Vlasov solver $\mathscr{V}$ identifies the set of operations that are carried out in order to compute the values of the densities of the species at the nodes of the computational domain. Being complementary to the Poisson solver $\mathscr{P}$ presented in Sec. 2.2.2, it receives from the latter the electrostatic potential profile as input, and it returns the consistent space charge vector $\boldsymbol{\rho} \equiv -(e_i\boldsymbol{n}_i - \boldsymbol{n}_e - \beta\boldsymbol{n}_{em})$. In turn, this requires the reconstruction of the discrete phase space distribution function $f_\alpha(\boldsymbol{r},\boldsymbol{v})$ of all the charged species, obtained by solving Eq. (2.19a) numerically. Taking

advantage of the collisionless character of the plasma, the code implements a *backward Liouville method*, which is a test-particle method typically used to estimate *a posteriori* the trajectories of the charged particles moving in a steady-state electromagnetic field obtained with different numerical algorithms (see Ref. [130] for an overview). Differently to its most common application, such method is applied here to compute *self-consistently* the structure of the sheath.

The procedure works as follows. Equation (2.19a) is equivalent to $df_\alpha(\boldsymbol{r},\boldsymbol{v})/d\tau = 0$. According to Liouville theorem [137], in a collisionless plasma the phase-space distribution function f_α is conserved along the characteristic equations

$$\frac{d\boldsymbol{r}}{d\tau} = \boldsymbol{v} \tag{2.38a}$$

$$\frac{d\boldsymbol{v}}{d\tau} = -\frac{e_\alpha}{2\delta_\alpha}\nabla\phi, \tag{2.38b}$$

with τ parametrising the integral curves. These equations are equivalent to the equations of motion of the charged particles moving within the sheath of the probe, and τ can be interpreted as a dimensionless time. At each node $\boldsymbol{x}_{s0} \equiv (\boldsymbol{r}_0, \boldsymbol{v}_0)$ of the four-dimensional discrete phase-space, the value of the distribution function is computed by integrating Eqs. (2.38a)-(2.38b) *backward* in time with initial conditions $\boldsymbol{x}_{s0}$. According to the configuration and the type of discretisation adopted, the present code can select among three different algorithms to carry out such integration: a *Runge-Kutta* scheme (RK), a *Leapfrog* (symplectic) scheme (LF), and an hybrid energy-conserving *Crank-Nicolson* scheme (CN) [160]. In order to avoid making the already complex and detailed presentation of the Vlasov solver too cumbersome, the descriptions of the orbital propagators and the different methods for reconstructing the electric field from the electrostatic potential at the nodes of the mesh are presented in Appendix C and Appendix D, respectively.

Regardless of the numerical algorithm used, the integration of the trajectory stops at $\tau = \tau_f$. That is, the moment at which the orbit either (i) hits the outer boundary of the domain Γ_{max}, (ii) reaches the probe contour Γ, or (iii) completes N_{tr} turns around the probe without crossing any of the boundaries of the computational domain (see Sec. C.1). Since f_α is conserved along the orbits (Liouville theorem), one has that $f_\alpha(\boldsymbol{x}_{s0}) = f_\alpha(\boldsymbol{x}_{sf})$, where $\boldsymbol{x}_{sf} \equiv (\boldsymbol{r}_f, \boldsymbol{v}_f)$ denotes the origin (root) of the characteristics. According to the BCs in Eqs. (2.21), the code sets $f_{e,i}(\boldsymbol{x}_{s0}) = f_M$ and $f_{em}(\boldsymbol{x}_{s0}) = 0$ if $\boldsymbol{r}_f$ lies on Γ_{max} [case (i)], while $f_{e,i}(\boldsymbol{x}_{s0}) = 0$ and $f_{em}(\boldsymbol{x}_{s0}) = f_{HM}$ when $\boldsymbol{r}_f$ pertains to Γ [case (ii)]. For convenience, the corresponding orbits are classified as Γ_{max}-*originated* and Γ-*originated*, respectively. In the event that $\boldsymbol{r}_f$ is within the computational domain [case (iii)], the particle is labelled as *trapped* and the algorithm assigns $f_\alpha(\boldsymbol{x}_{s0}) = 0$ regardless of its species.

This last result is a direct consequence of some of the hypotheses adopted in the model and deserves a further comment. During the formation of a sheath, particle trapping may result either as consequence of the loss of kinetic energy by particles following a collision with another particle or from the transient when the system evolves in response to some perturbation. However, the present model does not take into account collisions

and, in stationary conditions, it is not possible to identify the origin of a charge that is trapped inside the sheath during the transient phase, since the latter is absent. Under these circumstances, the typical choice is neglecting the contribution of the trapped population to the distribution functions [93, 108, 113, 123, 161]. Together with the set of hypotheses introduced at the beginning of the chapter, this poses the basis of the *Orbital Motion theory* (OMT) ordinarily employed in numerous plasma physics applications. Table 2.3 summarises the main features of the different types of orbits, which are shown in Figure 2.4.

Types of orbits

Origin (root)	Label	Distribution function
$\boldsymbol{r}_f \in \Gamma$	Γ-originated	$f_{e,i}(\boldsymbol{x}_{s0}) = 0$ $f_{em}(\boldsymbol{x}_{s0}) = f_{HM}$
$\boldsymbol{r}_f \in \Gamma_{max}$	Γ_{max}-originated	$f_{e,i}(\boldsymbol{x}_{s0}) = f_M$ $f_{em}(\boldsymbol{x}_{s0}) = 0$
$\boldsymbol{r}_f \notin \Gamma, \Gamma_{max}$ and N_{tr} turns around Γ	Trapped	$f_{e,i}(\boldsymbol{x}_{s0}) = 0$ $f_{em}(\boldsymbol{x}_{s0}) = 0$

TABLE 2.3: Classification of orbits (stationary case)

In stationary conditions, the energy is conserved along the trajectories of the charged particles [see Eqs. (2.38)]. Subsequently, a convenient choice is to apply the change of variables $(\boldsymbol{v}) \rightarrow (\varepsilon_\alpha, \zeta)$, with

$$\varepsilon_\alpha \equiv \boldsymbol{v}\cdot\boldsymbol{v} + \frac{e_\alpha}{\delta_\alpha}\left[\phi(\boldsymbol{r}) - H_\alpha \phi_p\right], \quad (H_{e,i} = 0, H_{em} = 1) \tag{2.39}$$

$$\zeta \equiv \tan^{-1}\left(\frac{\boldsymbol{v}\cdot\boldsymbol{t}}{\boldsymbol{v}\cdot\boldsymbol{n}}\right), \tag{2.40}$$

the total (dimensionless) energy and an angle in velocity space. For an elliptical (cylindrical) probe, $\boldsymbol{t}$ and $\boldsymbol{n}$ are the tangential and normal (outward) unit vectors to the ellipse (circumference) confocal (concentric) with Γ passing through $\boldsymbol{r}$. For each point of the computational domain, the code discretises the region of the phase space

$$(\varepsilon_\alpha, \zeta) \in [\varepsilon_\alpha^{min},\ \varepsilon_\alpha^{\max}] \times [0,\ 2\pi], \tag{2.41}$$

$$\varepsilon_\alpha^{min} \equiv max\left\{0,\ \frac{e_\alpha}{\delta_\alpha}\left[\phi(x,y) - H_\alpha\phi_p\right]\right\} \tag{2.42}$$

onto a grid of $N_\varepsilon \times N_\zeta$ nodes. In the energy-direction, ε_α^{min} is selected in order to comply with the condition of non-negative energy, while ε_α^{max} is a numerical parameter whose magnitude must ensure that a sufficient portion of the velocity space is taken into account. According to Eqs. (2.39)-(2.40), the nodes of the phase-space are identified as $\boldsymbol{x}_{s0} \rightarrow \boldsymbol{z}_{s0} = [\boldsymbol{r}^i, \varepsilon_\alpha^k, \zeta^l]$, with $i = 1,\ldots,N$, $k = 1,\ldots,N_\varepsilon$ and $l = 1,\ldots,N_\zeta$. Upon applying the change

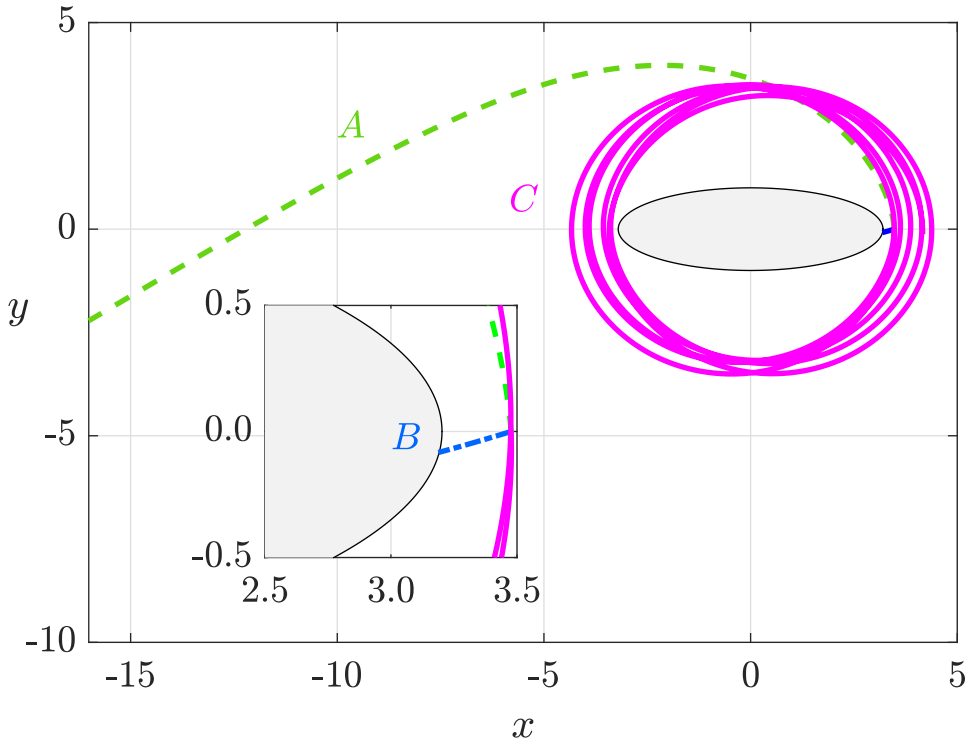

FIGURE 2.4: Example of Γ_{max}-originated (A), Γ-originated (B), and *trapped* (C) orbits [128].

of variables just discussed, the boundaries conditions of Eqs. (2.21) can be re-written as

$$f_{e,i}(\Gamma, \varepsilon_{e,i}, -\frac{\pi}{2} < \zeta < \frac{\pi}{2}) = 0, \quad f_{em}(\Gamma, \varepsilon_{em}, -\frac{\pi}{2} < \zeta < \frac{\pi}{2}) = \frac{2\exp(-\varepsilon_{em})}{\pi} \tag{2.43a}$$

$$f_{e,i}(\Gamma_{max}, \varepsilon_{e,i}, \zeta) = \frac{\exp(-\varepsilon_{e,i})}{\pi}, \quad f_{em}(\Gamma_{max}, \varepsilon_{em}, \zeta) = 0. \tag{2.43b}$$

For a probe biased at a negative potential with respect to the plasma (i.e., $\phi_p < 0$), Fig. 2.5 shows examples of the resulting diagrams in the velocity space obtained for the three species considered in the present model. The upper panels show the maps obtained by assigning different colours to regions of the velocity space yielding trapped (blue), Γ_{max}-originated (yellow) and Γ-originated particles (orange), while the bottom panels show the value of the distribution functions normalized with their maximum. For convenience, the distribution function is represented in the $\varepsilon_n - \varepsilon_t$ plane [123, 127], with

$$\varepsilon_n \equiv \varepsilon_\alpha \cdot \cos\zeta \tag{2.44a}$$

$$\varepsilon_t \equiv \varepsilon_\alpha \cdot \sin\zeta. \tag{2.44b}$$

For the attracted species (ions), panel (a) shows that there can exist two types of empty

regions in the velocity space. The first one corresponds to outgoing (i.e., $\varepsilon_n > 0$) Γ-originated orbits (*B*-type orbits in Fig. 2.4), while the two-lobed empty regions close to $(\varepsilon_n, \varepsilon_t) = (0,0)$ shown in the inset identify initial conditions yielding trapped orbits of the kind labeled with *C* in Fig. 2.4. In both cases, the algorithm assigns zero to the distribution function and the corresponding areas in panel (d) and its inset are left empty. In view of this, it is worth highlighting that the presence and extension of the trapped region are affected by the value of N_{tr}, whose importance as a numerical parameter is discussed more in detail in Sec. 3.2.1.2.

Panels (b) and (c) contain analogous information about the dynamics of the repelled species (plasma electrons) and the emitted electrons, respectively. In the former case, in addition to the orange region corresponding to trajectories whose root lies on the plasma-material interface, one observes a circular empty region centered at the origin of the $\varepsilon_n - \varepsilon_t$ diagram. The latter identifies particles whose kinetic energy is not high enough to overcome the potential barrier at that point of the computational domain.

Regarding the emitted species, one must notice that the meaning of the diagram is switched with respect to the plasma species, and the filled area in panel (e) represents the portion of the phase space populated by Γ-originated orbits. From Eqs. (2.43a)-(2.43b) and the bottom diagrams in Fig. 2.5, it is observed that the distribution function decays exponentially with the total energy ε_α. Therefore, it is convenient to distribute the N_ε nodes in the ε_α-mesh with a higher density close to ε_α^{min} in order to have a higher resolution in that region of the phase-space. With respect to the discretisation along ζ, the right panels of Fig. 2.5 shows that for the emitted species the distribution function becomes narrow as one moves away from Γ. In view of this, the algorithm implements a higher resolution in the area around $\zeta = 0$, since during the development of the code it was observed that a uniform distribution could prevent from recovering quasi-neutrality at Γ_{max}.

Once the structure of the plasma sheath is obtained, the macroscopic quantities of interest can be derived from the moments of the distribution functions f_α [127]. After adopting the change of variables introduced in Eqs. (2.39)-(2.40), the densities at the nodes of the computational domain are obtained from

$$n_\alpha(\boldsymbol{r}) \approx \frac{1}{2}\int_{\varepsilon_\alpha^{min}}^{\varepsilon_\alpha^{max}} \int_0^{2\pi} f_\alpha(\boldsymbol{r}, \varepsilon_\alpha, \zeta) d\varepsilon_\alpha d\zeta, \tag{2.45}$$

with $1/2$ the Jacobian of the $(\boldsymbol{v}) \rightarrow (\varepsilon_\alpha, \zeta)$ transformation. The double integral of Eq. (2.45) is computed numerically using the trapezoidal rule

$$n_\alpha(\boldsymbol{r}_i) \approx \frac{1}{2}\sum_{l=2}^{N_\zeta} \frac{S_\alpha^{int}(\boldsymbol{r}_i, \zeta_l) + S_\alpha^{int}(\boldsymbol{r}_i, \zeta_{l-1})}{2}(\zeta_l - \zeta_{l-1}), \tag{2.46a}$$

$$S_\alpha^{int}(\boldsymbol{r}_i, \zeta_l) \approx \sum_{k=2}^{N_\varepsilon} \frac{f_\alpha(\boldsymbol{r}_i, \varepsilon_{\alpha,k}, \zeta_l) + f_\alpha(\boldsymbol{r}_i, \varepsilon_{\alpha,k-1}, \zeta_l)}{2}(\varepsilon_{\alpha,k} - \varepsilon_{\alpha,k-1}), \tag{2.46b}$$

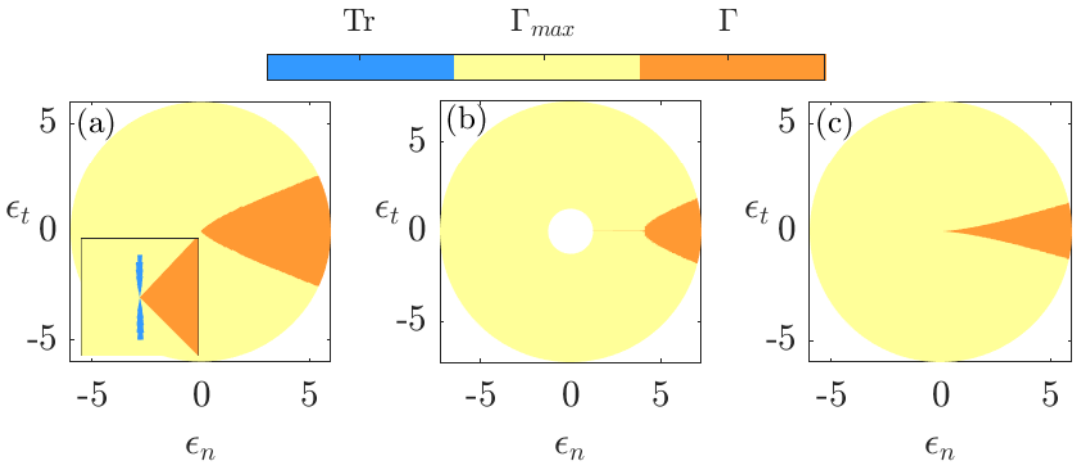

(a) Map of the $\varepsilon_n - \varepsilon_t$ highlighting area in the velocity space corresponding to trapped (blue), Γ_{max}-originated (yellow) and Γ-originated (orange) orbits for plasma ions [panel (a)], plasma electrons [panel (b)] and emitted electrons [panel (c)]. Inset in panel (a) show a detail of the region around $(\varepsilon_n, \varepsilon_t) = (0,0)$.

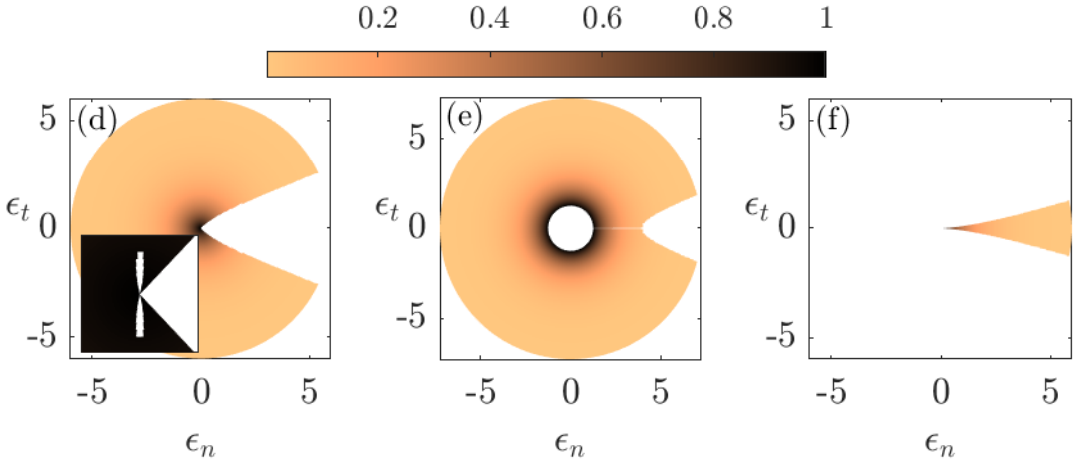

(b) Diagrams of f_α (normalized to its maximum) in the $\varepsilon_n - \varepsilon_t$ for plasma ions [panel (d)], plasma electrons [panel (e)] and emitted electrons [panel (f)]. Inset in panel (d) show a detail of the region around $(\varepsilon_n, \varepsilon_t) = (0,0)$.

FIGURE 2.5: Example of distribution function diagrams in the $\varepsilon_n - \varepsilon_t$ plane for plasma ions [panels (a) and (d)], plasma electrons [panels (b) and (e)], and emitted electrons [panels (c) and (f)] in the sheath around a negatively biased probe ($\phi_p < 0$).

and the space charge vector is eventually obtained from $\boldsymbol{\rho} = e_i \boldsymbol{n}_i - \boldsymbol{n}_e - \beta \boldsymbol{n}_{em}$. In addition to the densities of the particles, an interesting figure of merit for analyses related with LWTs applications is the current per unit length collected (emitted) at the interface Γ, which reads

$$I_\alpha = e n_0 \sqrt{\frac{k_B T_e}{2\pi m_e}} \times p_\Gamma \times j_\alpha. \tag{2.47}$$

In the equation above, the first term represents the random thermal motion of the plasma electrons, p_Γ is the perimeter of the probe and j_α the dimensionless function

$$j_\alpha \equiv e_\alpha \sqrt{\frac{\delta_\alpha}{\mu_\alpha}} \frac{\sqrt{\pi}}{p_\Gamma} \int_0^{p_\Gamma} j_s(s) ds \tag{2.48}$$

with

$$j_s(s) \equiv \int_{-\infty}^{+\infty} (\boldsymbol{v} \cdot \boldsymbol{u}_n) f_\alpha(\Gamma, \boldsymbol{v}) d\boldsymbol{v}, \tag{2.49}$$

the local normalized current per unit area. In Eq. (2.49), the coordinate s measures the arc-length along Γ defined in Eq. (A.2) in Appendix A. During the post-processing, analogous formulae to those of Eq. (2.46a)-(2.46b) are used to compute the discrete values of the current at Γ. It is interesting to notice that, in the stationary scenario depicted above, the dynamics of the different species can be treated separately as μ_α does not enter in the governing equations of the system. Therefore, the solutions found with the present algorithm are valid for different types of positive ions, whose mass should be specified only when the value of the current is needed.

2.2.4 Iterative Procedure

Similarly to other Eulerian Vlasov solvers previously presented in the literature [123], the solvers of Secs. 2.2.2-2.2.3 are embedded into an iterative procedure that seeks for the values of the charge density vector $\boldsymbol{\rho} \in \mathscr{R}^N$ at the N nodes of the computational domain satisfying the set of nonlinear algebraic equations

$$\boldsymbol{G}(\boldsymbol{\rho}) \equiv \boldsymbol{\rho} - \mathscr{V}[\mathscr{P}(\boldsymbol{\rho})] = 0. \tag{2.50}$$

In the present work, an acceptable numerical approximation for the solution to Eq. (2.50) is one that complies with

$$\|\boldsymbol{G}(\boldsymbol{\rho})\|_2 \equiv \sqrt{G_1^2 + G_2^2 + \ldots + G_n^2} < tol, \tag{2.51}$$

with tol a small enough scalar selected by the user. The iterative process works as follow. Starting from an initial guess $\boldsymbol{\rho}_0$, usually taken from the numerical solution of a similar

configuration, the code first updates its value following the *fixed point*-like strategy

$$\boldsymbol{\rho}_{n+1} = \boldsymbol{\rho}_n + \boldsymbol{w} \cdot \boldsymbol{G}(\boldsymbol{\rho}_n), \quad n = 0, 1, ... \tag{2.52}$$

where $\boldsymbol{w}$ identifies a vector of weights whose components decrease with the distance from the plasma-body interface, since the probe-induced perturbation is expected to be low as one approaches the outer plasma boundary, where quasi-neutrality is retrieved. The value of the charge density vector is updated according to Eq. (2.52) as long as the Euclidean norm $\|\boldsymbol{G}\|_2$ decreases. Unless the solution already complies with the required tolerance, when the code detects that no further improvement is achieved the updating strategy is switched to a Newton-Raphson map [153]

$$\boldsymbol{\rho}_{n+1} = \boldsymbol{\rho}_n - \boldsymbol{J}^{-1}|_{\boldsymbol{\rho}_n} \boldsymbol{G}(\boldsymbol{\rho}_n), \quad n = 0, 1, ... \tag{2.53}$$

with $\boldsymbol{J}|_{\boldsymbol{\rho}_n}$ the Jacobian matrix of $\boldsymbol{G}$ evaluated at $\boldsymbol{\rho}_n$ with a central finite difference scheme. Although typically not sufficient to reach the selected accuracy, the *fixed-point*-like iteration method of Eq. (2.52) is useful in order to get close enough to the final solution and to reduce significantly the number of estimations of $\boldsymbol{J}|_{\boldsymbol{\rho}_n}$, whose evaluation is by far the most expensive task from a computational standpoint. For this reason, the algorithm performs a new estimation of the Jacobian matrix only when the correction obtained with the previous one no longer improves the result. Although this choice may slow down the speed of convergence, the efficiency of the algorithm is enhanced overall. Since the Jacobian matrix is, in general, ill-conditioned, the code provides the possibility of implementing a Tikhonov regularization procedure analogous to that described in Ref. [123]. Its main steps are summarised in Appendix E.

Table 2.4 summarizes the characteristics of the different Vlasov-Poisson solvers that were implemented in the analysis presented in this work. They are named after the different combinations of meshes, Poisson solvers and numerical integrators.

Name	Mesh	Poisson solver	Integrator
FEM-RK	Unstructured	FEM [123]	Runge-Kutta [153]
FDM-RK	Structured	FDM	Runge-Kutta [153]
FEM-LF	Unstructured	FEM [123]	Leapfrog [153]
FDM-LF	Structured	FDM	Leapfrog [153]
FDM-CN	Structured	FDM	Crank-Nicolson [160]

TABLE 2.4: Summary of the different numerical algorithms implemented in the present analysis [128].

Chapter 3

Results of the stationary Vlasov-Poisson solver

This chapter presents the main results obtained with FONKS-G (i.e., the stationary Eulerian Vlasov-Poisson solver introduced in Chapter 2). After an extensive comparison with previous numerical results for verification purposes, novel results concerning the properties of the various numerical algorithms are presented and used to draw some generic conclusions about numerical and physical limitations affecting to stationary Vlasov-Poisson solvers. Eventually, a comprehensive parametric investigation of various configurations involving electron-emitting elliptical objects is presented in the last section of the chapter. Its outcomes allow to identify the main features of plasma sheaths that develops in presence of elliptical missive probes. The main core of the results presented in the following sections were published into two recent works [128, 129].

3.1 Verification of the numerical algorithm

In order to verify the correct implementation of the various solvers of Table 2.4, the results of FONKS-G were compared with previous analytical and numerical results obtained with more mature numerical tools for the investigation of plasma sheaths.

3.1.1 Versus FONKS-C

A first benchmark was carried out against a code for cylindrical emissive probes presented originally in Ref. [113] and recently upgraded (see Ref. [162]). Registered with the name *Free-of-Noise Kinetic Solver for Cylindrical geometries* (FONKS-C), the code is based on a kinetic model analogous to that presented in Chapter 2. However, it is restricted to the investigation of cylindrical probes, for which radial symmetry holds. Taking advantage of such feature, and of the subsequent conservation of the angular momentum along the collisionless orbits of the charged particles, the algorithm defines an effective potential

that allows to express the densities of each species as a functional of the electrostatic potential without the need for explicit numerical integration of the particles trajectories. Accordingly, the Vlasov-Poisson system of equations becomes a single integro-differential equation that is solved with a Newton method map similar to that of Eq. (2.53).

To compare the results of FONKS-G with those of FONKS-C, the following approach was adopted. First, FONKS-C computes self-consistenly the structure of the plasma sheath for a configuration with $e_p = 0$, and a certain set of dimensionless parameters [see Eq.(2.20)]. The radial space charge density profile thus obtained is then interpolated linearly at the nodes of the two-dimensional domain defined in FONKS-G, and serves as input for the novel Poisson solver $\mathscr{P}$. The resulting electrostatic potential is then passed to the novel Vlasov solver, which provides the consistent space charge density vector. At this point, the sheath structures obtained with the two codes are compared among each other, along with the fluxes of the species at the plasma-material interface Γ. In the following, a selection of the results from this benchmark is presented in order to provide evidence for the reliability of the novel results presented in the rest of the chapter.

Figure 3.1 contrasts the solution obtained with FONKS-C (round markers) against the one computed with FONKS-G (cross markers) for the following set of dimensionless parameters

$$e_p = 0,\ b_p = 1,\ \phi_p = -4,\ \delta_i = 1,\ \delta_{em} = 0.32,\ \beta = 1.72. \tag{3.1}$$

Being the first one to be developed among the different solvers of the list in Table 2.4, the results for this first phase of the verification procedure were computed with the FEM-RK solver, using the piecewise-constant electric field reconstruction (see Appendix D.2) and the numerical parameters

$$N = 539,\ r_{max} = 7.5,\ N_\varepsilon = 150,\ N_\zeta = 360,\ N_{tr} = 100, \varepsilon_\alpha^{max} = \varepsilon_\alpha^{min} + 6. \tag{3.2}$$

The top-left panel shows the electrostatic potential profiles normalised with the probe bias. Following Ref. [94], the results are plotted against b_p^2/r^2. This is a convenient choice since, for $e_p = 0$ (i.e., cylindrical probes), the value of the current collected is the one predicted by the OML theory if the profile does not cross the diagonal. The same representation will be adopted in the remaining part of the dissertation, unless specified otherwise. Substantial overlapping of the two curves indicates that the Poisson solver is well implemented. Despite a slight, but acceptable, discrepancy is present at the external boundary Γ_{max}, the charge density profiles in the top-right panel are in good agreement as well.

In order to make sure that this is not given by a compensation of different errors committed during the computation of the charge density of the different species, one provides in the bottom panel such profiles separately. All three pairs of curves overlap and follow the expected behaviour. The (normalised) densities of the plasma species approach to one as the distance from the plasma-material interface increases, though the computational domain was cut before since quasi-neutrality is already satisfied as one observes from the top-right panel. At Γ (i.e., $r = b_p = 1$), the density of the repelled species is reasonably very low ($n_e \approx 0$), since the probe bias represents a potential energy barrier

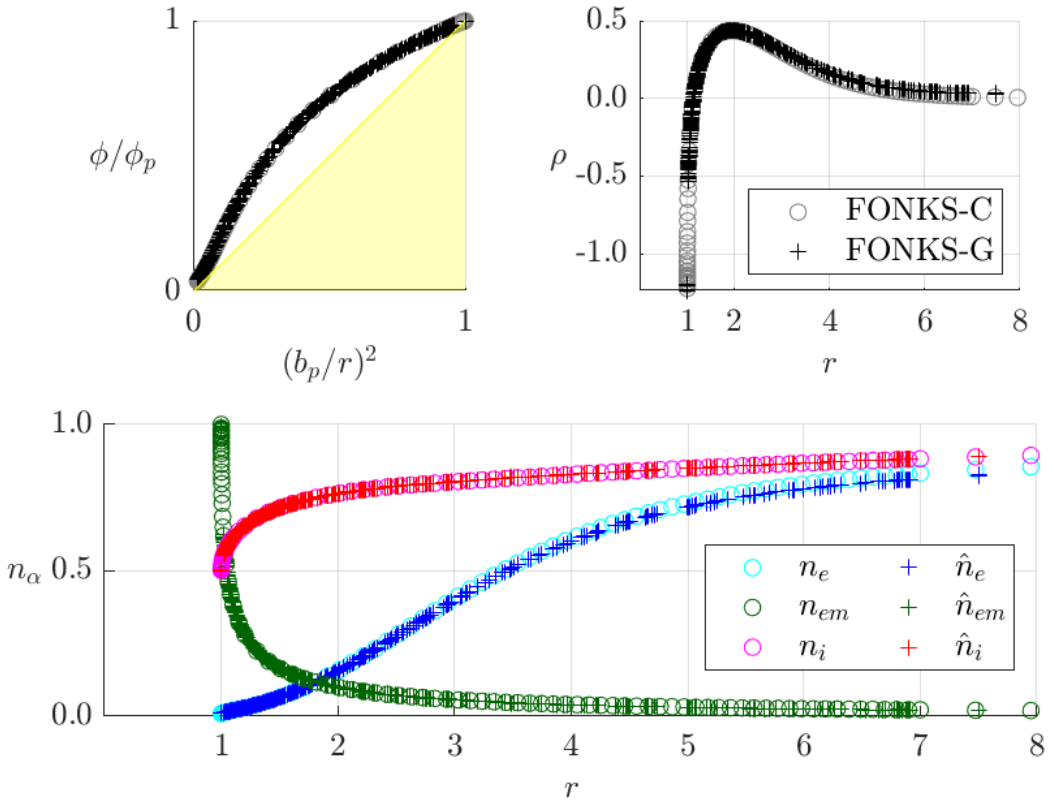

FIGURE 3.1: Verification of the code for the set of parameters in Eq. (3.2). Top panels: electrostatic potential profile (left) and charge density (right). Bottom panel: density of plasma ions (magenta, red), plasma electrons (cyan, blue) and emitted electrons (light and dark green). Crosses and circle show the results obtained with FONKS-G and FONKS-C, respectively.

and only the most energetic particles can arrive there. For the attracted species, the charge density gives $n_i \approx 0.5$, which is the expected value when OML condition holds for a two-dimensional problem (see Ref. [108]). This is consistent with the electrostatic potential profile not crossing the diagonal in the top-left panel. Regarding the emitted electrons, their density is unitary at the emitting surface, which implies that all electrons emitted at Γ are driven away by the electric field. This is expected as the electrostatic potential profile shown in the top-left panel is monotonic. As r increases, the density of the emitted species decreases with a steep trend and approaches zero asymptotically.

Overall, the profiles shown in Fig. 3.1 prove that the numerical algorithm is well-implemented and that the results obtained with FONKS-G are consistent with those of FONKS-C. The little discrepancy in the charge density profiles at the plasma boundary is due to the fact that the grid used to dicretise the velocity space (i.e., the $\varepsilon_\alpha - \zeta$ domain) is coarser in the case of FONKS-G, which has to comply with much more stringent constraints from the point of view of the computational cost due to the necessity of explicit integration of particle trajectories.

Taking as baseline the set of parameters of Eq. (3.2), further proof of the well implementation of the algorithm was obtained through parametric analyses modifying one at a time some of the governing parameters. Figure 3.2 shows the results corresponding to different values of the probe bias ϕ_p, which spans over two orders of magnitude. As in the reference case discussed previously, the FEM-RK solver in combination with the piecewise-constant electric field reconstruction was used, using the numerical parameters

$$N \sim 10^{2-3},\ r_{max} \sim 10^{1},\ N_\varepsilon = 150,\ N_\zeta = 360,\ N_{tr} \sim 10^{0-1}, \varepsilon_\alpha^{max} = \varepsilon_\alpha^{min} + 6. \qquad (3.3)$$

In the top panels, the electrostatic potential profiles obtained with the two codes are shown

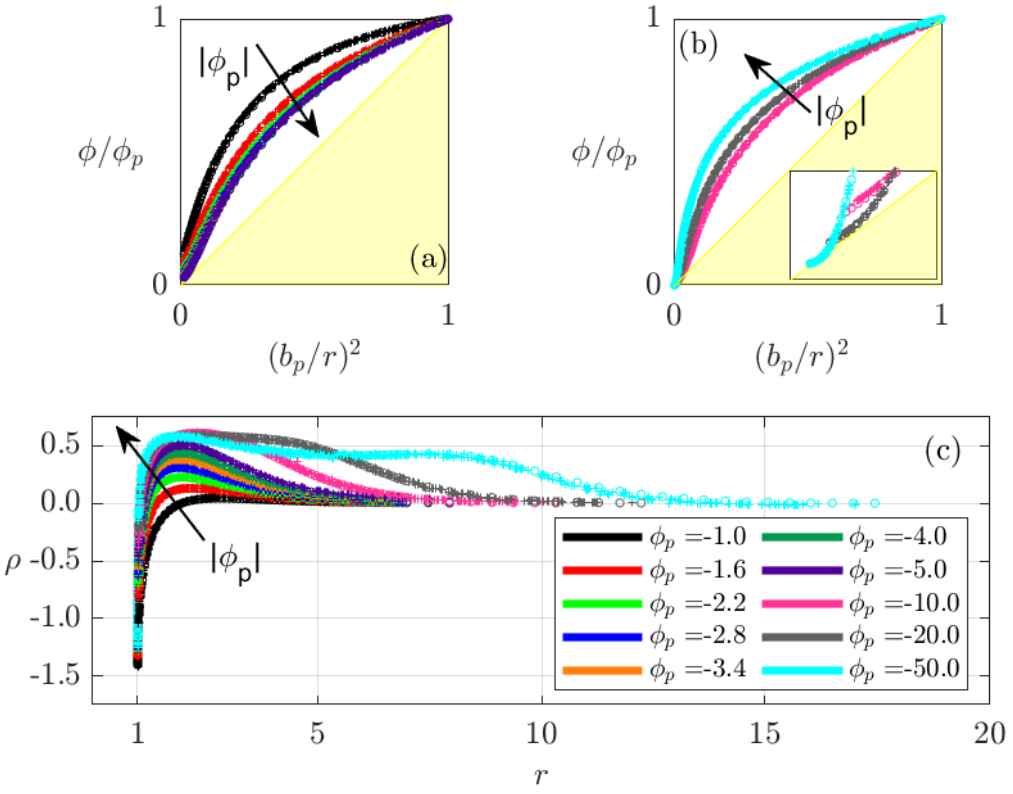

FIGURE 3.2: Verification of the code for the set of parameters given in Eq. (3.2) and several values of ϕ_p identified by different colours (see legend). Electrostatic potential profiles for $-5 \leq \phi_p \leq -1$ [panel (a)] and $-50 \leq \phi_p \leq -10$ [panel (b)]. Total charge density vectors [panel (c)]. Results obtained with FONKS-C and FONKS-G are identified with round markers and crosses, respectively.

for the intervals $-5 \leq \phi_p \leq -1$ [panel (a)] and $-50 \leq \phi_p \leq -10$ [panel (b)]. Similarly to the previous case, round markers (FONKS-C results) and crosses (FONKS-G results) practically overlap, meaning that the two codes provide analogous results. The inset of panel (b) highlights the electrostatic potential faraway from the plasma-body interface. For the highest value of ϕ_p considered, one observes that the curves cross the diagonal, meaning that positive ions collection falls beyond the OML regime in this case. This is

consistent with other results obtained for similar plasma parameters (see for instance Fig.6 in Ref. [162]).

Panel (c) shows the comparison for the space charge density. Intuitively, the size of the sheath, and therefore the computational domain, increases with ϕ_p. Due to limitations with the computational resources, the resolution was decreased for such bigger computational box. Despite some discrepancies are detected, the profiles of the two codes still agree to a more than acceptable extent. In addition, one of the main purposes of the present analysis is that of investigating the emission in SCL conditions, which occur for negatively-biased objects with small $|\phi_p|$, for which the agreement between the two codes is total because a good resolution can be used for FONKS-G.

Figure 3.3 shows a third comparison addressing the variation of the size of the object-to-Debye length ratio b_p. Only the charge density profiles are shown and plotted against

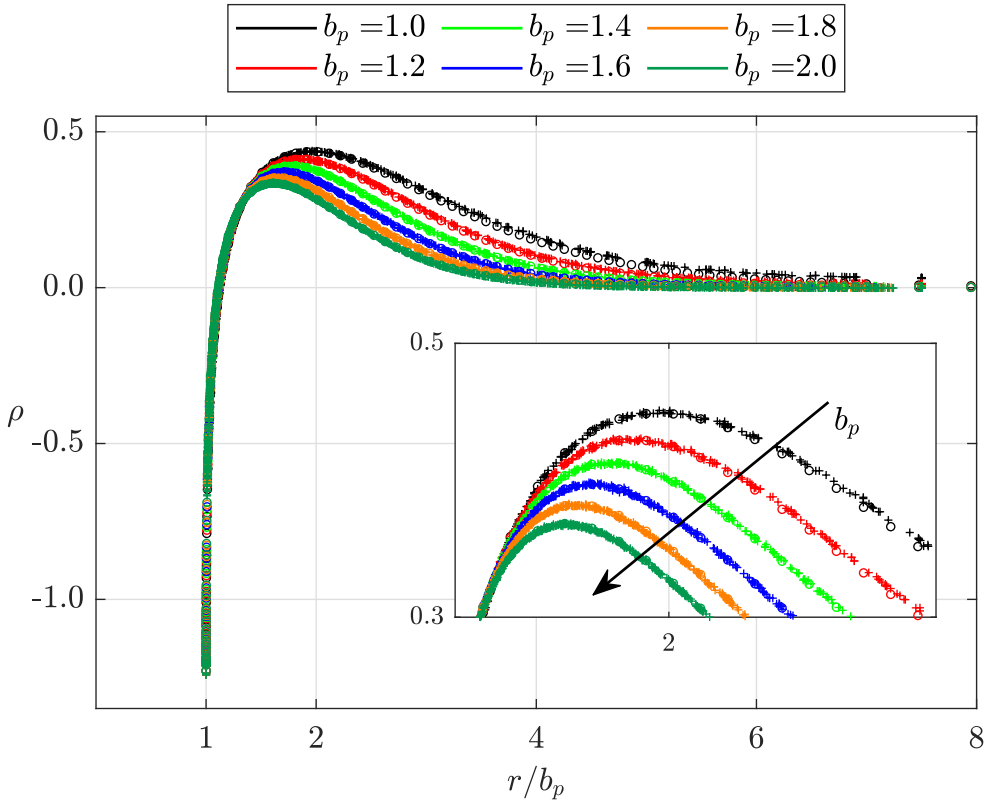

FIGURE 3.3: Charge density vector for $1 \leq b_p \leq 2$ (see legend for colour scheme) and the rest of the parameters given in Eq. (3.2). Results obtained with FONKS-C and FONKS-G are identified with round markers and crosses, respectively.

the normalised radial coordinate r/b_p. The results from the two codes match well, as highlighted in the detailed view of the sheath region where the charge density peaks (see inset). Overall, one observes that the size of the sheath relative to the characteristic length of Γ diminishes for increasing r_p, though in absolute terms the contrary holds. Concerning

the operational regime, the value of the density at the plasma-material interface suggests that the current collection and emission occur in the OML and non-SCL regimes, respectively. The former result is consistent with previous analytical works stating that OML current collection holds for cylinders with characteristic dimensions of the order of the Debye length [94, 162].

In addition to the structure of the sheath, it is interesting to compare the values of the currents collected or emitted at the plasma-body interface, which is one of the most significant figures of merit in LWT applications. Figures 3.4 shows the relative difference $100 \times |(j_\alpha^C - j_\alpha^G)/j_\alpha^C|$ between the fluxes of the α-species obtained from the novel code (super-index G) and that of Ref. [113] (super-index C). Recalling that the basic set of

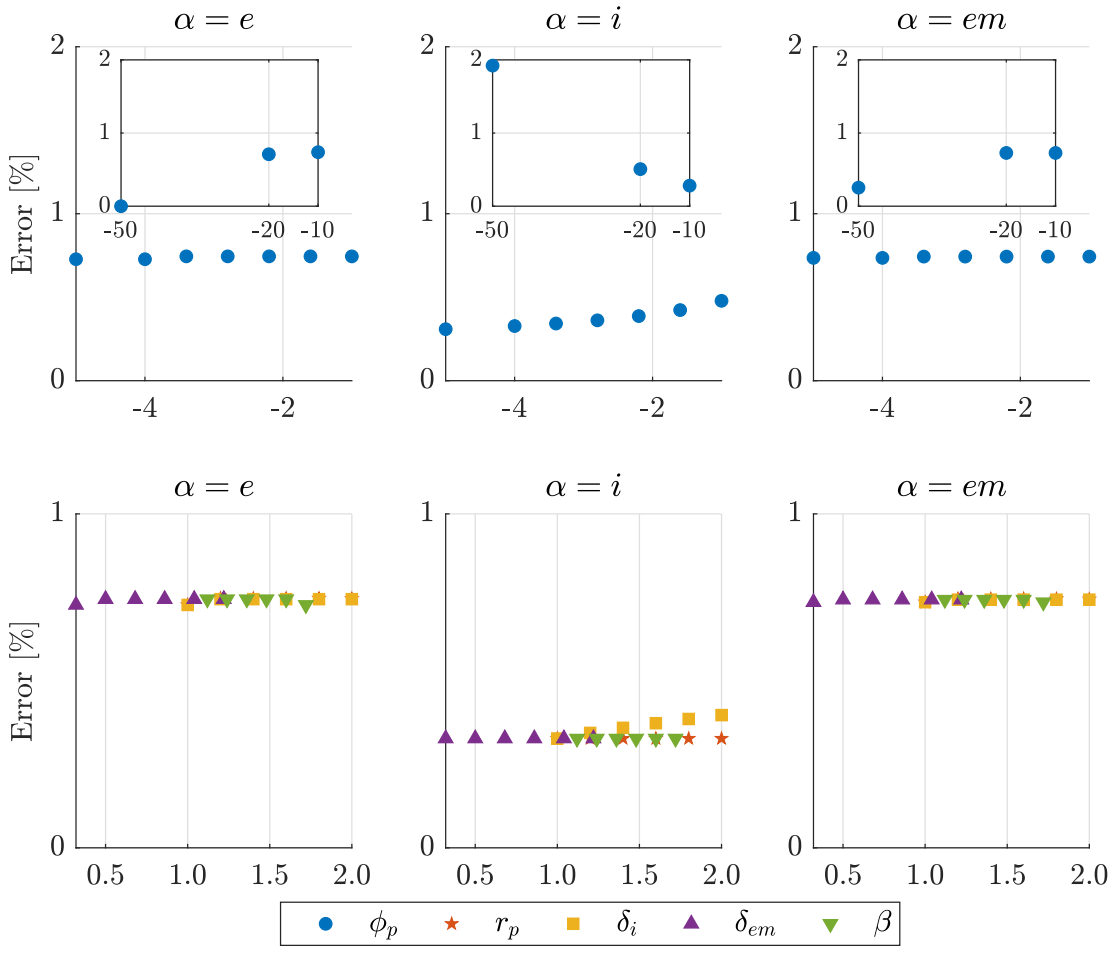

FIGURE 3.4: Relative error $100 \times |(j_\alpha^C - j_\alpha^G)/j_\alpha^C|$ for plasma electrons (left panels), ions (middle panels) and (right panels) for different values of ϕ_p (top panels) and r_p, δ_i, δ_p, β (bottom panels). Different combinations of markers and colours identify the parameter being changed with respect to the list given in Eq. (3.2).

parameters is that of Eq. (3.2), different combinations of markers and colours identify which of the parameter is being changed. For the sake of clarity, the results corresponding

to the variation of ϕ_p are gathered in the top panels, while the remaining cases are shown in the bottom panels. Left, middle and right panels correspond to plasma electrons, plasma ions and emitted electrons, respectively. For almost all the cases considered the error is below 1%, with only the configuration with $\phi_p = -50$ showing an error of around 2%, arguably because of the lower resolution achieved in view of the larger computational domain. Overall, the agreement between FONKS-G and FONKS-C is very good and one can conclude that the novel code is well-implemented.

3.1.2 Versus CPIC

A second verification campaign provides further evidence of the reliability of FONKS-G by checking its results with those obtained with *CPIC*: a well-tested PIC code for curvilinear geometries introduced in Ref. [163], which the author had the opportunity to exploit as a user during a collaboration with Dr. Delzanno and his group at Los Alamos National Laboratory (LANL). Contrary to FONKS-C, CPIC can address plasma-material interfaces of any (three-dimensional) curvilinear geometry. In order to reproduce the elliptical configurations that were the main focus of this second benchmark investigation, several quasi-2D simulations were run with CPIC imposing reflective boundary conditions at the top and bottom faces located at $z = \pm\lambda_{De}/2$, respectively.

Figure 3.5 shows the results of a first simulation, corresponding to the dimensionless parameters

$$e_p = 0.95,\ b_p = 1,\ \phi_p = -4,\ \delta_i = 1,\ \delta_{em} = 0.0,\ \beta = 0.0. \tag{3.4}$$

Since axial symmetry no longer holds, the macroscopic profiles at the horizontal ($y = 0$) and vertical ($x = 0$) axes of the computational domain are plotted separately in Fig. 3.5(a) and Fig. 3.5(b), respectively. In addition to the comparison with CPIC, whose results are identified by light grey $\times$-markers, a cross-verification between the *FEM-RK* (dark grey circles) and *FDM-CN* (black crosses) solvers is presented (see Table 2.4 for details about the different solvers implemented in FONKS-G). Despite using slightly different computational domains, results are in good agreement, though CPIC profiles, which are averaged over 5000 time steps in order to filter out the statistical noise, show some features that are absent in the case of FONKS-G.

A first remarkable difference is the behaviour of the electrostatic potential (top-left panel) at the external boundary of the computational domain. This is due to the different boundary condition selected for the Poisson equation. In fact, while for FONKS-G simulations it was imposed that the potential decays as in Eq. (2.28), CPIC assumes that $\phi(\Gamma_{max}) = 0$. As a consequence, the electrostatic potential obtained with CPIC changes curvature towards the external boundary of the computational domain, where it reconnects to zero. Due to the presence of potential barriers, such feature has an impact on the density of the electrons (bottom-right panel), which follows the same trend as the potential profile. That is, n_e itself presents an inflection point towards the outer plasma boundary, where it assumes a unitary value. In turn, CPIC charge density profiles (top-right panels)

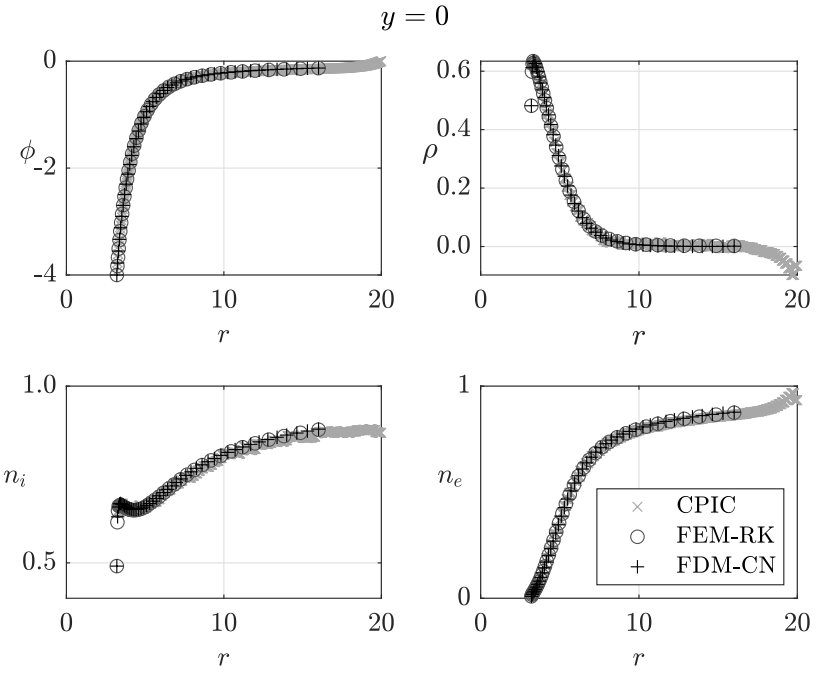

(a) Plasma sheath at $y = 0$ for the physical parameters of Eq. (3.4)

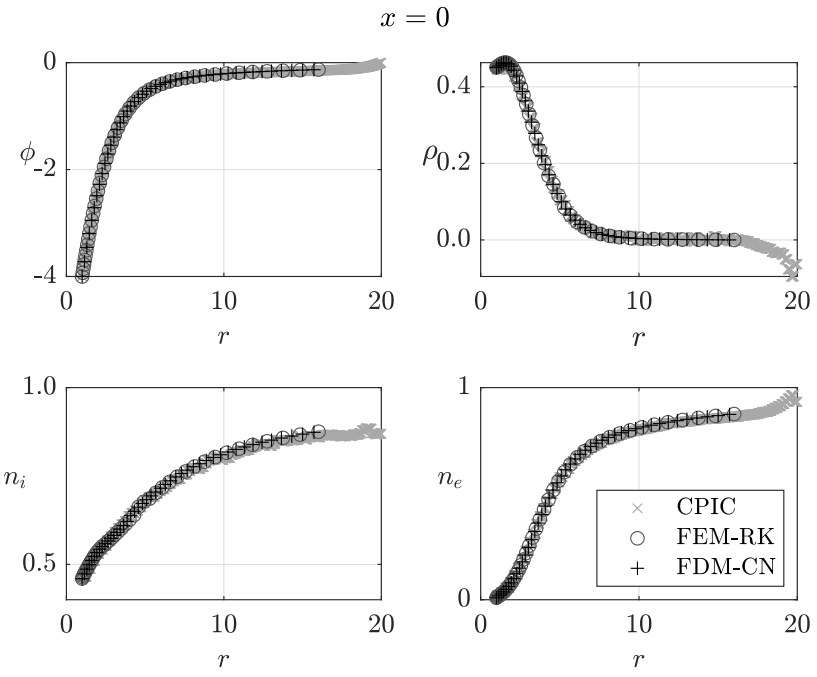

(b) Plasma sheath at $x = 0$ for the physical parameters of Eq. (3.4)

FIGURE 3.5: Comparison of FONKS-G and CPIC results (light grey $\times$-markers) for the set of physical parameters in Eq. (3.4). FEM-RK and FDM-CN solvers of FONKS-G are identified with dark grey circles and balck crosses, respectively.

show a residual sheath in such region since, contrary to that of the electrons, the density of the positive ions (bottom-left panel) does not reach a unitary value. As discussed, such residual sheath is a numerical artifact stemming from the boundary condition selected, and it does not affect significantly the overall structure of the plasma sheath, nor the values of the fluxes at the plasma-material interface.

Regarding the latter, the values of the currents of electrons and ions at the plasma-material interface are gathered in Table 3.1. For the configuration at hand, hydrogen nuclei giving $\mu_i = 1836$ were considered, though for the computation of the structure of the plasma sheath this is relevant only for CPIC as the dynamics of the particles can be decoupled in the stationary model at the basis of FONKS-G. As expected, the current of ions, which are the attracted species, is higher than that of the repelled electrons, even though they are in the same order of magnitude due to the bigger mass of the positively charged particles. The three solvers provide very similar outputs, with differences in the order of 1% and 2%.

Solver	$I_e\,[A/m]$	$I_i\,[A/m]$
CPIC	2.46×10^{-6}	7.53×10^{-6}
FEM-RK	2.42×10^{-6}	7.67×10^{-6}
FDM-CN	2.43×10^{-6}	7.70×10^{-6}

TABLE 3.1: Magnitude of the currents per unit length of plasma electrons (I_e) and plasma ions (I_i) at the plasma-material interface, obtained with CPIC and the FEM-RK and FDM-CN solvers of FONKS-G.

A second appreciable distinction is the discrepancy in the value of the density of the attracted ions at the plasma-material interface at the x-axis [bottom left panel in Fig. 3.5(a)]. There, both FONKS-G solvers give $n_i \approx 0.5$, which is in agreement with the results predicted by the OML theory for a two-dimensional probe with small enough radus (see Ref. [108]). On the contrary, CPIC provides a value which is slightly higher, though it is not evident in the plot as the corresponding marker lies behind the very dense set of points located where the curve shows a bump. Rather than a significant disagreement between the codes, this discrepancy is due to the fact that CPIC does not provide the value of the density exactly at the plasma-material interface, but an average computed along the cell next to it. Since the density increases steeply at the horizontal axis (see FONKS-G curves), a small displacement in the radial direction might result in a significant difference in the value detected. This is not the case at the vertical axis, where the density of ions increases more smoothly with the radial distance.

Such difference in the rate of change of the densities of the plasma species at the y- and x- axes is due to the fact that at the latter the electric field is bigger as it emerges by looking at the slopes of the electrostatic potential profiles (top-left panels). In fact, the intensity of the electric field is correlated with the curvature of the biased object, which is maximum at the semi-major axis lying on the x-axis of the computational domain in the case at hand. Being the electric field smaller at the semi-minor axis, one observes that the density of the ions falls below the OML value there. This outcome aligns with the

analysis of Laframboise and Parker [108], who demonstrated that, in the Laplacian limit, OML theory holds for oblate spheroids up to an aspect ratio of 2.537 (i.e., $e_p \approx 0.92$). A more detailed analysis of why the OML conditions do not hold when the slenderness of the object becomes too high is provided later in the chapter when the results of a parametric analysis of different elliptical probes are discussed in Sec. 3.3.2.

Additional results of comparisons between CPIC and FONKS-G are shown in Fig. 3.6, which correspond to the non-dimensional parameters

$$e_p = 0.75,\ b_p = 1,\ \phi_p = -4,\ \delta_i = 1,\ \delta_{em} = 0.32, \tag{3.5}$$

and different value of emission level β as indicated in the captions of the sub-figures. As before, values are plotted at the x-axis (right sub-figures) and y-axis (left sub-figures) separately, while the results of FONKS-G (crosses) were obtained with the FDM-CN solver alone in this specific case. Generally speaking, the two codes are in good agreement, though the density profiles of the plasma species (bottom panels) differ slightly more than in the case of the Langmuir elliptical probe discussed above. In particular, while remaining very close, curves obtained with FONKS-G are somewhat higher than those of CPIC. This little difference might be explained by the fact that the profiles obtained with CPIC seem to be more affected by numerical noise than those of Fig. 3.5, though the same averaging was applied while post-processing the output data.

Again, the most prominent difference is detected at the plasma material interface, where the values of n_i and n_{em} do not appear to be in agreement. As discussed previously, this is due to the fact that the outputs of CPIC do not coincide precisely with the values at the plasma-material interface. Since the slopes of the curves are very steep, especially in the case of emitted electrons, whose density decays quickly with the radial distance, the plots show a relatively big difference, which is not reflected in the values of the current at the plasma-material interface. As reported in Table 3.2, the two solvers return values of the currents that are in good agreement for all the three species of plasma considered. In fact, the relative error is $\approx 4\%$ in the worst case scenario, which is represented by plasma ions for the configurations at hand. In absolute terms, the discrepancies are highest for the current of emitted electrons, whose value is bigger than that of the plasma species by two orders of magnitude. This is consistent with the fact that the density of the emitted electrons at the probe interface is several times that of the background plasma.

An interesting aspect is that the current does not scale linearly with the emission level β. This is a well-known phenomenon due to the high density of electrons accumulating in the region of space close to the emitting surface that results in the appearance of a potential well next to the plasma-material interface when the emission level increases above a certain threshold. The subsequent reversal of the electric field causes the least energetic electrons to be reflected back to the emitting-surface, thus giving rise to the so-called Space Charge Limited (SCL) emission. As anticipated in the introduction (see Chapter 1), this is detrimental for LWTs applications as it poses a limit to the amount of current that the device is able to emit (and therefore to generate).

Intuitively, for a fixed value of probe bias, the potential well appears and increases

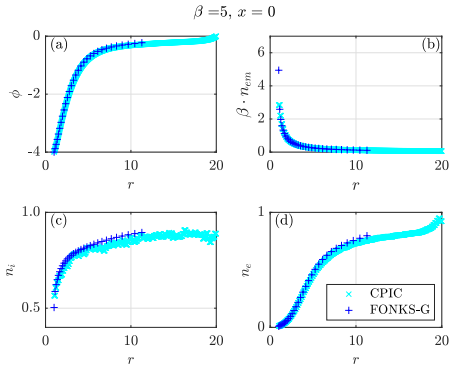

(a) Plasma sheath at $x = 0$ for $\beta = 5$

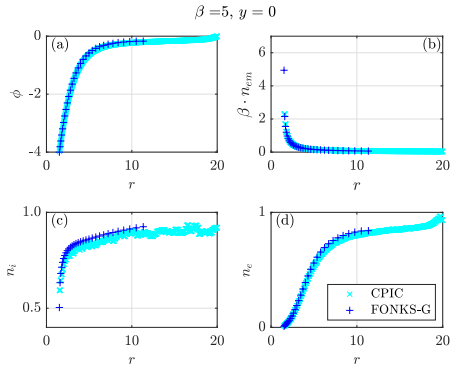

(b) Plasma sheath at $y = 0$ for $\beta = 5$

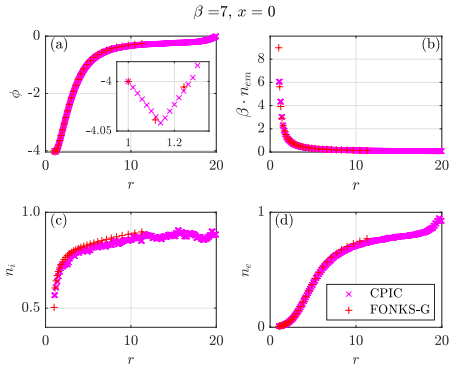

(c) Plasma sheath at $x = 0$ for $\beta = 7$

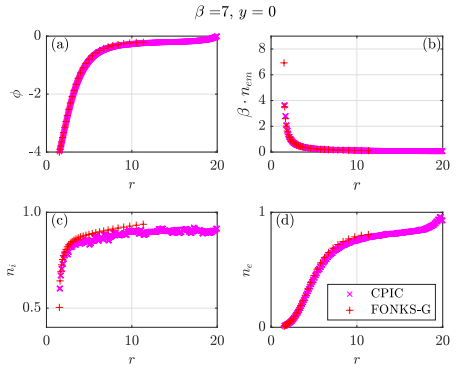

(d) Plasma sheath at $y = 0$ for $\beta = 7$

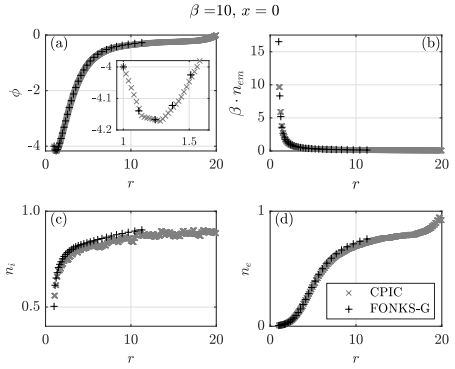

(e) Plasma sheath at $x = 0$ for $\beta = 10$

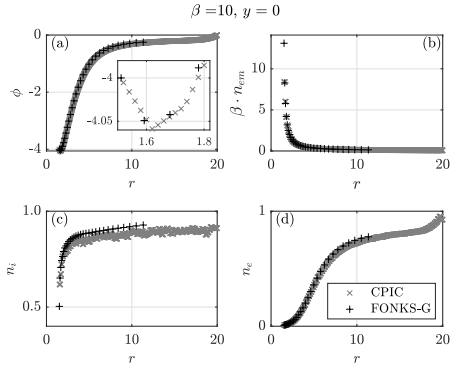

(f) Plasma sheath at $y = 0$ for $\beta = 10$

FIGURE 3.6: Plasma sheath corresponding to the physical parameters of Eq. (3.5) and different values of emission level β, computed with CPIC ($\times$ markers) and FONKS-G ($+$ markers). Sub-figures on the left (right) shows macroscopic quantities at nodes lying on the y-axis (x-axis).

β	Solver	$I_e\,[A/m]$	$I_i\,[A/m]$	$I_{em}\,[A/m]$
5	CPIC	1.39×10^{-6}	4.23×10^{-6}	4.21×10^{-4}
	FDM-CN	1.37×10^{-6}	4.40×10^{-6}	4.23×10^{-4}
7	CPIC	1.38×10^{-6}	4.22×10^{-6}	5.75×10^{-4}
	FDM-CN	1.36×10^{-6}	4.40×10^{-6}	5.79×10^{-4}
10	CPIC	1.30×10^{-6}	4.23×10^{-6}	6.43×10^{-4}
	FDM-CN	1.27×10^{-6}	4.40×10^{-6}	6.33×10^{-4}

TABLE 3.2: Magnitude of the currents of plasma electrons (I_e), plasma ions (I_i) and emitted electrons (I_{em}) at the plasma-material interface, obtained with CPIC and the FDM-CN solver of FONKS-G.

in response to a growth of the emission level. In fact, for a low enough value of β, the electrostatic potential profiles are monotonic at both the x-axis and the y-axis of the computational domain [see Figs. 3.6(a)-3.6(b)]. When β increases, a small potential well develops at the vertical axis of the computational domain [see inset in top-left panel of Fig. 3.6(c)], while the potential remains monotonic at the horizontal axis. As it will be discussed more in detail later in the present chapter (see Sec. 3.3.2.2), this is a further consequence of the correlation between the curvature of the object and the electric field along its surface. Eventually, when the emission level overcomes a certain threshold, the potential well grows and extends to the whole plasma-material interface, as depicted in the insets of the top-left panels in Figs. 3.6(e)-3.6(f). Regarding the comparison between the two codes, one observes that FONKS-G captures quite well this feature of the sheath, despite using a much lower spatial resolution than CPIC in the area surrounding Γ.

3.2 Limitations of stationary Vlasov-Poisson solvers

This section presents novel results related to the investigation of some *numerical* (see Sec. 3.2.1) and *physical* (see Sec. 3.2.2) limitations that affect stationary Vlasov-Poisson solvers based on the backward Liouville method. The analysis deals with both cylindrical and elliptical Langmuir probes facing a Maxwellian plasma that comply with the mathematical model outlined in Chapter 2. In particular, the configurations considered in the present analysis are described by the following set of physical parameters

$$b_p = 1,\ \phi_p = -4,\ \delta_i = 1,\ \delta_{em} = 0,\ \beta = 0, \tag{3.6}$$

and different values of the of the probe eccentricity e_p, which is conveniently used as integrability-breaking parameter. A thorough comparison among the different solvers of Table 2.4 allows not only to characterise deeply the properties of the different algorithms of FONKS-G, but also to derive a list of good practices that one might take into account when developing a VP solver based on the backward Liuoville method, with particular emphasis on how to identify an optimal value for N_{tr} (i.e., number of loops inside the

plasma sheath after which the trajectory a particle is classified as trapped) and how to deal with the filamentation of the distribution function in non-integrable systems.

3.2.1 Numerical limitations

This first type of limitations stems from numerical errors intrinsic to the various algorithms implemented in the code. For the problem at hand, such inaccuracies, which include discretization, interpolation, and integration errors, are not important for the majority of the Γ-originated and Γ_{max}-originated orbits. Connecting with either one of the two boundaries of the computational domain, the integration of these orbits typically lasts a short amount of time and the numerical error can be controlled by using adequate integration algorithms and selecting appropriately the time step. Therefore, numerical errors occurring along the integration do not have a significant impact neither on the origin of the trajectory, nor on the values of the invariant(s).

From a practical point of view, changing slightly the point where a trajectory crosses a boundary has little influence on the final solution. For Γ-originated trajectories, the algorithm set to zero the value of the distribution function regardless of the location of the impact, while for Γ_{max}-originated orbits the value is assigned according the boundary conditions of Eqs. (2.43a)-(2.43b), where the total energy is the one at the beginning of the integration. However, for long-lived trapped orbits, numerical errors tend to accumulate and a proper investigation of the properties of the algorithms is needed in order to select a good set of numerical parameters that allows to reach accurate-enough results. In fact, orbits that should be trapped might incorrectly end up at one of the boundaries of the computational domain and the corresponding value of the distribution function be set by the algorithm to a finite value rather than zero.

3.2.1.1 Conservation laws

The characteristics of the Vlasov equation [see Eqs. (2.38a)-(2.38b)], which coincide with the orbits of the charged particles inside the sheath of the probe, are a Hamiltonian system, whose Hamiltonian coincides with the total energy ε_α defined in Eq. (2.39). Being τ-independent, the Hamiltonian is a constant of motion of the system of Eqs. (2.38a)-(2.38b). For the particular case of a cylindrical body (i.e., $e_p = 0$), the equations of motion conserve the angular momentum of the charges as well. In view of the intrinsic inaccuracies affecting the numerical algorithms of the code, the invariant(s) of the system are not (in general) preserved exactly during its numerical integration, unless specifically designed schemes are used. Investigating the capability of the different integrators to recover these conservation laws provides a measure of their good implementation and their relative accuracy. In order to address this issue, the performances of the different numerical integrators of Table 2.4 were compared among each other.

Considering the configuration outlined by the physical parameters of Eq. (3.6) and $e_p = 0$, a first benchmark is carried out between the RK and CN orbital propagators

onto an unstructured and structured cylindrical meshes with $r_{max} = 7.5$, discretised with $N = 1893$ and $N_r \times N_\theta = 45 \times 45$ nodes, respectively. The latter is plotted in the physical space in the bottom-right panle of Fig. 2.3. For convenience, the VP-solver of Ref. [113] provided the electrostatic potential profile used as input for the reconstruction of the electric field. The latter was computed according to the polynomial fitting coupled with the Natural Neighbour Interpolation for the RK algorithm, while the B-spline procedure was used in the case of the CN orbital propagator (see Appendix D for details). Starting from the initial conditions $(x_0, y_0, \varepsilon_i) = (3.05, 0, 0.505)$, Fig. 3.7 shows the intersections with the $v_r = v_x \cdot \cos\theta + v_y \cdot \sin\theta = 0$ plane (Poincaré section) of the trajectories of trapped ions corresponding to five different values of the initial velocity angle ζ_0, identified by distinct combinations of markers and colours. In the left panel, the orbits computed with

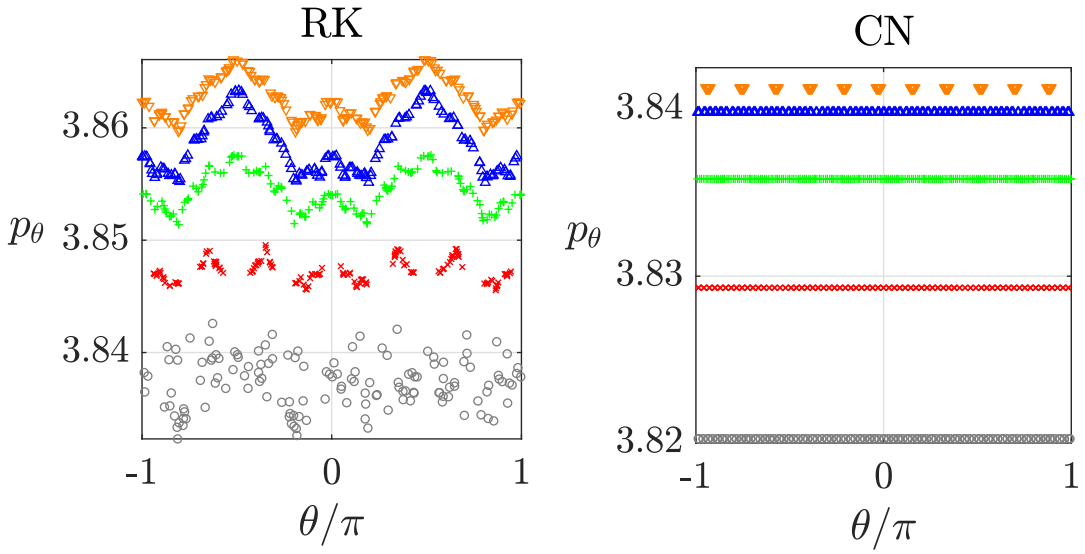

FIGURE 3.7: Poincaré section ($v_r = 0$ plane) of trapped ions moving around a cylindrical probe. Results are shown for initial conditions with $(x_0, y_0, \varepsilon_i) = (3.05, 0, 0.505)$ and five different velocity angles ζ_0, identified by different combinations of colours and markers. Left and right panels were obtained with the RK and the CN integrators, respectively [128].

the RK integrator and the unstructured mesh do not conserve exactly the angular momentum $p_\theta \equiv r v_\theta = -v_x \cdot y + v_y \cdot x$, which exhibits variations of approximately 1%. These small changes derive from small errors in the computation of the electric field along the trajectory, which result in a violation of the axial-symmetry of the physical configuration,

although the potential profile used as input strictly satisfies $\partial\phi/\partial\theta = 0$. On the contrary, the right panel reveals that using the CN algorithm and the cylindrical structured mesh is beneficial for this particular scenario, since a remarkably better conservation of the angular momentum is achieved. Regarding the discrepancy in the magnitudes of the initial p_θ, whose values are slightly higher in the case of the unstructured mesh, this is due to the fact that the initial point of the trajectory does not coincide with any of the nodes of the structured cylindrical mesh. As a consequence, the value of the electrostatic potential was interpolated. This resulted in a slightly different value of the total energy and, in turn, of the initial velocities. Given that the goal of the study is that of determining which of the two integrators conserves better the invariants of motion, this small difference is not relevant.

While the above discussed conservation of the angular momentum took advantage of a solution computed with the numerical scheme of Ref. [113], the conservation of the Hamiltonian was studied by finding the full solution of the Vlasov-Poisson system with the different solvers of FONKS-G for the configuration described by the parameters of Eq. (3.6) and $e_p = 0.95$. After setting the numerical parameters to

$$N_\zeta = 360, \quad N_{\varepsilon_\alpha} = 300, \quad \varepsilon_\alpha^{max} = \varepsilon_\alpha^{max} + 6.0, \quad N_{tr} = 2, \tag{3.7}$$

the simulations were run onto an unstructured and structured elliptical meshes with $r_{max} = 16$ and $N = 1898$, and $\xi_{max} \approx 7.26 \times \xi_p$ and $N_\xi \times N_\eta = 45 \times 45$, respectively (see top-left and bottom-left panels in Fig. 2.3). Recalling that the Hamiltonian of the system coincides with the total energy of the particles, its conservation was investigated by monitoring the relative error defined as $\Delta\varepsilon_i \equiv 100 \times \left[\varepsilon_i(\tau)/\varepsilon_i(0) - 1\right]$ along the trajectories of some trapped ions. The results are shown in Fig. 3.8.

In the left panel, one observes that the error corresponding to the FEM-RK solver (red solid line) presents oscillations with peaks of almost 10%, while its mean value undergoes a secular variation. Comparing such curve with the one obtained with the FDM-RK solver (dark gray dash-dotted line), whose magnitude does not exceed 3% and shows no secular variation, reveals that a discretisation of the physical space with a structured mesh, in tandem with a bi-linear interpolation technique for the reconstruction of the electric field, ensures better conservation properties than an unstructured mesh with natural neighbor interpolation. Substituting the RK integrator with a (symplectic) second-order LeapFrog (LF) scheme lead to analogous conclusions (see right panel of Fig. 3.8), and no significant improvement in the conservation of the energy was observed by halving the time step (for clarity, these two curves are not included in the plot). These results identify the algorithm used for the reconstruction of the electric field along the orbit as the main source of error for the conservation of the energy. Eventually, much better conservation properties are exhibited by the FDM-CN solver (blue dashed line in the left panel). In fact, this implicit method conserves the Hamiltonian up to the tolerance set by the user for the Newton method used to compute the state vector at subsequent time steps along the trajectory. Such value was equal to 10^{-8} in the computations that are being discussed.

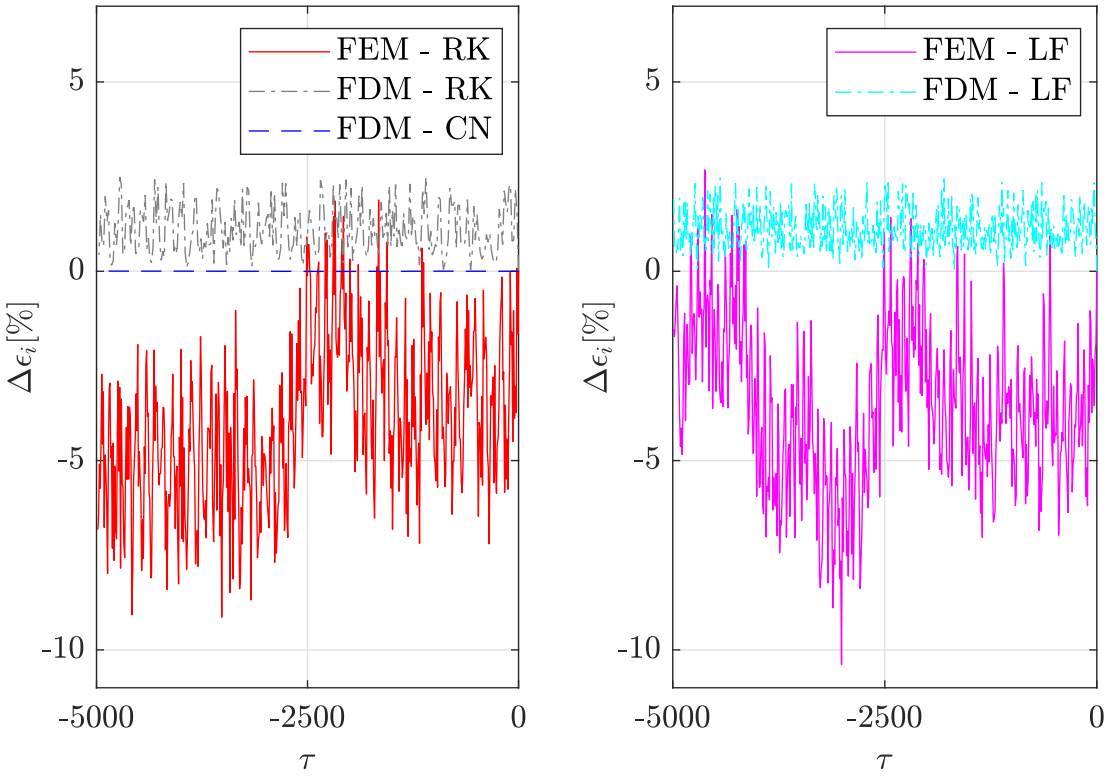

FIGURE 3.8: Evolution of $\Delta\varepsilon_i = \left[\varepsilon_i(\tau)/\varepsilon_i(0) - 1\right] \times 100$ for a trapped ion moving around an elliptic probe with $e_p = 0.95$. Different curves correspond to different solvers of FONKS-G [128].

3.2.1.2 Trapping criterion

The previous discussion about the conservation of the energy is very important for setting an appropriate trapping criterion and having a good understanding of the limitations of stationary VP solvers. As explained in Chapter 2, stationary solvers cannot assess the population of trapped particles, and their distribution function is thus set to zero regardless of their species. Since this population can play a significant role in the solution, it is thus of uttermost importance to identify a good criterion for classifying an orbit as trapped. In the present work, this is the role of N_{tr}, which is the numerical parameter that denotes the number of loops that an orbit must cover without connecting to the boundaries of the computational domain for being considered as trapped. The solutions of a well designed VP solver should not depend on the values of the numerical parameters, like the size of the computational domain and the resolution, provided that these values are selected above certain thresholds. For instance, this is the case of the numerical parameters governing the resolution of the discretisation of f_α in the phase space (N, N_{χ^1}, N_{χ^1}, N_ζ,N_ε, ε_{max}). However, the role of N_{tr} is subtler in this regard, and a more involved analysis is required to identify an optimum value.

To address this topic, the same numerical integrators and computational domains adopted during the investigation of the conservation of the angular momentum discussed above were implemented. Exploiting again the solution computed with the algorithm of Ref. [113], the different propagators were used to analyse the influence of N_{tr} on the structure of the ions distribution function of at point $(x,y) = (3.05,0)$. Figure 3.9 shows plots of a restricted portion of the velocity space, which was conveniently discretised with a high resolution grid of $N_\varepsilon \times N_\zeta = 100 \times 250$, where trapped particles are found.

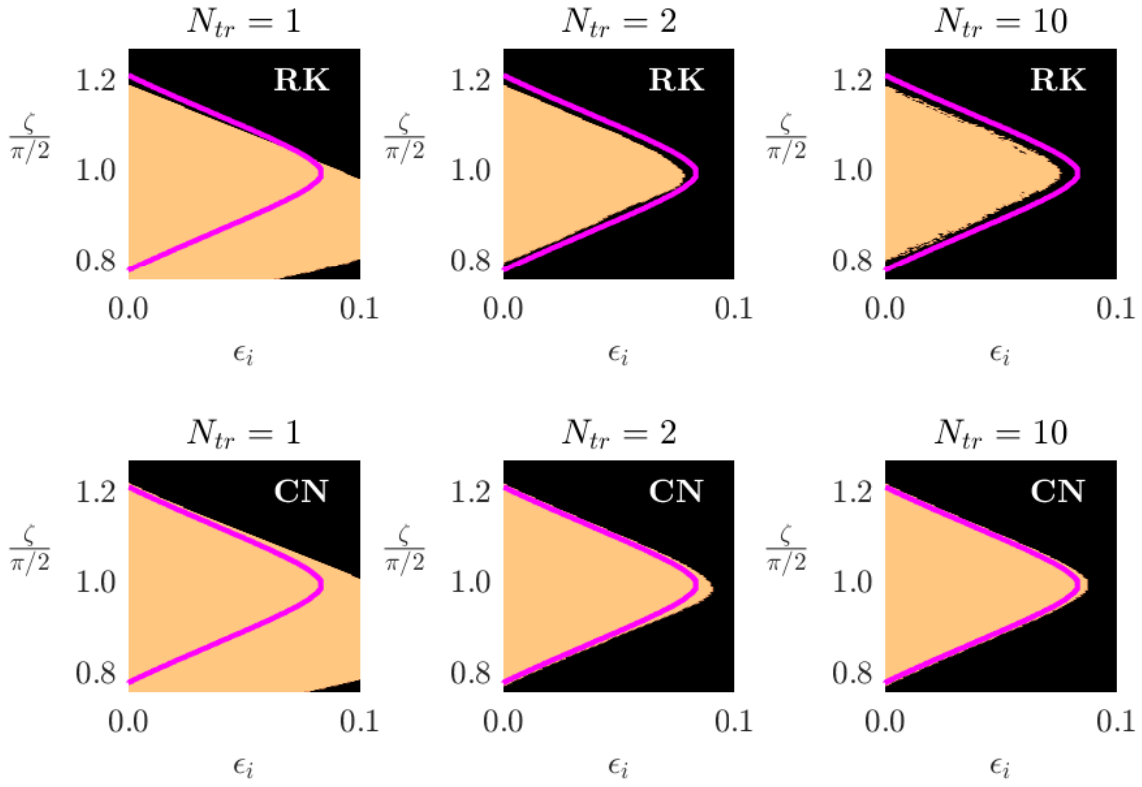

FIGURE 3.9: Distribution function at $(x,y) = (3.05,0)$ in the $\varepsilon_i - \zeta$ plane for different values of N_{tr} obtained with the RK (top) and CN (bottom) integrators. Orange and black regions identify initial conditions yielding trapped and Γ-originated orbits, respectively. The magenta line is the exact boundary computed with FONKS-C [128]. Research data and post-processing scripts are available at dataset [164].

Top panels represent the results obtained with the RK integrator and the unstructured mesh, while bottom panels correspond to the CN integator applied onto the structured cylindrical mesh. In the plots, the black area identifies the area where the distribution function has a finite positive value given by the Maxwellian (i.e., Γ_{max}-originated orbits), while the orange area includes initial conditions that yield trajectories that perform N_{tr} loops inside the sheath (i.e., trapped), for which the distribution function is set to zero. The magenta solid line provides a benchmark, as it represents the boundary between these two regions that is obtained with the algorithm of Ref. [113], which exploits the conservation

of both energy and angular momentum to compute the exact result without the need for explicit particle-tracking.

The left panels show that if N_{tr} is too low (equal to 1 in the present case), the algorithm incorrectly classifies an excessive amount of orbits as trapped regardless of the numerical integrator. An integration over the velocity space would thus result in an underestimation of the ion density. When N_{tr} grows, the ability of the orbital propagator to conserve the invariants of the system becomes more important. For $N_{tr} = 10$, the RK integrator ends up overestimating the density bacause some of the orbits that should be labeled as trapped are incorrectly classified as non-trapped. In fact, small numerical errors accumulate along the path, leading to the breaking of the conservation of ε_i and p_θ and ultimately to the deflection of these trapped trajectories, which end up connecting to the outer boundary of the computational domain.

An interesting side effect is that the boundary between trapped and non-trapped orbits becomes jagged, since there reside the conditions that most likely lead to the deflection of the trajectories due to the accumulated numerical errors. Using an algorithm with better conservation properties is thus beneficial in this case, as shown by the results obtained with the CN integrator, which captures with good accuracy the boundary even for high values of N_{tr} (see bottom right). Therefore, the solutions provided by a VP solver based on the CN integrator do not depend on N_{tr} provided that its value is high enough. Once a well-behaved algorithm is identified, a sensitivity analysis allows to compute the optimal value for N_{tr}. The latter should also account that N_{tr} has an impact on the computational cost as well.

3.2.2 Physical limitations

In contrast to their numerical counterpart discussed in the previous sections, physical limitations stems from the very nature of the problem and do not depend on the algorithm(s) implemented to solve it. Stationary descriptions of physical systems like the one outlined in Chapter 2, though useful for providing approximations of a wide variety of phenomena, cannot address properly certain features. In the following two sections a discussion of the consequences of neglecting the population of trapped particle and how to deal with the filamentation of the distribution function when the system becomes non-integrable are presented.

3.2.2.1 Trapped Particles

One of the most important limitations of stationary Vlasov (collisionless) solvers is their failure at dealing with the presence of trapped particles. In the majority of cases, this population is neglected. Coherently, this was the approach adopted in the present work. However, there are some circumstances in which simply disregarding the presence of trapped particle might interfere with the computation of a solution, whether not directly

preventing from finding one. The present section discusses three different scenarios in which the trapped particles have been shown to play a different role.

A first group includes systems which are not affected significantly by the disregarding of the population of trapped particles, whose effect is just that of slightly modifying the profile of the electrostatic potential profile. Therefore, a self-consistent solution to the Vlasov-Poisson system can be found even without taking into account the trapped population. For a cylindrical Langmuir probe immersed at rest in Maxwellian plasmas, comparisons between steady-state solutions [93] and solutions with trapped particles arising from collisions (i.e., stationary Boltzmann-Poisson solver [165]) or during transients (non-stationary Vlasov-Poisson solver [166]) proved this point.

A second category includes configurations in which ignoring trapped particles lead to convergence issues. A plasma expansion in a slender magnetic nozzle provides a good example. In fact, numerical solutions were found with a stationary Vlasov solvers only after including in the system a heuristic population of trapped electrons [167]. A more recent study implementing a non-stationary Vlasov solver showed that trapped electrons are indeed present [151], though in a much smaller fraction than the one considered in the stationary analysis.

Eventually, a third class involves physical scenarios in which the trapped particles are indispensable for finding a solution to the problem. To this last category pertains the case of a positively biased Langmuir probe immersed in a flowing plasma at mesothermal conditions. That is, with the flow velocity being large (small) with respect to the thermal velocity of the plasma ions (electrons). If no trapped particles are taken into account, the density of the attracted species should fall below the background density n_0 [108], but the density of the hypersonic (repelled) ions should exceed n_0 at the front side of the probe. In turn, quasi-neutrality would not hold over a broad region. As proposed in Ref. [168], simulations with a non-stationary Vlasov solver [169] showed that a population of trapped particle is in fact necessary for quasi-neutrality to be recovered at the front of the probe.

3.2.2.2 Filamentation

Since its Hamiltonian does not depend on τ, the total energy is a constant of motion of the 4-dimensional system given by Eqs. (2.38a)-(2.38b). In some particular cases, a second invariant can be identified. For instance, the sheath around a cylindrical object ($e_p = 0$) at rest inside a Maxwellian plasma features an axi-symmetric electrostatic potential and the angular momentum is conserved as well along the orbits. The effective dimension of the phase space thus reduces to $4-2=2$ and the system is said to be *integrable*, admitting only regular solutions. However, when the sheath around an elliptical ($e_p \neq 0$) probe is considered, the angular momentum is not conserved. The Hamiltonian system is non-integrable, because its effective dimension is $4-1=3$. Accordingly, non-regular (chaotic) dynamics can appear.

In order to investigate the impact of this feature, a solution for the configuration corresponding to the physical parameters of Eq. (3.6) and $e_p = 0.95$ was computed with the

FDM-CN solver, which showed the best performances in the analysis of Sec. 3.2.1.1. The structure of the plasma sheath was computed self-consistently, setting the numerical parameters in Eq. (3.7) and $N_{tr} = 2$. Afterwards, the electrostatic potential was exploited as input for investigating in detail the dynamics of trapped ions. For a fixed value of the total energy $\varepsilon_i \approx 0.062$, Fig. 3.10 shows the intersection with the plane $v_r = 0$ of different trapped orbits. Each color identifies a different set of initial conditions, all sharing the same value of energy. The resulting Poincaré section features a pair of two-lobed structures around $\theta = 0$ and $\theta = \pi$, though, for clarity, just one is shown in the plot. In constrast to the analogous plot obtained for a cylindrical probe in Fig. 3.7, p_θ is not a constant of motion and a mix of regular and chaotic orbits appears, with Poincaré-Birkhoff chains and chaotic layers highlighted in the inset.

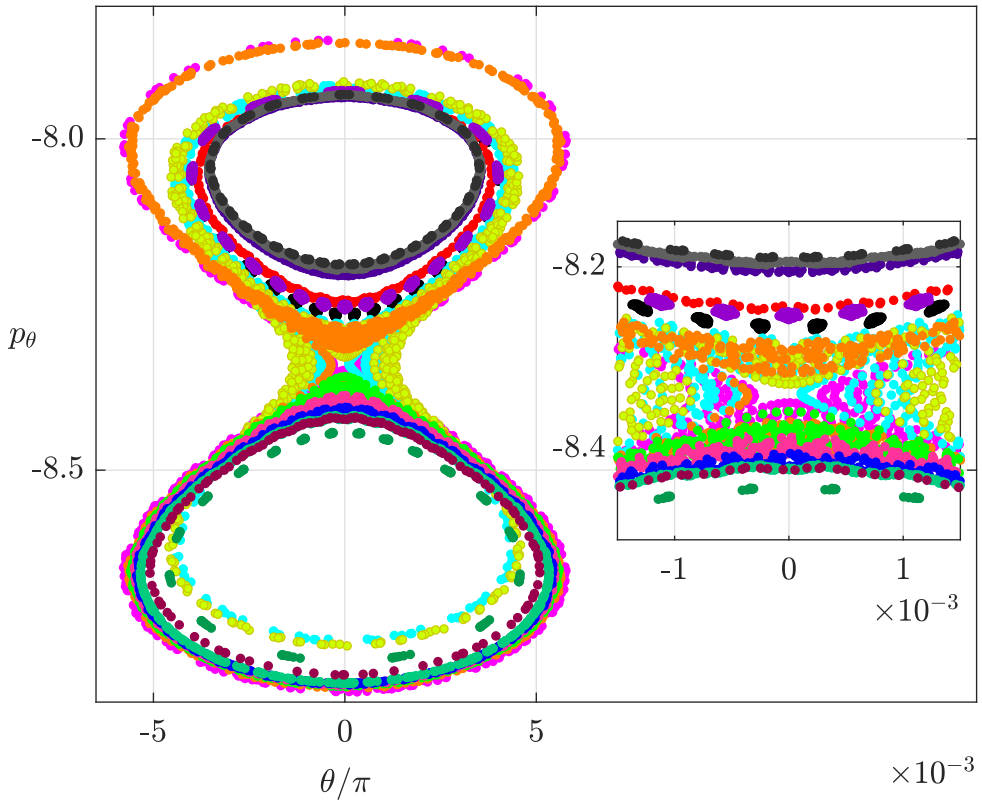

FIGURE 3.10: Poincaré section ($p_r = 0$ plane) of trajectories of trapped ions. All trajectories have $\varepsilon_i \approx 0.062$, but different sets of (x_0, y_0, ζ_0), each one identified by a different colour [128].

The appearance of chaotic orbits deeply affects the structure of the distribution function. This is evident in the high-resolution ($N_\varepsilon \times N_\zeta = 300 \times 300$) maps of Fig. 3.11, where orange, yellow and blue areas identify initial conditions yielding Γ-originated, Γ_{max}-originated and trapped (Tr) trajectories. These plots were obtained by setting $N_{tr} = 100$. For a cylindrical probe ($e_p = 0$), the presence of a second invariant of motion implies not

only that explicit integration of the orbits becomes unnecessary for the computation of the distribution function [113], but also that the boundaries separating different types of trajectories in velocity space are smooth curves, as shown in panel (a). When the system becomes non-integrable ($e_p \neq 0$), such boundary becomes irregular and the distribution function presents increasingly complex structures for higher values of the probe eccentricity [see panels (b), (c) and (d)].

For a moderate elongation ($e_p = 0.75$), the boundaries separating trapped from non-trapped particles are jagged and some empty spots start emerging in the otherwise yellow area. When the eccentricity further increases ($e_p = 0.90$), an additonal population of Γ-originating ions appears in view of the larger perimeter of the ellipse (see discussion in Sec. 3.3.2.1) and the boundaries becomes more complex. At $e_p = 0.95$ [panel (d) and the detailed region in panel (e)], the different types of trajectories deeply mix in velocity space and the distribution function is highly filamented, with boundaries between different areas showing a fractal structure.

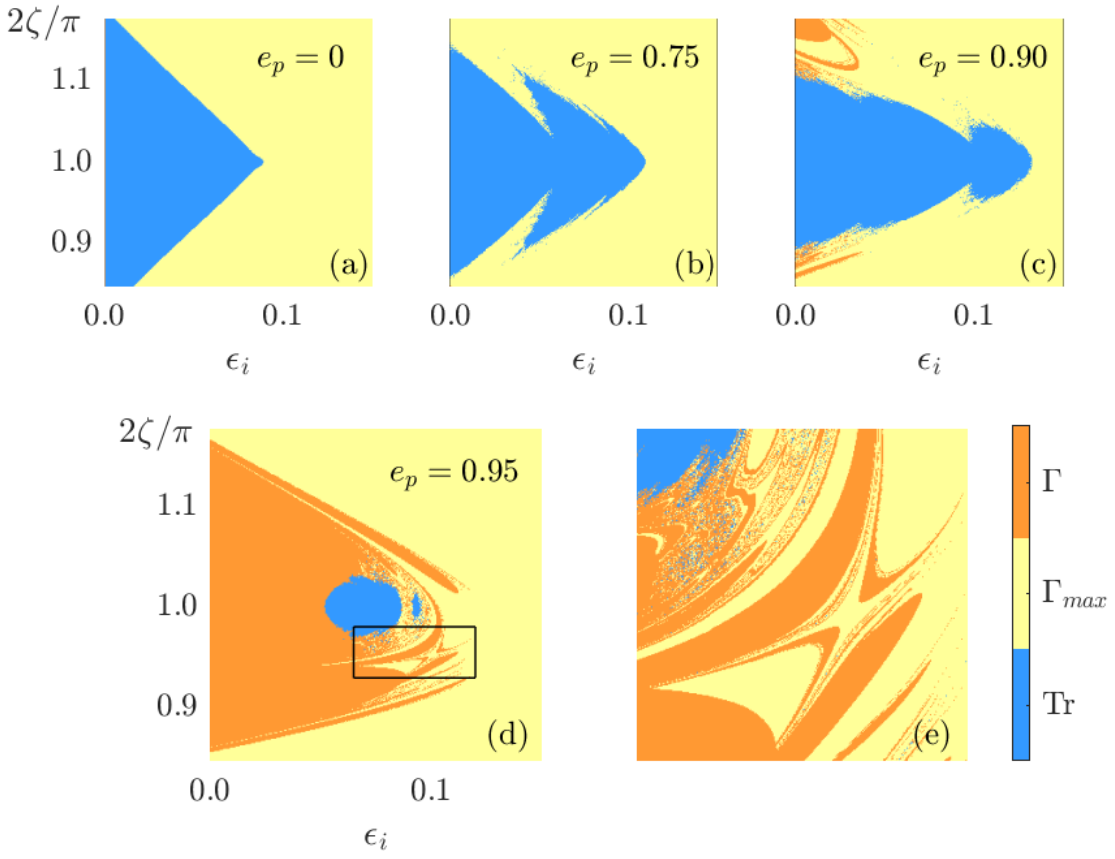

FIGURE 3.11: Ions distribution function at $(x,y) \approx (3.4,0)$ in the $\varepsilon_i - \zeta$ plane for $e_p = 0$ (a), $e_p = 0.75$ (b), $e_p = 0.9$ (c), and $e_p = 0.95$ (d). Panel (e) shows a detail of the region marked with a rectangle in panel (d). Orange, yellow and blue colours identify Γ-originated, Γ_{max}-originated and trapped orbits, respectively [129].

This feature was further investigated by considering in detail the ion distribution function at $(x,y) = (3.54,0)$ and $\varepsilon_i \approx 0.062$. Keeping fixed the value of the energy, a high resolution grid was used for discretising a small ζ-range ($1.57 \leq \zeta \leq 1.77$). As shown in Fig. 3.12, the same color scheme of Fig. 3.11 was implemented to mark the values of ζ corresponding to different types of orbits. As anticipated, the boundary in the ζ-axis between trapped and Γ-originated orbits exhibits a complex geometry. The investigation at smaller scales (using a resolution 10 times bigger) displayed in the insets clearly shows that a mix of the two types of orbits exists. Nonetheless, the distribution function around this boundary is smooth since, according to the model outlined in Chapter 2, in both cases the algorithm sets $f_i = 0$. However, the same does not hold for the boundary that separates Γ-originated orbits from the ones reaching the plasma boundary Γ_{max}, which also shows a complex structure (see right insets). There, the distribution function is filamented, with its value jumping continuously between zero and a positive scalar given by the Maxwellian.

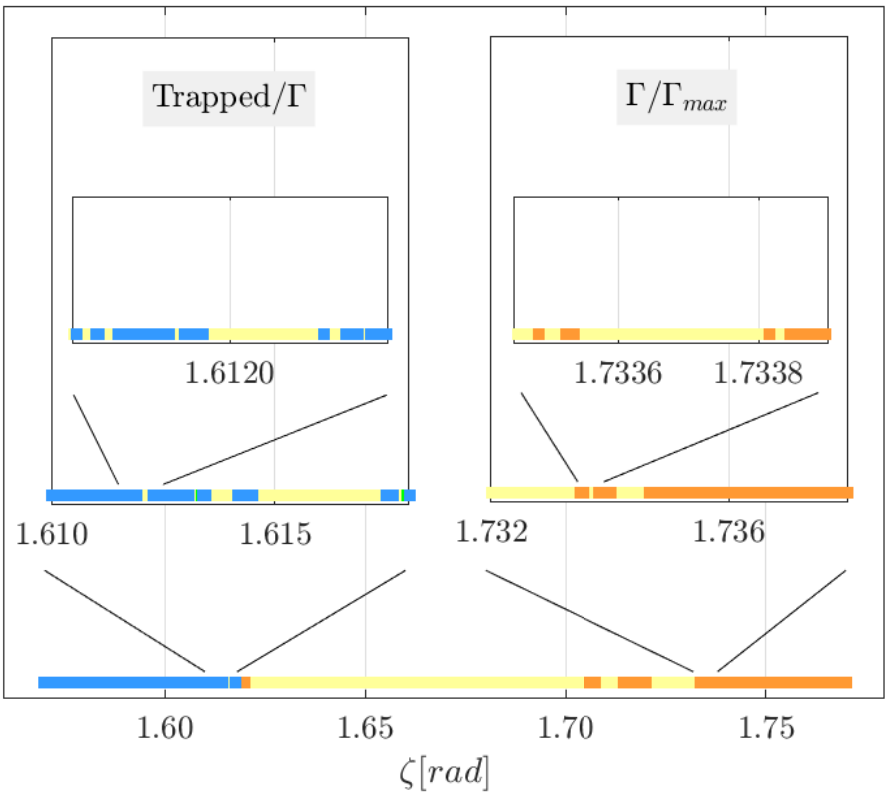

FIGURE 3.12: Structure of the ion distribution function at $(x,y) = (3.54,0)$ with $\varepsilon_i \approx 0.062$. Insets show details of selected regions along the boundaries between trapped and Γ-originated orbits (left) and Γ-originated and Γ_{max}-originated (right) orbits [128]. Research data and post-processing scripts can be found at dataset [164].

3.3 Parametric analysis

This section presents a parametric analysis of the characteristics of the sheath around electron-emitting prisms with elliptic cross-sections. The targeted configurations span over a wide range of parameters that are representative of ionospheric plasma and can be relevant for applications in both plasma physics (e.g., elongated dust grains) and aerospace engineering (e.g., LWTs applications). Considering a LEO environment, a reference scenario is outlined by setting the values of the plasma density to $n_0 = 10^{11}\mathrm{m}^{-3}$ and temperatures $T_e \approx T_i \approx 0.15\mathrm{eV}$ (i.e., $\delta_i = 1$), which give a Debye length of $\lambda_D \approx 1\mathrm{cm}$. The analysis aims at filling the theoretical gap between the OMT for probes with cylindrical and tape-like cross-sections, focusing especially on the investigation of the transition between different operational regimes. It was already stressed that evaluating the impact of SCL conditions is important for assessing the performance of an LWT device. To this extent, the analysis is limited to moderate (negative) values of ϕ_p, while the emission level β varies considerably.

3.3.1 Sheath structure

This sub-section discusses the macroscopic characteristics of the plasma sheath around ellipses of different geometrical properties. First the impact of modifying the eccentricity is investigated by setting the physical parameters to

$$0 \leq e_p \leq 0.99, \quad \phi_p = -4, \quad b_p = 1, \quad \delta_i = 1, \quad \delta_{em} = 0, \quad \beta = 0. \tag{3.8}$$

Figure 3.13 shows the net charge density ρ. Analogously to what was done in Sec. 3.1.2, the profiles are plotted at the x- [panel (a)] and y- [panel (b)] axes separately. For the cylindrical ($e_p = 0$) case (dark gray lines with circular markers), which was computed with the algorithm of Ref. [113] and will be adopted as benchmark for the rest of the results, one observes that the charge density first grows to a peak in the region close to the plasma-material interface, and then decreases monotonically along the remaining part of the domain. Corresponding to a cylinder, such curves are the same in panel (a) and panel (b). On the contrary, the profiles tend to differ in the region close to Γ when $e_p > 0$, since axial-symmetry no longer holds. Intuitively, both the discrepancy between the profiles at $y = 0$ and $x = 0$ and the extension of the sheath grow with e_p. Since the effect of the specific geometry of the probe vanishes as $r \to \infty$, higher values of e_p require the use of larger computational boxes (i.e., bigger L_ξ).

The slenderness of the object has an impact on the location and magnitude of the maximum value of the charge density as well. The former occurs closer to the plasma-material interface when e_p grows, this effect being more pronounced at the semi-minor ($x = 0$) axis of the ellipse. For $e_p = 0.99$, one observes that the maximum basically lies on Γ and the charge density decreases almost monotonically across the entire domain. Regarding the magnitude, the intensity of the peak is barely constant up to $e_p = 0.95$ at the semi-major ($y = 0$) axis, while it diminishes when the eccentricity approaches to one in view

of a growth in the number of Γ-originated ions orbits. At $x = 0$, the maximum decreases monotonically with the eccentricity as the probe gradually enters the non-OML regime (see Sec. 3.3.2.1 for more details).

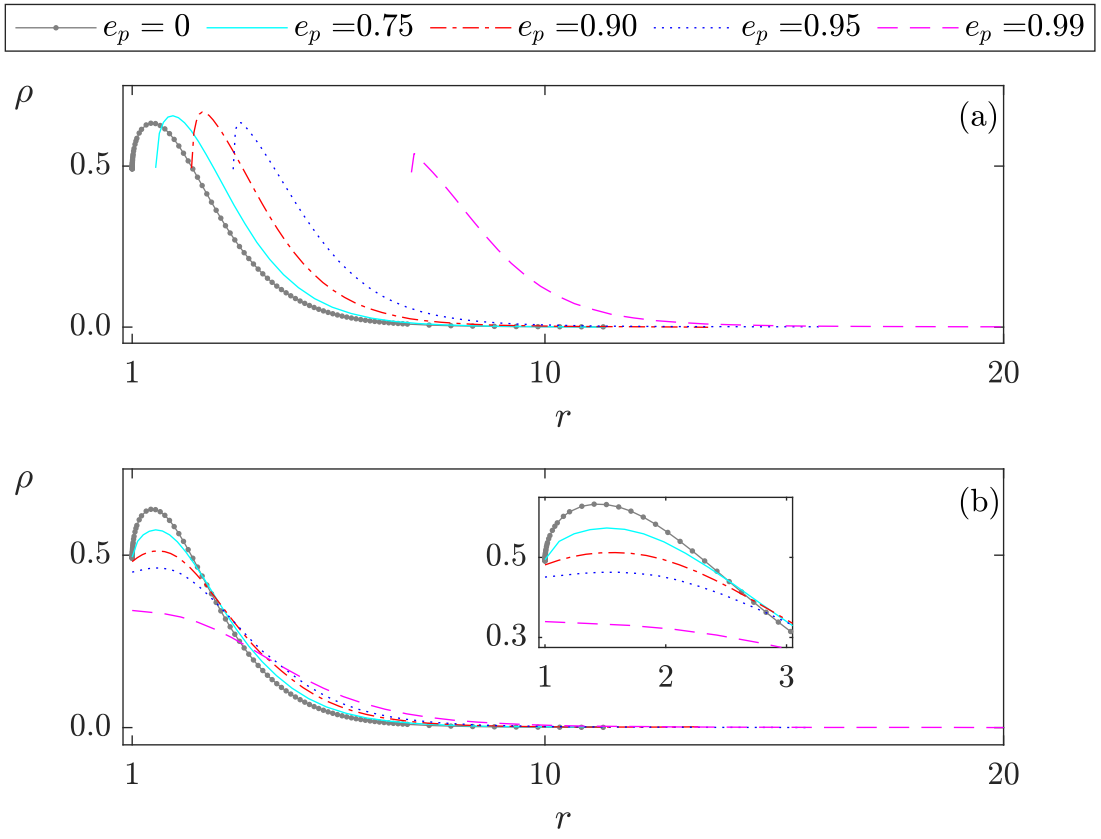

FIGURE 3.13: Space charge at the $y = 0$ [panel (a)] and $x = 0$ [panel (b)] axes for the set of parameters given in Eq. (3.8) and several values of e_p, identified by different combination lines and colours [129].

Four simulations of the configurations having

$$\begin{aligned} &e_p = 0.75, \quad \phi_p = -5.0, \quad 1 \leq b_p \leq 3, \\ &\delta_i = 1.0, \quad \delta_{em} = 0.32, \quad \beta = \{0,\ 1.72\}. \end{aligned} \tag{3.9}$$

were run to study the influence of the characteristic-size-of-the-object-to-Debye-length ratio (b_p) and the intensity of electron-emission (β) on the structure of the sheath. Figure 3.14, which is divided into four quadrants, shows the map of the density of the ions in a region close to Γ. Being the eccentricity $e_p = 0.75$, one immediately observes that the density varies in the azimuthal direction. A comparison of the results relative to a non-emitting body (top panels) with those in presence of emission (bottom panels) reveals that the dependence on the azimuthal angle becomes more evident in the latter case, especially in proximity of the horizontal axis of the domain. On the contrary, increasing the characteristic dimension of the probe yields the opposite effect. A comparison between the

panels on the left ($b_p = 1$) and those on the right (b_p) shows that, for a given value of emission, the sheath is less sensitive to the particular shape of Γ when the size of the body increases. Arguably, this is due to the local curvature [see definition in Eq. (A.3)] of the plasma-material interface diminishing with b_p. Looking at the trend across the computational domain, one observes that the growth of n_i is much slower for bigger probes. For instance, the map depicted in the top-right panel ($\beta = 0$) features a wide region where the density of the ions is below 0.6 times the background plasma density. It is thus safe to state that the extension of the sheath is higher when the dimensions of the body grows, a result consistent with previous findings on infinite cylinders [72, 93, 123].

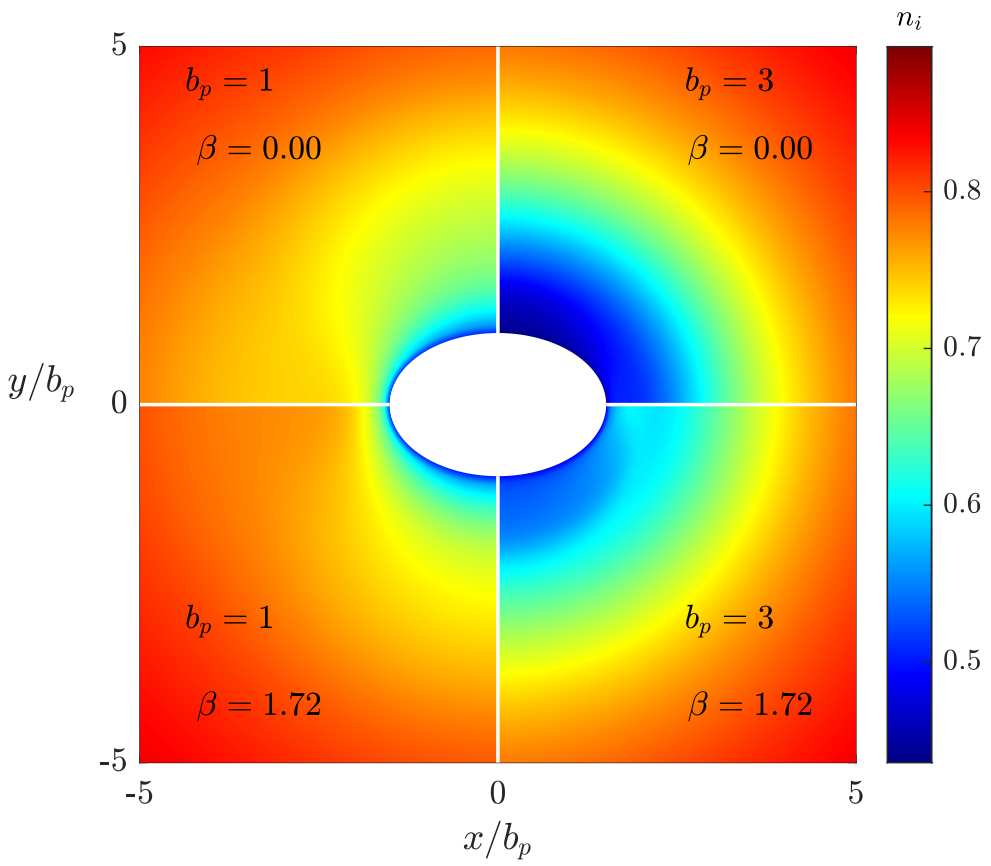

FIGURE 3.14: Detail of the density of attracted ions inside the plasma sheath corresponding to the set of parameters given in Eq. (3.9) [129].

In order to understand this last effect, it is necessary to analyse the component of the electric field normal to the ellipse confocal to Γ at each point of the mesh, shown in Fig. 3.15. Being the bias of the probe negative, the ions see a (negative) electric force directed inward. An analysis of the orbits of the ions reveals that, the stronger the electric field and the larger the object, the higher the number of Γ-originated trajectories. In turn, this reflects in the density of the attracted species being lower. Comparing the left and right panels of fig. 3.15, it is observed that the component of the electric field directed towards

the plasma-material interface increases with b_p. On the contrary, electron emission (bottom panels) smooths out the electric field, resulting in an increased density of the ions in the sheath.

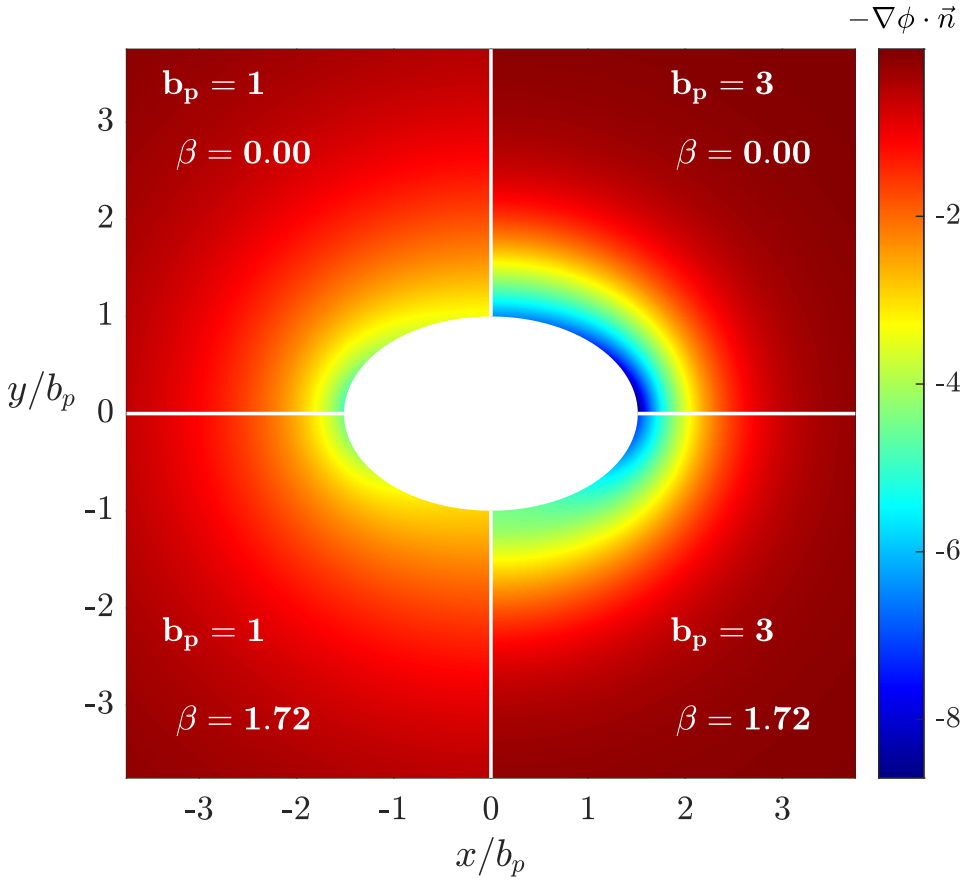

FIGURE 3.15: Normal component of the electric field corresponding to the set of parameters given in Eq. (3.9) [129].

3.3.2 Operational regimes

This section analyses the different operational regimes in which current collection and electron emission from elliptic negatively polarised probes fall. In particular, transition between different regimes is investigated by varying, one at a time, the eccentricity (e_p), the size relative to the Debye length (b_p) and the level of electron-emission (β) of the body.

3.3.2.1 Transition between OML and non-OML operational regimes

An object immersed in a Maxwellian plasma operates in the Orbital Motion Limited (OML) regime when the sheath associated to its presence does not feature any barrier

of effective potential, which would hinder some of the attracted particles from reaching the plasma-material interface [108]. Therefore, the OML conditions represent a maximum condition for current collection and, under such circumstance, some fundamental results hold. For a two-dimensional arbitrarily-shaped object with a negative bias relative to the plasma operating under OML conditions, the density and net current of the attracted species (i.e., positive ions) at the object are given by

$$n_i^{OML}(\Gamma) = \frac{1}{2}, \tag{3.10}$$

$$j_i^{OML}(\Gamma) = \sqrt{\frac{\delta_i}{\mu_i}}\left[2\sqrt{-\frac{\chi_\alpha}{\pi}} + \exp(\chi_i)\cdot erfc(\sqrt{\chi_i})\right], \tag{3.11}$$

where $\chi_i \equiv -\phi_p/\delta_i$ [108]. Analytical relations such as those in Eqs. (3.10)-(3.11) are very useful in plasma-material interaction problems and considerable efforts in the past were targeted at determining the range of physical parameters under which an object meets OML conditions. Relevant theoretical results were obtained for configurations involving non-emitting cylinders, thin tapes and infinite prisms with convex and concave cross-sections in the high bias limit [94, 122], and spheroids in the Laplace limit [108]. In presence of emission, a recent work has identified the validity of the OML regime for infinite-cylinders [162]. In the following paragraphs, the VP solver described in Chapter 2 was used to revisit some of these previous results, which typically rely on asymptotic analysis and compliance to a certain set of sensible hypotheses. Relaxation of some of the latter allows also to address to a higher degree of detail the impact of the object shape and the electron emission on the plasma sheath.

Slenderness of the object Simulating the configurations defined by the set of physical parameters of Eq. (3.8) for several values of e_p helps to understand the impact of the eccentricity of the ellipses onto the current collection operational regime. To this extent, panels (a) and (b) in Fig. 3.16 show the electrostatic potential, normalised to ϕ_p, at the vertical ($x = 0$) and horizontal ($y = 0$) axes of the computational domain. Recalling that, for $e_p = 0$, the OML condition reads $r_p^2\phi_p \leq r^2\phi(r)$ [i.e., Equations (3.10)-(3.11) hold provided that the potential profiles do not cross the diagonal], it was decided to follow Ref. [94] and plot ϕ/ϕ_p curves against a_p^2/r^2 and b_p^2/r^2, respectively, with $a_p = b_p/\sqrt{1-e_p^2}$ the dimensionless semi-major axis of the ellipses. For convenience, the non-OML region for cylinders is highlighted in yellow in the plots. Panel (a) and its inset show that the profiles enter such region when e_p grows. Nonetheless, this do not imply that the current collected by ellipses falls beyond the OML regime. In fact, panel (c), which displays the ratio j_i/j_i^{OML} for the different configurations considered, shows that current collection meets the predicted OML value up to $e_p = 0.90$, despite their corresponding electrostatic potential profiles enter the yellow area mentioned above. Therefore, the OML condition for cylinders does not hold for an elliptic geometry.

For the physical parameters of Eq. (3.8), the transition between the OML and non-OML operational regimes lies within the interval $0.90 \leq e_p \leq 0.95$. As anticipated in Sec. 3.1.2, this result aligns with the outcome of a study by Laframboise and Parker [108], who predicted such transition to happen for oblate spheroids of aspect ratio 2.537 ($e_p \approx 0.92$) in the Laplace limit. For increasingly higher values of e_p, the shape of the object approaches that of a tape and the ratio j_i/j_i^{OML} keeps decreasing, reaching a minimum of ≈ 0.88 for the cases taken into account. Such minimum is considerably lower than the value obtained with the asymptotic analysis of Ref. [94], which predicted a drop in the current collection in the order of 1% for thin tapes at high biased relative to the plasma. The magnitude of the bias mitigates the influence of the geometry of Γ on the current collection. In addition, an elongated shape might actually be beneficial for current collection even if OML current collection no longer hold. In fact, for a fix value of b_p, the growth in the perimeter of Γ [see Eq. (2.48)] with the eccentricity effectively counteracts the reduction in j_i induced by its shape. For instance, one finds $p\,|_{e_p=0.99} = 4.9 \times p\,|_{e_p=0}$ and $p\,|_{e_p=0.99} = 2.71 \times p\,|_{e_p=0.9}$.

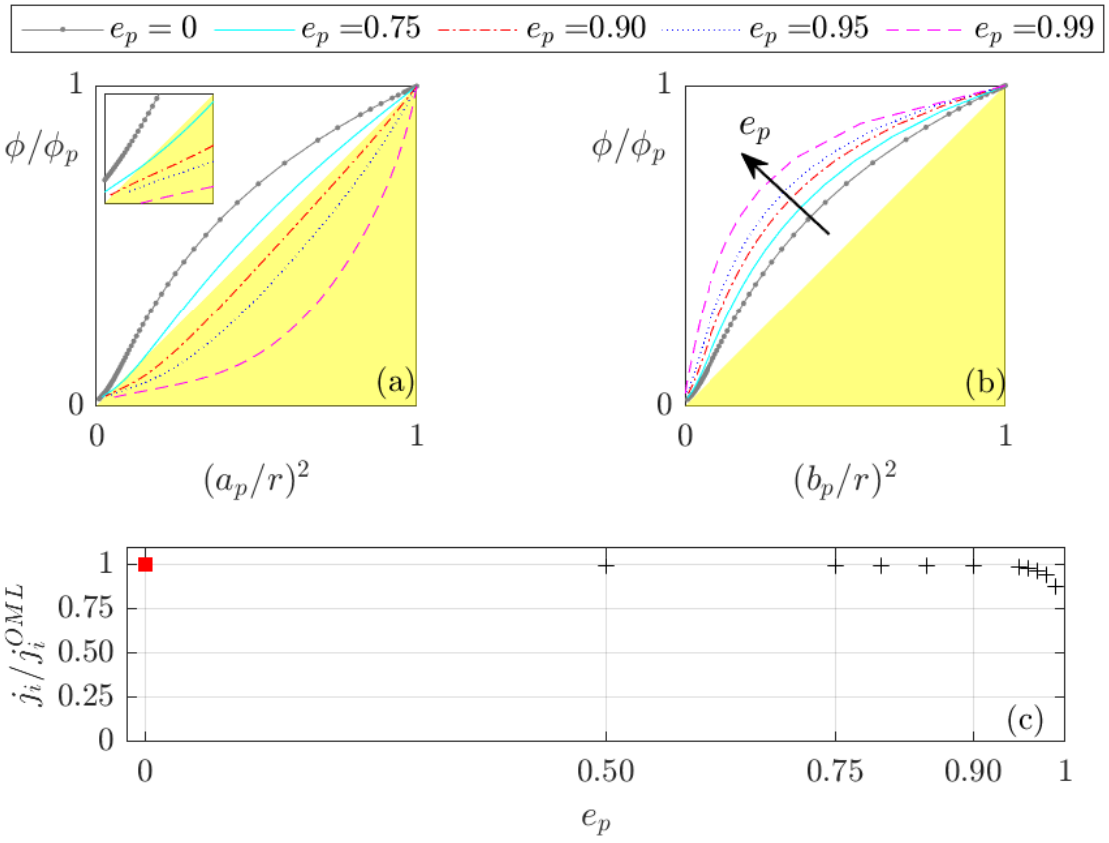

FIGURE 3.16: Electrostatic potential at the $y = 0$ [panel (a)] and $x = 0$ [panel (b)] axes for for the set of parameters given in Eq. (3.8) and several values of e_p, identified by different combination lines and colours. Collected current-to-OML current ratio versus the eccentricity [panel (c)]. The red squared marker provides a reference value computed with FONKS-C for a cylindrical probe [129].

To further characterise the impact of the shape of the object on the current collection, it is also interesting to analyse the distribution of the current along the plasma-material interface. Panel (a) in Fig. 3.17 displays the ratio $j_s(\gamma)/j_s^{OML}$ versus the eccentric anomaly γ [see Eqs. (2.49), (A.1a)-(A.1b)]. Since the configuration is symmetric with respect to both Cartesian axes, only a quarter of the ellipse is considered. Before analysing the results, the authors of Ref. [129] (the first one being the author of the current manuscript) would like to take the opportunity to provide an *errata corrige* regarding Fig. 5 of this very work. While reviewing the results published at Ref. [129] in order to adapt them for the redaction of the present manuscript, a typo was detected in the code script used to post-process the data shown in Fig. 5. In particular, the value of γ (referred to as θ in Ref. [129]) provided was incorrect. Therefore, panel (a) in Fig. 3.17 provides the actual curves obtained from the analysis of the distribution of the current along the perimeter of Γ. A thorough double-checking of the rest of the results presented in Ref. [129] proved that these are not affected by the error. All the conclusions drawn are still valid, except the one concerning the correlation between the minimum current collection and the maximum rate of change of the curvature.

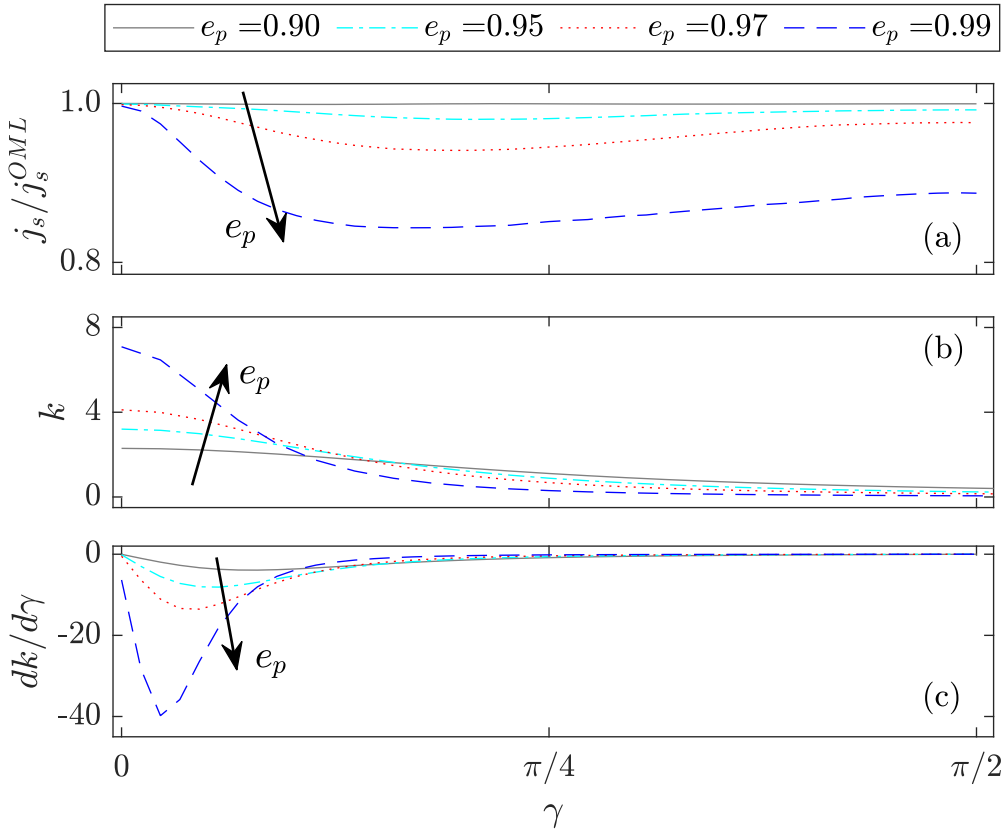

FIGURE 3.17: Ratio $j_s(\gamma)/j_s^{OML}$ (a), curvature k (b) and $dk/d\gamma$ (c) versus γ for different values of e_p, identified by different combinations of lines and colours. *Errata corrige* of Fig. 5 in Ref. [129].

Back to the discussion of the results, current collection is uniform along Γ up to $e_p = 0.90$ (dark grey solid line), which is the range of parameters for which OML conditions hold. However, for bigger values of e_p, ions are not collected uniformly along the plasma-material interface. At $(x,y) = (a_p, 0)$ (i.e., $\gamma = 0$) the current per unit area is that predicted by the OML. Then, the ratio $j_s(\gamma)/j_s^{OML}$ decreases along Γ, reaching a minimum that displaces closer to $\gamma = 0$ and becomes deeper as e_p grows. Eventually, the current collected grows back monotonically with γ up to a value lower than 1 and barely constant for $\gamma > \pi/4$. Along the plasma-material interface, points collecting OML and non-OML current coexist. This outcome is in agreement with the charge density profiles shown in panels (a) and (b) of Fig. 3.13. Since the density of the repelled species is negligible at Γ, one has that the charge density at the probe boundary is equal to $\rho(\Gamma) \approx n_i(\Gamma) = 0.5$ at the semi-major axis, which coincides with the OML condition of Eq. (3.10). On the contrary, at the semi-minor axis ($x = 0$) one finds $\rho(\Gamma) < 0.5$, which implies that some of the attracted particles are prevented from reaching that portion of the probe.

The trend of $j_s(\gamma)/j_s^{OML}$ versus γ correlates significantly with that of the local curvature k in panel (b) [see its definition in Eq. (A.3)]. Close to $\gamma = 0$, the curvature is high and the collected current approaches the OML value. Moving rightward, both j_s and k diminishes following similar trend. In the region where γ approaches $\pi/2$, the curvature is low. There, the ellipse is no longer *convex enough* to meet OML current collection, though the point of minimum current collection does not coincide exactly with $(x,y) = (0, b_p)$. Originally, it was thought that such minimum occured where the derivative $dk/d\gamma$, shown in panel (c), is maximum in magnitude. However, after fixing the typo in the post-processing script as discussed above, this correlation happens no longer to hold. Nonetheless, the results of the analysis prove that the geometry of the plasma-material interface has a significant impact on the current collection, particularly when its distribution along the perimeter is concerned. Being able to assess this kind of correlation is a key aspect in applications involving plasma-sheath lenses [119–121].

A deeper understanding of the behaviour of the ratio $j_s(\gamma)/j_s^{OML}$ requires an analysis of the ion distribution functions. For convenience, the analysis is made in the $\varepsilon_n - \varepsilon_t$ [123, 127] defined as

$$\varepsilon_n \equiv \varepsilon_\alpha \cdot \cos\zeta \tag{3.12}$$

$$\varepsilon_t \equiv \varepsilon_\alpha \cdot \sin\zeta, \tag{3.13}$$

Panels (a) and (c) in Fig. 3.18, which is adapted from Fig. 6 in Ref. [129], display the ion distribution function for $e_p = 0.99$ and $e_p = 0.95$ at the point along Γ where the current collected is minimum. Since a point pertaining to the plasma-material interface is considered, and no ions are emitted from such surface, both diagrams feature an empty region for $\varepsilon_n > 0$, which corresponds to outgoing particles. A second unpopulated region is present in both diagrams in the quadrant defined by $\varepsilon_n < 0$ and $\varepsilon_t < 0$. This second empty region becomes larger for higher eccentricities, therefore explaining the lower value of the current collected by the probe with $e_p = 0.99$.

A detailed analysis regarding the particle orbits in panel (b), which correspond to the

initial condition identified by labels A and B in panel (a), allows to understand why such is the case. In view of the elliptic geometry, trajectories with $\pi \leq \zeta \leq 3\pi/2$ follow a long path across a vast area close to the probe boundary, which exerts an attractive force on the charges, thus deflecting them towards Γ. For a fixed value of energy, the closer ζ is to $3\pi/2$, the more likely the origin of the trajectory pertains to Γ [see orbit B in panel (b)]. The resulting empty region in the third quadrant shrinks when the energy grows, for high-energetic particles are less prone to be deflected towards the plasma-material interface [see panel (c)]. Intuitively, the length of the trajectory running along the perimeter of the probe increases with e_p, thus resulting in a higher number of Γ-originated orbits for bigger eccentricities.

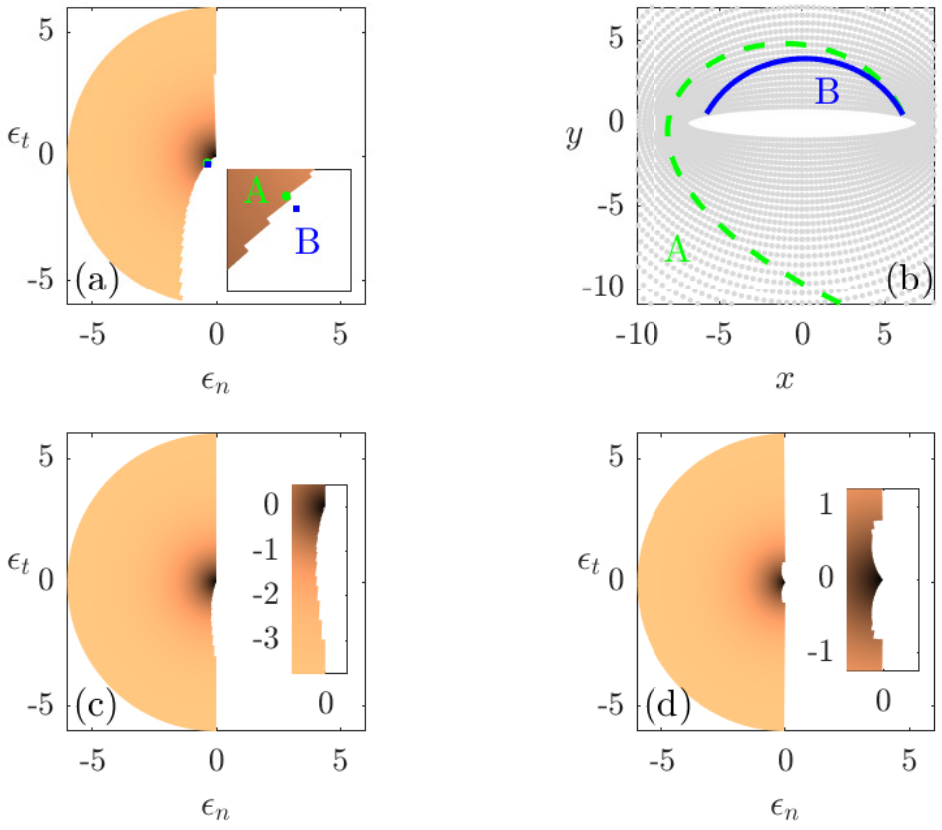

FIGURE 3.18: Ion distribution functions for $e_p = 0.99$ (a) and 0.95 (c) evaluated at the point along Γ where $j_s(\gamma)/j_s^{OML}$ in panel (a) of Fig. 3.16 is minimum. Panel (b) shows two orbits for the initial conditions labelled with *A* and *B* in panel (a). Panel (d) displays the ions distribution function at Γ for a cylinder ($e_p = 0$) of perimeter equal to that of the ellipse considered in panel (a) [129].

Panel (d) shows that a cylinder with radius such that its perimeter is equal to that of an ellipse of $e_p = 0.99$ (i.e., the most eccentric probe considered in the present analysis) also operates under non-OML conditions. In fact, the diagram of the distribution function features two unpopulated regions that are, in view of the axial symmetry of the configuration, symmetric with respect the ε_t-axis. In order to complete the analysis regarding

the impact of the shape, it is interesting to compare the amount of current collected by these two objects. Despite the distribution function of the cylinder presents a pair of Γ-originated regions, their impact on the current collection is smaller overall. In fact, one has $j_i\,|_{e_p=0} = 1.08\, j_i\,|_{e_p=0.99}$, meaning that the current collected by a cylinder is higher for a given perimeter.

Characteristic size A biased object is known to operate under OML conditions when its shape is convex enough and its characteristic dimension is small relatively to the Debye length [108]. This section presents a quantitative analysis of the impact of this second aspect for a set of ellipses with

$$e_p = \{0,\ 0.5,\ 0.75\} \quad 1 \leq b_p \leq 3,$$

immersed in the Maxwellian plasma consistent with the physical parameters $\delta_i = 1.0$, $\phi_p = -5$, $\delta_{em} = 0.32$. Panels (a) and (b) in Fig. 3.19 display the ratio j_i / j_i^{OML} versus the characteristic size b_p for an emission level $\beta = 0$ and $\beta = 1.72$, respectively. Different combinations of colours, style of lines and markers correspond to different probe eccentricities, with markers identifying the configurations that were simulated. For the three eccentricities, in absence of emission ($\beta = 0$), the current collected coincides (up to the numerical accuracy of the VP solver) with the value predicted by OML theory when b_p is small. However, when the size of the probe increases, the attracted particles travels on longer orbits in regions near Γ where the intensity of the electric field is stronger (see Fig. 3.15). Subsequently, they are more prone to end up at the probe boundary Γ, thus not contributing to the distribution function. When this happens, the current collected falls below the OML value and the probe operates under non-OML conditions.

When a cylindrical probe is considered ($e_p = 0$, dotted black lines with round markers), the transition starts at a radius which is approximately 1.5 times the Debye length [162], and the current gradually decreases as b_p increases, though the discrepancy with the OML value remains small even for the highest value of radius considered. These results, which are found for $\phi_p = -5$, extend to low-bias conditions the analytical results obtained in the limit of high-biases in Ref. [109].

As compared to a cylinder with the same plasma conditions, ellipses not only enter the non-OML operational regime at lower values of b_p, but also exhibit a steeper reduction in the current collected. Nonetheless, the overall reduction remains limited, as doubling and tripling b_p in the worst case scenario ($e_p = 0.75$) induces a drop in the order of 2% and 5%, respectively. Similar conclusions were found in previous analyses that took into account thin tapes [123] and 2-dimensional prisms of arbitrary shape in the limit of high-bias [122]. Overall, the results of the present and previous analyses show that the geometry of Γ (i.e., its eccentricity) has a bigger impact on current collection than its characteristic size.

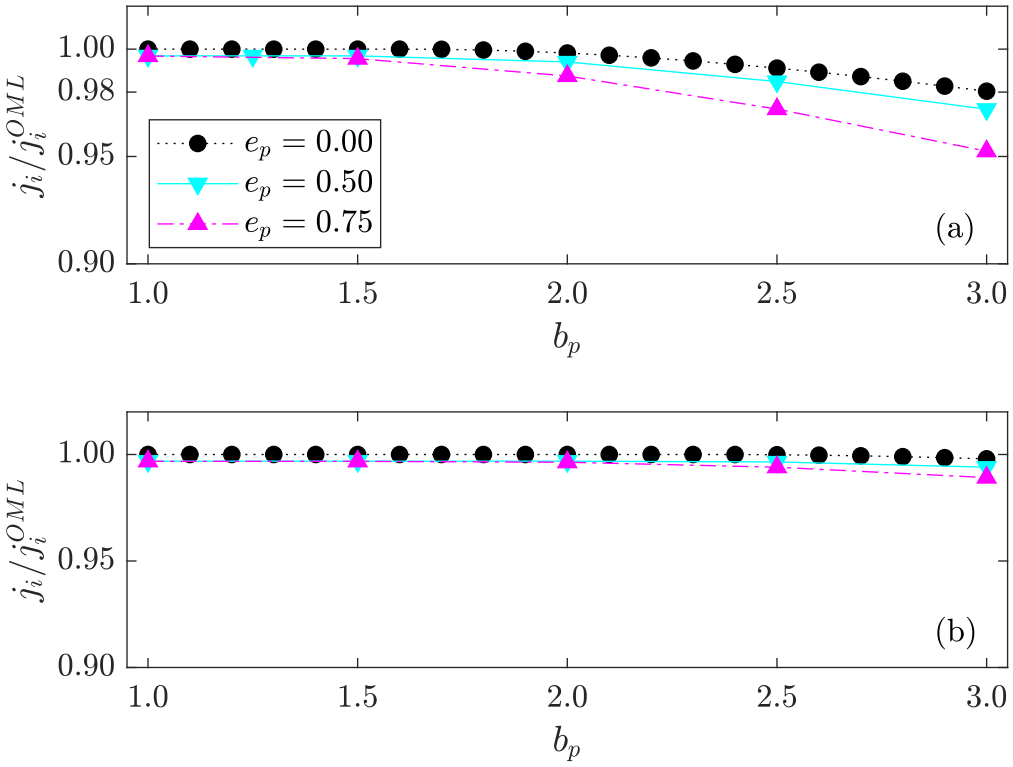

FIGURE 3.19: Collected-to-OML current versus b_p for $e_p = 0$ (black, dotted line with circles), $e_p = 0.5$ (cyan, solid line with down triangles) and $e_p = 0.75$ (magenta, dash-dotted line with up triangles). Panels (a) and (b) corresponds to $\beta = \delta_{em} = 0$ and $\beta = 1.72$ and $\delta_{em} = 0.32$, respectively. The rest of the parameters is given in Eq. (3.9) [129].

Electron emission In addition to the shape and the size of the object, also the emission of electrons at its surface can have an impact on the current collected. A comparison between panel (a) and panel (b) of Fig. 3.19 reveals that, in presence of electron-emission ($\beta = 1.72$), the transition between the OML and non-OML operational regimes occurs at higher b_p for all the three probes considered. Such a result is consistent with previous studies on infinite electron-emitting cylinders [113, 162], and derives from the reduction of the electric field in the proximity of Γ as a consequence of the enhanced density of electrons (see Fig. 3.15). In turn, this translates into a reduction of the number of Γ-originated ions. In addition to being triggered at higher b_p, the drop in the current collection is more gradual than the case where $\beta = 0$, and $j_i/j_i^{OML} \approx 1$ holds approximately for the three eccentricities considered. These results prove that the validity of the OML results extends to a wider range of parameters (eccentricities and sizes) when electrons are emitted at the plasma-material interface. This is a relevant outcome for applications that require modeling the current exchange between an object and the surrounding plasma. Probes for plasma diagnostics, dusty plasmas and space tethers represent pertinent examples.

3.3.2.2 Transition between non-SCL and SCL operational regimes

When electrons are emitted at a negatively biased plasma-material interface, their presence in the region surrounding the object might induce a reversal of the electric field that stems from the formation of a potential well. For fixed values of δ_i, e_p, b_p, and $\phi_p < 0$, this occurs when the emission level (β and δ_{em}) increases beyond a certain threshold. Under such operational condition, the current emitted by the probe is said to be Space Charge Limited (SCL) because a portion of the emitted electrons (namely, the least energetic) are reflected back to Γ due to the action of the reversed electric field. The non-SCL/SCL transition for electron-emitting ellipses was investigated by setting

$$e_p = 0.75, \quad \phi_p = -4, \quad b_p = 1, \quad ,\delta_i = 1, \quad \delta_{em} = 0.32 \quad 0 \leq \beta \leq 30. \tag{3.14}$$

Panel (a) and panel (b) in Fig. 3.20 display the electrostatic potential profile and the fraction of the perimeter of the ellipse under SCL conditions to the total perimeter ($r_{SCL} = p_{SCL}/p$), respectively. For consistency with the results of Sec. 3.3.2.1, the potential is dis-

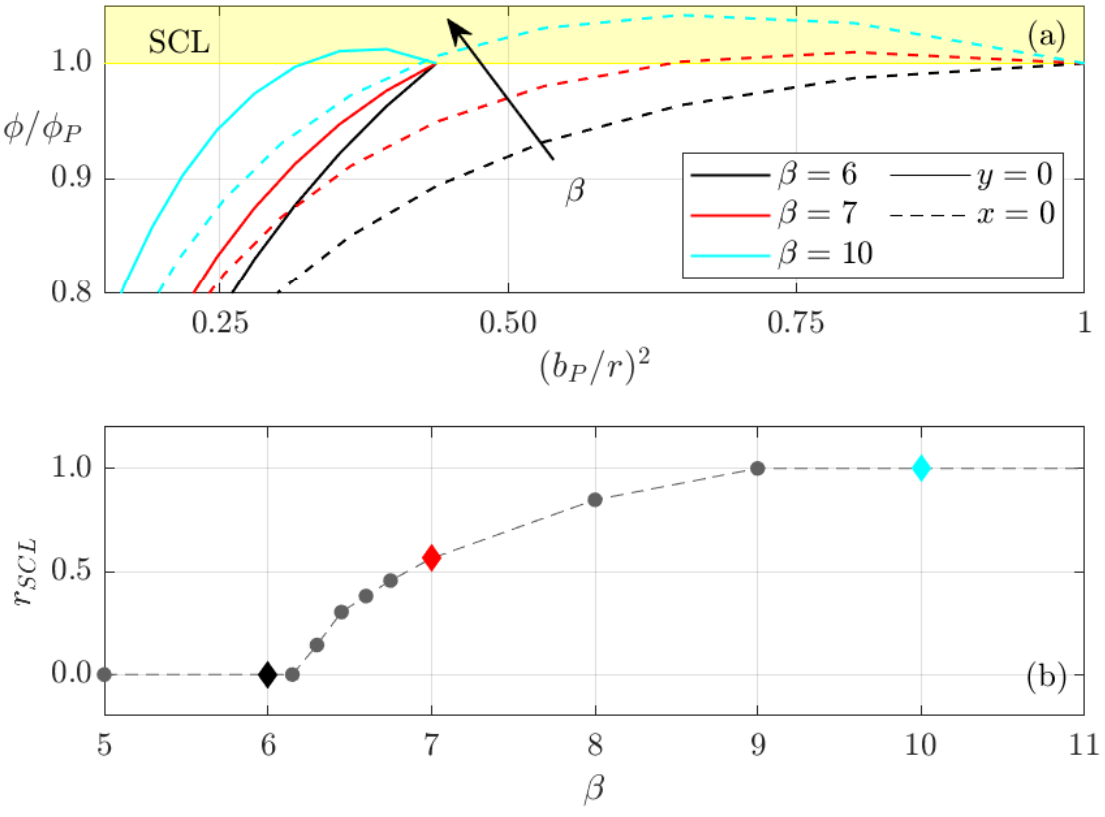

FIGURE 3.20: Panel (a): normalized electrostatic potential profile versus $(b_p/r)^2$ for the set of parameters given in Eq. (3.14) and $\beta = 6$ (black), $\beta = 7$ (red) and $\beta = 10$ (cyan) at $x = 0$ (dashed lines) and $y = 0$ (solid lines). Panel (b): fraction of the perimeter under SCL conditions versus emission level β [129].

played against $(b_p/r)^2$. In the resulting graph, the presence of a potential well in the ϕ/ϕ_p versus r plane (not shown) is identified by a normalized potential profile above the horizontal line $\phi/\phi_p = 1$ [panel (a) in Fig. 3.20]. Markers in panel (b) identify the configurations that were simulated, with the coloured diamonds corresponding to the configurations shown in panel (a).

When the emission is low ($\beta < 6.2$), the electrostatic potential profile is monotonic and no potential dip develops [see black curves in panel (a) of Fig. 3.20]. Accordingly, the electric field point inward everywhere, as observed in the top panels of Fig. 3.21, which shows the normal component of the electric field for various configurations. When $\beta = 6$, all the electrons that are emitted at Γ are driven away from it and their corresponding distribution function, whose maps are provided in Fig. 3.22, is filled with outgoing (i.e., $\varepsilon_n \geq 0$) orbits only [panels (a) and (d)]. As expected, for low values of emission level the probe operates in non-SCL. Nonetheless, from the top-right panel in Fig. 3.21, one observes that at the semi-minor axis ($x = 0$), where the curvature of the ellipse is minimum, the electric field approaches zero, thus suggesting that a potential dip is about to develop in the region surrounding that area.

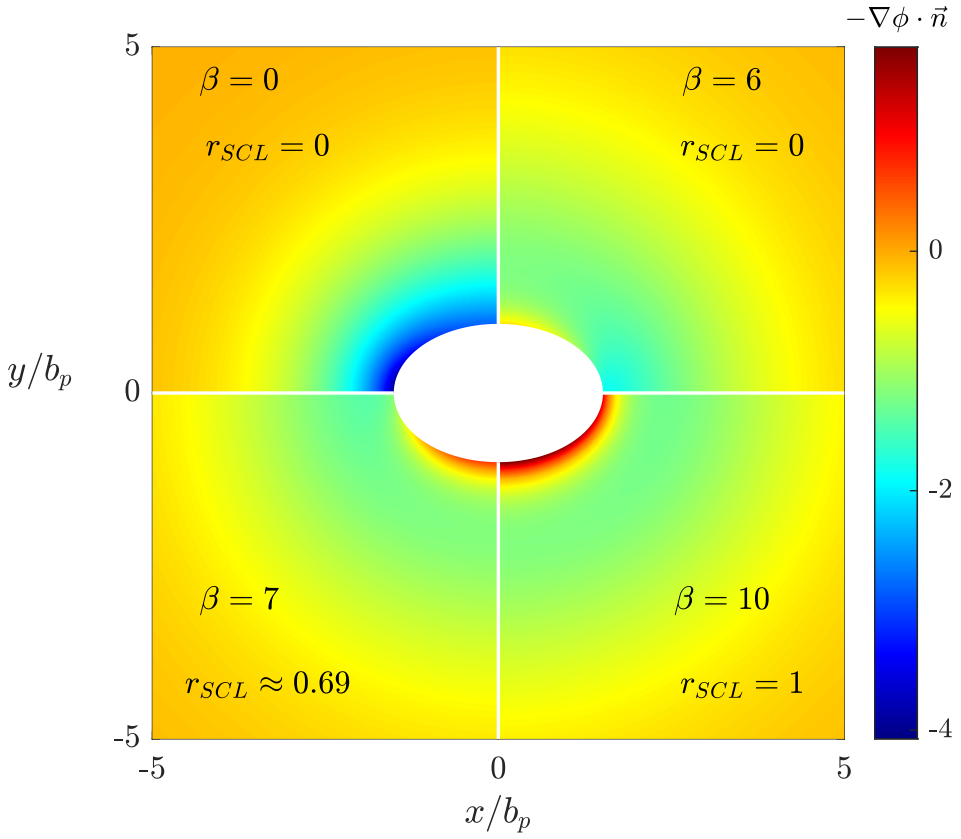

FIGURE 3.21: Normal component of the electric field for for the set of parameters given in Eq. (3.14) [129].

Analysing the interval $6.2 < \beta < 9$, one observes that non-SCL and SCL conditions coexist along the perimeter of the object. While at $x = 0$ the electrostatic potential profile enters the SCL regime (yellow area) for $\beta = 7.00$ (solid and dashed red lines in Fig. 3.20), the potential is still monotonic at the horizontal axis of the computational domain ($y = 0$). In the bottom left panel of Fig. 3.21, one can appreciate the partial reversion of the electric field around the point $(x,y) = (0,b_p)$. Here, emitted electrons fill a portion of the area of incoming particles ($\varepsilon_n < 0$), whereas the same region remains unpopulated at the semi-major axis $(x,y) = (a_p,0)$ [panels (b) and (e) in Fig. 3.22, respectively]. A further increase in the emission level ($\beta > 9$) results in an extension of the potential well to the entire Γ. For $\beta = 10$, the whole probe operates under SCL conditions ($r_{SCL} = 1$) and the electrostatic potential is non-monotonic at both $x = 0$ and $y = 0$ (Fig. 3.20). In addition to growing in the azimuthal direction, the potential dip grows in magnitude and penetrates a bigger region of the sheath (bottom right panel of Fig. 3.21). Accordingly, electrons with higher energies are reflected back to Γ, and the populated areas of incoming particles in panels (c) and (f) of Fig. 3.22 are larger as compared to the previous case.

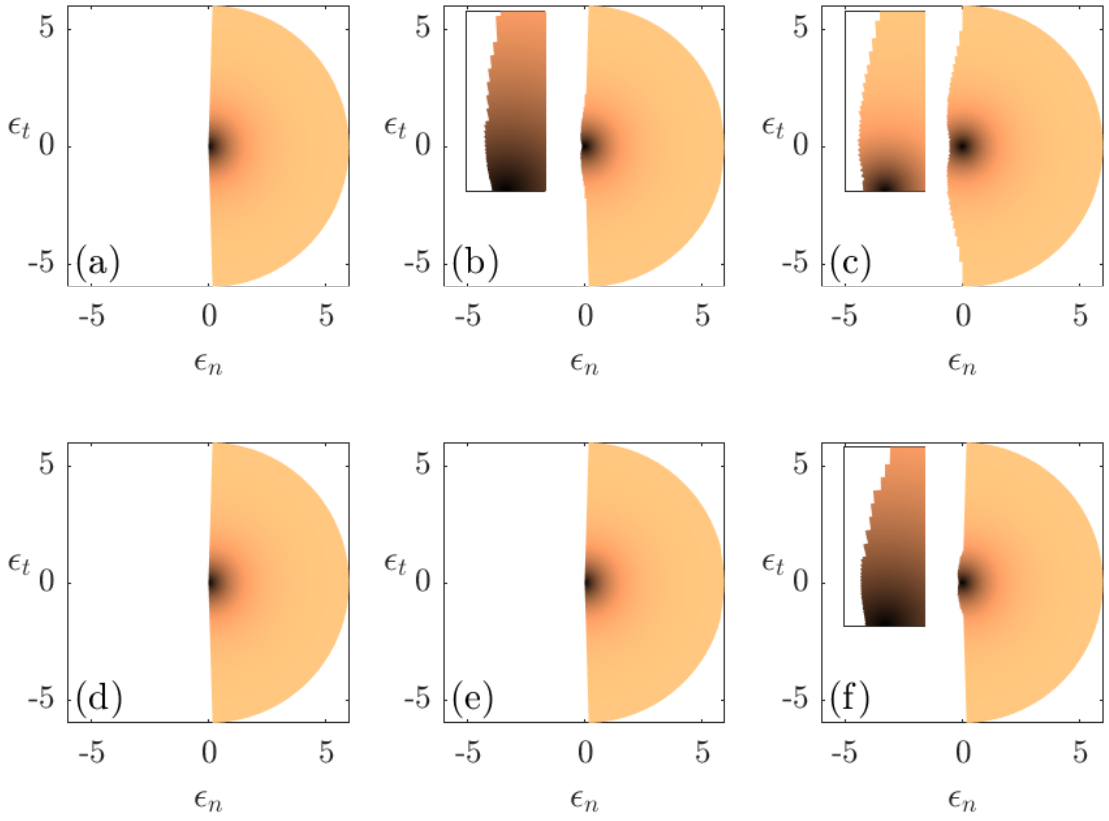

FIGURE 3.22: Normalized distribution functions for emitted electrons (f_{em}) at $(x,y) = (0,b_p)$ [panels (a), (b) and (c)] and $(x,y) = (a_p = 0)$ [panels (d), (e) and (f)] for $\beta = 6$ [panels (a) and (d)], $\beta = 7$ [panels (b) and (e)] and $\beta = 10$ [panels (c) and (f)], respectively. Rest of parameters given in Eq. (3.14) [129].

Operating under SCL conditions is not ideal for the performances of devices such as LWTs. In order to quantify the reduction in the capability of emitting electrons, Fig. 3.23 shows the variation of j_{em}/j_{em0} for a wide range of emission levels, with

$$j_{em0} = -2\beta\sqrt{\delta_{em}} \tag{3.15}$$

the current emitted by a half-Maxwellian (i.e., the current emitted under non-SCL conditions). Each colour identifies the results obtained for a specific geometry, while markers highlight the configurations that were simulated.

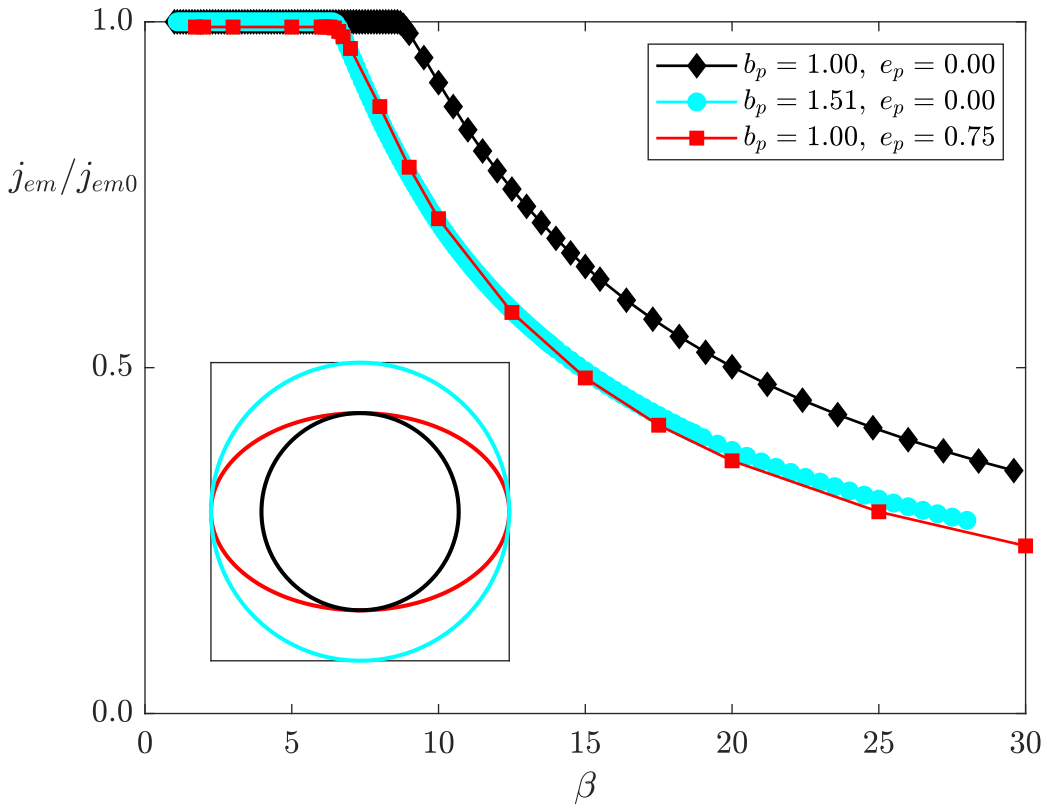

FIGURE 3.23: Emitted-to-half-Maxwellian current versus emission level β for the different probes shown in the inset. Rest of parameters given in Eq. (3.14). Markers identify the configurations that were simulated [129].

The analysis compares the performances of the three different probes shown in the inset: i) an elliptical probe with eccentricity $e_p = 0.75$ and semi-minor axis $b_p = 1$ (solid red curve with squares), and two cylindrical probes with radius equal to the semi-minor (solid black curve with diamonds) and semi-major (solid cyan curve with bullets) axes of the ellipses. For convenience, results regarding cylindrical probes were computed with the solver of Ref. [113]. When the electron emission is low, the simulations gave $j_{em}/j_{em0} = 1$ for the three configurations. An increase in β causes each body to enter the SCL regime, resulting in a reduction of the emitted current. Similarly to the OML/non-OML transition

discussed in Sec. 3.3.2.1, the SCL regime does not occur for the same value of β for all the objects. In particular, the probe with lowest radius is the one that enters the SCL regime for the largest value of β.

Regarding the ellipse and the cylinder of highest radius, the transition occurs for $\beta \approx 6.5$ in both cases, and the two curves follow a similar trend. Despite gradually developing along Γ as discussed previously, the potential well that appears at the point of minimum curvature for the probe with $e_p = 0.75$ has a similar impact to the one that cover the whole probe for $e_p = 0$ and $b_p = 1.51$. Unlike the relatively weak influence of b_p on j_i/j_i^{OML}, the ratio j_{em}/j_{em0} happens to be much more sensitive to the variation in β. For all the three cases, the current emitted drops considerably, reaching values of about 50% for $\beta \approx 15$ in the two worst scenarios. The outcomes of the analysis show that, when moderate biases are considered, there is a good agreement between the current emitted by an ellipses and the one from a cylinder with radius equal to the semi-major axis. Upon using appropriate dimensionless variables, the results for electron-emitting cylinders can thus be used to predict the current emitted by ellipses. This is an important result because, by using an equivalent radius, the broad database that was constructed in [162] for electron-emitting cylinders can be used to estimate the emitted current by ellipses without running additional simulations.

Chapter 4

Non-Stationary Vlasov-Poisson solver

The present chapter describes a novel (backward) semi-Lagrangian solver that was developed as an extension of FONKS-G for the purpose of investigating the plasma sheath around (electron-emitting) two-dimensional bodies in non-stationary scenarios. Extension to time-varying conditions is necessary in order to properly assess the population of trapped particles that, in a collisionless plasma, arise during the transient response of a plasma sheath to a perturbation [166, 170–172]. As discussed in Sec. 3.2.2.1, trapped particles are a fundamental part of the solution for probes facing flowing plasmas.

Since FONKS-G was used as a starting point for the development of this second software, the discussion leaves asides the aspects that the two codes share, and focuses the differences among them. In particular, both the new normalistion and the novel interpolation algorithm, which is at the core of the semi-Lagrangian method, will be discussed in detail. An overview of a first analysis assessing the role of the trapped population is also present.

4.1 Collisionless plasma model in non-stationary conditions

While all the hypotheses introduced in Sec. 2.1 still hold, the novel model relaxes the requirement about the stationary state of the plasma sheath that was at the basis of the stationary solver presented in Sec. 2.2. In these non-stationary conditions, the sheath obeys the set of Eqs. (2.10)-(2.11)-(2.12)-(2.13) that is solved together with the appropriate boundary conditions. The extension to non-stationary scenarios requires introducing a new normalisation, which reads

$$\begin{aligned} &\frac{\boldsymbol{r}}{\lambda_{De}} \rightarrow \boldsymbol{r}, \quad \frac{\boldsymbol{v}}{\sqrt{2}v_{the}} \rightarrow \boldsymbol{v}, \quad \frac{n_{e,i}}{n_0} \rightarrow n_{e,i}, \quad \frac{n_{em}}{n_{em0}} \rightarrow n_{em}, \\ &\sqrt{2}\omega_{pe}t \rightarrow \tau, \quad \frac{2k_B T_\alpha f_\alpha}{m_\alpha n_{\alpha 0}} \rightarrow f_\alpha(\boldsymbol{r},\boldsymbol{v}), \quad \frac{e\phi}{k_B T_e} \rightarrow \phi(\boldsymbol{r}), \end{aligned} \tag{4.1}$$

where $\omega_{pe} \equiv \lambda_{De}/v_{the}$ is the electron plasma frequency. Substituting the above magnitudes in the Vlasov-Poisson system of equations yields

$$\frac{\partial f_\alpha}{\partial \tau} + \boldsymbol{v}_\alpha \cdot \nabla_{\boldsymbol{r}} f_\alpha - \frac{q_\alpha}{2\mu_\alpha} \nabla\phi \cdot \nabla_{\boldsymbol{v}} f_\alpha = 0, \tag{4.2a}$$

$$\Delta\phi = -\rho \equiv n_e + \beta n_{em} - e_i n_i. \tag{4.2b}$$

While the normalized Poisson equation is the same as the one found previously [see Eq. (2.19b)], the non-stationary Vlasov equation now involves the mass ratio μ_α, which entered only in the definition of the current in the stationary case [see Eq. (2.48)]. Contrary to the stationary case, the time appears explicitly in the Vlasov equation and the self-consistent evolution of the sheath depends on the the relative speed of the different species and, in turn, on their relative mass. Therefore, $\mu_\alpha \equiv m_\alpha/m_e$ adds to the set of dimensionless parameters of Eq. (2.20) that, together with the geometry and the bias of the object ϕ_p, identify the configuration of interest. Regarding the boundary conditions, the new normalisation introduced above gives

$$\begin{gathered}
\phi(\tau,\Gamma) = \phi_P, \quad \phi(\tau, r\to\infty) \to 0 \\
f_{em}(\tau,\Gamma,\boldsymbol{v}\cdot\boldsymbol{u}_n > 0) = f_{HM} \equiv \frac{2}{\pi}\exp\{-\mu_\alpha(\boldsymbol{v}\cdot\boldsymbol{v})\}, \quad f_{em}(\tau, r\to\infty, \boldsymbol{v}) = 0 \\
f_{e,i}(\tau,\Gamma,\boldsymbol{v}\cdot\boldsymbol{u}_n > 0) = 0, \quad f_{e,i}(\tau, r\to\infty, \boldsymbol{v}) \to f_M \equiv \frac{1}{\pi}\exp\{-\mu_\alpha(\boldsymbol{v}\cdot\boldsymbol{v})\},
\end{gathered} \tag{4.3}$$

where it was highlighted how the macroscopic magnitudes depend on the non-dimensional time τ in a non-stationary setting.

In order to find a solution to the non-stationary Vlasov-Poisson system just discussed, a novel *semi-Lagrangian* software was implemented as an extension to FONKS-G. Widely applied in problems described by the Vlasov-Poisson system [173–176], semi-Lagrangian schemes rely on the hypothesis of collisionless plasma, which must hold for the Liouville theorem to be valid. After sampling it onto an Eulerian grid in phase space, the distribution function is advanced in time along the characteristics of the Vlasov equation. It is convenient to recall that, for a collisionless plasma, f_α is conserved along such characteristics, which coincide with the orbits of the charged particles (see Sec. 2.2.3). If the latter are followed *forwardly*, the new values of the distribution function at the nodes of the grid are found through a scatter operation from the arriving point of the characteristics. For *backward* semi-Lagrangian schemes, the value of the distribution function is updated through interpolation at the origin of the characteristics from the known values of f_α at the previous time step.

Here, the latter approach is adopted as explained in detail in the next section. Regarding the Poisson solver, which is the other main block of the algorithm, it remains the same as that presented in Sec. 2.2.2. Starting from an initial condition $f_\alpha(0,\boldsymbol{r},\boldsymbol{v}) = f_0$, the structure of the sheath is updated self-consistently at each time step. Likewise the stationary software presented in Sec. 2.2, *FORTRAN* was selected as the coding language.

4.2 Semi-Lagrangian Vlasov-Poisson solver

The Vlasov solver advances in time the distribution function and, at each time step, it computes the charge density profile that is passed as input to the Poisson solver. A backward semi-Lagrangian approach is implemented to update the value of f_α at the nodes of the discrete phase space. Similarly to the stationary case, this requires the numerical integration of the characteristics of the Vlasov equation, which read

$$\frac{d\boldsymbol{r}}{d\tau} = \boldsymbol{v}_\alpha \tag{4.4a}$$

$$\frac{d\boldsymbol{v}_\alpha}{d\tau} = -\frac{e_\alpha}{2\mu_\alpha}\nabla\phi. \tag{4.4b}$$

Multiplying scalarly Eq. (4.4) by the velocity $\boldsymbol{v}_\alpha$, one obtains the equation of the energy

$$\frac{d\varepsilon_\alpha}{d\tau} = e_\alpha \frac{\partial\phi}{\partial\tau}, \tag{4.5}$$

which shows that the total energy

$$\varepsilon_\alpha \equiv \mu_\alpha \boldsymbol{v}\cdot\boldsymbol{v} + e_\alpha[\phi(\boldsymbol{r}) - H_\alpha\phi_p], \quad (H_{e,i}=0, H_{em}=1). \tag{4.6}$$

is conserved along the characteristics only if the electrostatic potential profile does not depend on time. Since this is not the case for the non-stationary scenarios here considered, the code applies the change of variables $(\boldsymbol{v}) \to (\kappa_\alpha, \zeta)$, with $\kappa_\alpha \equiv \mu_\alpha \boldsymbol{v}\cdot\boldsymbol{v}$ the dimensionless kinetic energy and ζ the angle in velocity space defined in Eq. (2.40), and discretises the distribution function in the 4-dimensional space $(x, y, \kappa_\alpha, \zeta)$.

For each node in the physical space, the code discretises with a $N_\kappa \times N_\zeta$ grid the region in the velocity space delimited by

$$(\kappa_\alpha, \zeta) \in [0,\ \kappa_\alpha^{\max}] \times [0,\ 2\pi]. \tag{4.7}$$

with κ_α^{max} a numerical parameter selected high enough to cover an appropriate range of velocities in order to include the relevant part of the distribution. The semi-Lagrangian solver keeps the $\kappa_\alpha - \zeta$ grid fixed. Since there is a transient and the energy of the particles changes according to Eq. (4.5), particles with a positive energy at a certain insant in time can be trapped with a negative energy afterwards due to the change in the profile of the electrostatic potential. This a collisionless trapping mechanism described in Ref. [170].

The nodes of the discrete phase-space are denoted as $\boldsymbol{z}_s = [\boldsymbol{r}^i, \kappa_\alpha^k, \zeta^l]$, with $i = 1, \ldots, N$, $k = 1, \ldots, N_\kappa$ and $l = 1, \ldots, N_\zeta$, while the boundary conditions for the distribution function

become

$$f_{e,i}(\tau,\Gamma,\kappa_{e,i},-\frac{\pi}{2}<\zeta<\frac{\pi}{2})=0,\quad f_{e,i}(\tau,\Gamma_{max},\kappa_{e,i},\zeta)=\frac{\exp(-\varepsilon_{e,i})}{\pi} \tag{4.8a}$$

$$f_{em}(\tau,\Gamma,\kappa_{em},-\frac{\pi}{2}<\zeta<\frac{\pi}{2})=\frac{2\exp(-\varepsilon_{em})}{\pi},\quad f_{em}(\tau,\Gamma_{max},\kappa_{em},\zeta)=0. \tag{4.8b}$$

with the dependence on κ_α implicit in the value of the total energy ε_α. Once the grid in the energy-ζ (velocity) space is defined and an initial condition f_0 assigned, the distribution function is advanced in time as follows.

At $\tau=\tau_0$, the distribution function is known at all the nodes $\boldsymbol{z}_s$ of the discrete phase space. To compute the value of the distribution function at node $\boldsymbol{z}_{s0}$ at time $\tau_0+\Delta\tau$, with $\Delta\tau$ a (small) time step, one integrates Eqs. (4.4a)-(4.4b) backward in time with initial condition $\boldsymbol{z}_{s0}$. The final point of the orbit $\boldsymbol{z}_{sf}$ identifies the root (origin) of the characteristics passing through $(\boldsymbol{z}_{s0})$ at time $\tau_0+\Delta\tau$. During the backward integration step, if an orbit crosses one of the boundaries of the computational domain, the unknown value of the distribution function $f_\alpha(\tau_0+\Delta\tau,\boldsymbol{z}_{s0})$ is assigned according to the BCs in Eqs. (4.8a)-(4.8b). However, when the root of the characteristic lies inside the computational domain, the value of the distribution function there is computed by interpolating the distribution function at the previous time step [i.e., $f_\alpha(\tau_0,\boldsymbol{z}_s)$].

Table 4.1 summarises the different type of orbits together together with the value of the distribution function that they yield, while Fig. 4.1 provides a sketch of the backward semi-Lagrangian approach described above. The black filled circle represents the node at

Types of orbits (non-stationary)

Stop condition	Label	Distribution function
$\boldsymbol{r}_{sf}\in\Gamma$	Γ-originated	$f_{e,i}(\tau_0+\Delta\tau,\boldsymbol{z}_{s0})=0$ $f_{em}(\tau_0+\Delta\tau,\boldsymbol{z}_{s0})=f_{HM}$
$\boldsymbol{r}_{sf}\in\Gamma_{max}$	Γ_{max}-originated	$f_{e,i}(\tau_0+\Delta\tau,\boldsymbol{z}_{s0})=f_M$ $f_{em}(\tau_0+\Delta\tau,\boldsymbol{z}_{s0})=0$
$\boldsymbol{r}_{sf}\notin\Gamma,\Gamma_{max}$	Trapped	$f_\alpha(\tau_0+\Delta\tau,\boldsymbol{z}_{s0})=f_\alpha(\tau_0,\boldsymbol{z}_{sf})$ $f_\alpha(\tau_0,\boldsymbol{z}_{sf})$ interpolated from $f_\alpha(\tau_0,\boldsymbol{z}_s)$

TABLE 4.1: Classification of orbits (non-stationary case)

which the distribution function is unknown, which coincide with the initial condition for the numerical integration. The resulting orbit (dashed black curve) ends up at the red filled circle, which identifies the origin of the characteristic passing through $(\tau_0+\Delta\tau,\boldsymbol{x}_{s0})$. After determining the cell that contains it, the value of the distribution function at $(\tau_0,\boldsymbol{r}_f,\mathbf{v_f})$ is found through an interpolation procedure. In the current version of the code, the latter is carried out with the *cloud-in-cell* (CIC) approach described in Appendix F. Since it is a local method, the CIC interpolation uses only the information from the vertices (red empty circles) of the cell that contains the root of the characteristics $(\boldsymbol{r}_f,\mathbf{v_f})$.

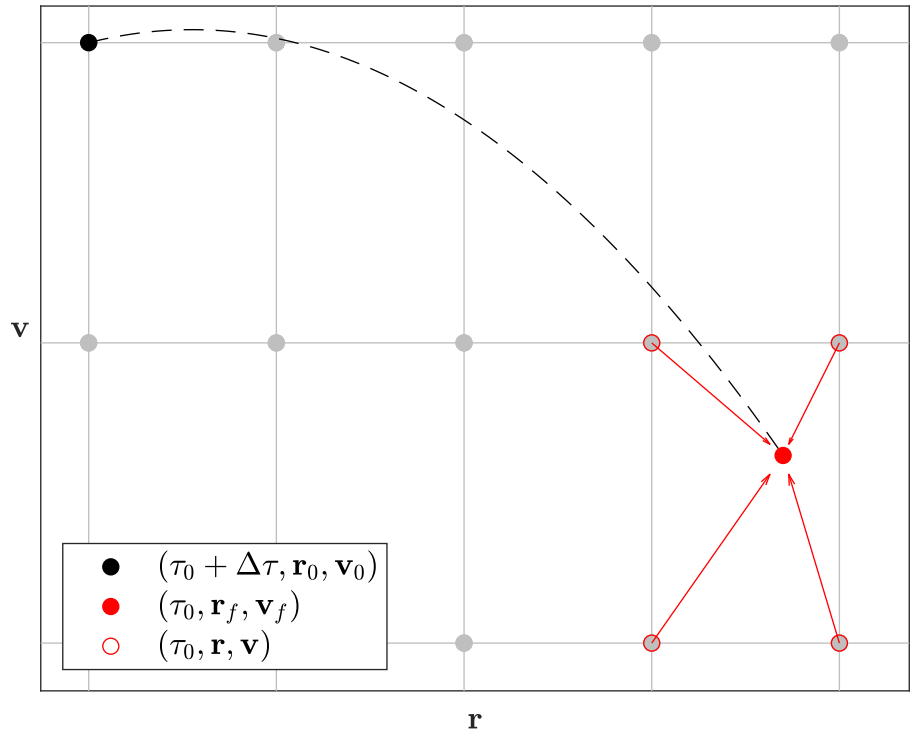

FIGURE 4.1: Sketch of the backward semi-Lagrangian Vlasov solver using the CIC interpolation method.

Once the value of the distribution function is known at time $\tau 0$, the densities at the nodes of the computational domain are obtained from

$$n_\alpha(\tau_0, \boldsymbol{r}) \approx \frac{1}{2\mu_\alpha} \int_0^{\kappa_\alpha^{max}} \int_0^{2\pi} f_\alpha(\tau_0, \boldsymbol{r}, \kappa_\alpha, \zeta) d\kappa_\alpha d\zeta, \tag{4.9}$$

where $1/(2\mu_\alpha)$ represents the Jacobian of the $(\boldsymbol{v}) \rightarrow (\kappa_\alpha, \zeta)$ transformation. The new space charge density is then passed to update the electrostatic potential profile that is used in the next iteration of the Vlasov solver. In order to monitor whether the latter system reaches a steady-state, the code keep records at each time step of some scalar quantities such as the total density inside the computational domain ρ_{scl} and the charge and current densities of the various species at the object boundary Γ.

4.3 Particle trapping analysis

This section presents the results of a first analysis assessing the impact of the population of trapped particles on the structure of the sheath around electron-emitting two-dimensional

objects. A comparison between the results of FONKS-C, CPIC and the semi-Lagrangian Vlasov-Poisson (SLVP) solver introduced above is presented.

4.3.1 Effect of particle trapping on the structure of the sheath

This section presents a comparison between the different solvers. Since it assumes stationary conditions (i.e., $\partial f_\alpha/\partial\tau = 0$), FONKS-C cannot compute self-consistently the population of trapped particles. Their distribution function is set to zero. On the contrary, the novel SLVP and CPIC can assess the role of the trapped population that arises during the transient. Therefore, comparing the results of the different solvers provides an insight of the impact of the trapped population on the macroscopic magnitudes of the sheath. In addition, it allows to verify the correct implementation of the novel semi-Lagrangian solver. An sensitivity analysis varying the space resolution in the radial dimension (i.e., N_r) is also carried out in order to identify a good set of numerical parameters for the novel semi-Lagrangian solver.

Figure 4.2 compares the plasma sheath in a simulation with the set of physical parameters

$$b_p = 1,\ \delta_i = 1,\ \mu_i = 1,\ \phi_p = -10,\ \delta_{em} = 0,\ \beta = 0, \tag{4.10}$$

computed with FONKS-C (solid green), CPIC (dashed magenta) and SLVP (dash-dotted black). For the non-stationary solvers, a Maxwellian plasma was considered as initial condition (i.e., $f_0 = f_M$). Overall, the SLVP results are free-of-numerical noise and smooth,

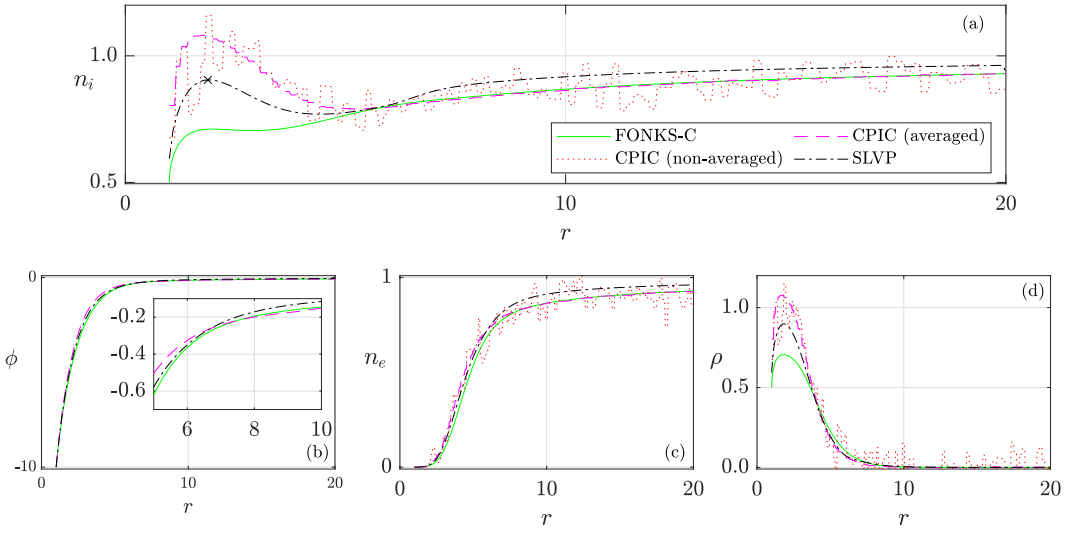

FIGURE 4.2: Plasma sheath computed with FONKS-C (solid green), CPIC and SLVP (dash-dotted balck) for the set of parameters in Eq. (4.10). CPIC results are shown before (red dotted) and after (dashed magenta) averaging in time.

as opposed to the results obtained with CPIC. For the latter, a proper average in time is

necessary to remove the statistical noise induced by the macro-particle description (highlighted by the red dotted curve). Panel (a) shows that the n_i profiles obtained with the non-stationary solvers all display a region close to the probe boundary where the density of the ions is significantly higher than that obtained with the stationary solver. Such enhancement, which is analogous to that shown in Fig. 5 of Ref. [166], is a footprint of the particle trapping, whose magnitude changes between the two different solvers. While the CPIC profile overcomes the background plasma density value, the solution obtained with the SLVP solver does not reach as high a peak. Such discrepancy between the two local maxima, in the order of 18%, is likely due to the different evolution in time of the potential profile, which affects the amount of particles that get trapped inside the plasma sheath (see also discussion in Sec. 4.3.2).

The bigger population of plasma ions given by CPIC reflects in the electrostatic potential profile, displayed in panel (b). While overall the solvers provides results that are in good agreement among each other, a more detailed look show that the profiles slightly differ from one another. In the region close to the probe, the SLVP is below the one of CPIC, which is less negative in view of the bigger population of plasma ions. At $r \approx 7$ the curves cross (see inset) and, far away from the probe, the SLVP electrostatic potential is above both the other two curves. Therefore, the SLVP slightly overestimates the density of the plasma species far away from the probe [see panels (a) and (c)], though such differences do not affect the extension of the sheath. In fact, the space charge density profiles in panel (d) show that quasi-neutrality is recovered in all cases around $r \approx 10$.

In order to understand the source of the enhancement of the density of attracted species in the region near the probe, Fig. 4.3 shows the results of a detailed analysis of the ions distribution function. The three panels show a comparison between the distribution function in the velocity space obtained with SLVP (top half) and FONKS-C (bottom half) at the probe boundary (left panel), the point where the maximum difference with respect to the stationary solver occurs (middle panel), and a point close to the plasma boundary (right panel). At the probe boundary (left), the maps are populated with incoming ($v \cdot \cos\zeta < 0$) particles only since no ions are emitted from the probe. In the case of FONKS-C (bottom half), the peak of the distribution function is well defined and a net separation exists between the areas where the distribution function has null and finite positive values. On the contrary, the peak of the distribution function does not emerge as clearly in the case of SLVP (top half) and part of the area that is unpopulated in the stationary solver is filled. The distribution function gradually diminishes to zero from its maximum, which is also appears smaller than the corresponding one for the stationary solver.

This is even more evident in the middle panel, which corresponds to the point where the peak of the ions density occurs. The area inside the potential barrier that is populated in the non-stationary case is bigger than at the probe boundary, especially for velocity angles that are close to $\zeta = \pi/2$, while it shrinks as ζ approaches π. Far away from the probe (right panel), the distribution function resembles a Maxwellian with a small empty *cone* in the $v \cdot \cos\zeta > 0$ region. Such cone is due to the presence of the probe [166] and is present in both plots, though in the stationary case is much narrower than in the non-stationary one and it cannot be appreciated as clearly. Again, the region inside the potential barrier

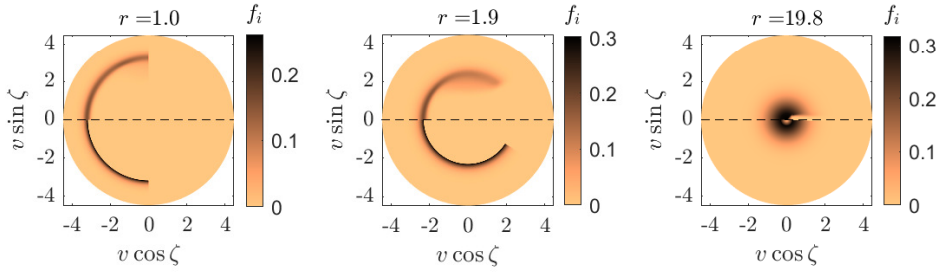

FIGURE 4.3: Plasma ions distribution function maps in the velocity space computed with FONKS-C (bottom half) and SLVP (top half) for the set of parameters in Eq. (4.10). Left, middle and right panel correspond to $r = 1$ (i.e., probe boundary), $r = 1.9$ and $r = 19.8$.

that is empty in the case of FONKS-C (bottom) is populated in the case of SLVP (top). Though small, the contribution of this population to the distribution function explains why the SLVP density is higher than FONKS-C one far away from the probe [see panel (a) in Fig. 4.2].

The above discussion shows that the enhanced ions density is due to particles with negative (at steady-state) energy that gets trapped inside the sheath during the transient phase. This appears more clearly in Fig. 4.4, which displays the distribution function at the probe boundary (left panel in Fig. 4.3) versus the kinetic energy for different angles in the velocity space. Results of the SLVP are shown for $N_r = 120$ (dashed orange) and $N_r = 240$ (dash-dotted black) in order to highlight the effect of the spatial resolution on the numerical results. Contrary to the stationary solver, the distribution function obtained with the SLVP does not feature a discontinuity in the energy-direction. Overall, the SLVP curves spread over a wide range of energies and its maximum is considerably lower than that of the stationary solver, especially at $\zeta = 90°$. As ζ approaches 180°, the distribution functions obtained with SLVP shrink and their maximum increase, but never reach the value of FONKS-C. When the spatial resolution is low (i.e., $Nr = 120$), the distribution function spreads over a wider range of energies and its maximum is considerably smaller than that of the stationary solver. The distribution obtained with $N_r = 240$ nodes along r has lower tails and is closer to the FONKS-C one.

These results suggest that, due to the fact that a low order (linear) interpolation scheme is used, a high number of node in the radial dimension is needed in order to capture correctly the gradients of the distribution. In order to see whether a higher order interpolation scheme could be useful in this regard, a cubic B-spline interpolation method was tested by implementing the library of Ref. [177]. Unlike the CIC interpolation method, the cubic B-spine does not conserve the distribution function by construction and particular measures

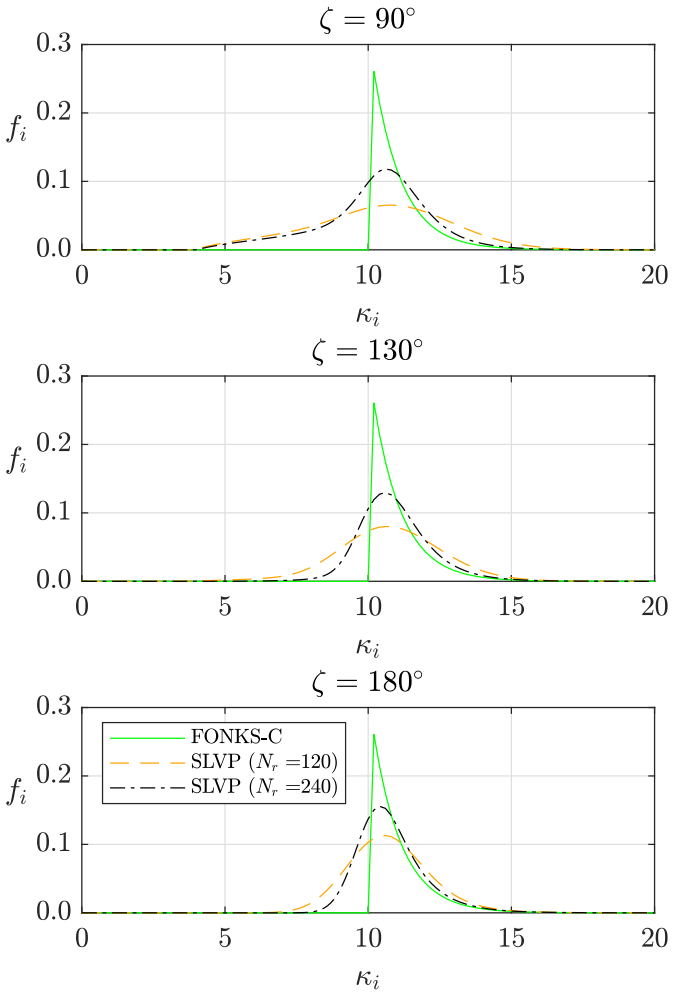

FIGURE 4.4: Ions distribution function versus kinetic energy computed at the probe boundary for the set of parameters in Eq. (4.10). Top, middle and bottom panels correspond to $\zeta = 90°$, $\zeta = 130°$ and $\zeta = 180°$, respectively. Results are shown for FONKS-C (solid green) and SLVP with $N_r = 120$ (dashed orange) and $N_r = 240$ (dash dotted black).

must be taken to avoid negative values of the distribution function. Therefore, a simple filter that assigns a null value to the function when this reaches negative values was implemented. However, this introduced several discontinuities along the energy direction, which prevented the code from reaching a numerical convergence. It was thus decided to use the low order interpolation method. Since a further increase in the spatial resolution did not bring significant changes, the SLVP results shown in Fig. 4.2 are consistent with $N_r = 240$.

To complete the comparison between the different solvers, it is interesting to compare the values of the current at the plasma-probe interface, which are listed in Table 4.2. For

both non-stationary solver, the ions current is bigger than its stationary counterpart. In the case of CPIC, the increment is contained and could be traced back to a numerical error. On the contrary, the SLVP solver predicts a current sensibly higher ($\approx 13\%$) than that of the stationary solver. The increase in the ions current is comparable to that observed for the ions density and is consistent with what discussed about the distribution function. An even bigger discrepancy is observed for the electron current, though in absolute value its magnitude is negligible. Overall, the results of SLVP are expected and are in good agreement with previous works regarding current collection by probe in non-stationary scenarios [166]. Therefore, it can be stated that the solver is well-implemented.

Solver	$I_e\,[\mathrm{A/m}]$	$I_i\,[\mathrm{A/m}]$
FONKS-C	2.71×10^{-9}	2.23×10^{-4}
SLVP	3.44×10^{-9}	2.54×10^{-4}
CPIC ($f_0 = f_M$)	2.69×10^{-9}	2.28×10^{-4}

TABLE 4.2: Magnitude of the currents of plasma electrons (I_e) and plasma ions (I_i) at the plasma-material interface, obtained with FONKS-C, SLVP and CPIC for the set of parameters in Eq. (4.10).

4.3.2 Effect of the electron emission on particle trapping

This section presents a parametric analysis that quantifies the influence of electron-emission at the plasma-probe interface on the trapped population, and how this affects the macroscopic quantities of the plasma sheath. The first case of the analysis involves a cylindrical probe ($e_p = 0$) and the set of non-dimensional parameters

$$b_p = 1,\ \delta_i = 1,\ \mu_i = 1,\ \phi_p = -10,\ \delta_{em} = 0.32,\ \beta = 10 \tag{4.11}$$

Figure 4.5 displays a comparison between the plasma sheath obtained with FONKS-C (green lines) and that of SLVP initialised with a Maxwellian plasma ($f_0 = f_M$, black lines). Panel (a) shows that the electrostatic potential profiles follow similar trends, though the one obtained with the stationary solver is slightly above that of SLVP. This is consistent with what shown in panel (b), which displays the densities of the various species computed with the two solvers. Similarly to what discussed in the previous section (see Fig. 4.2 and the corresponding discussion), the plasma ions profile given by the non-stationary solver features a region where the population of the species is singificantly higher with resepct to the stationary one. This is particularly evident in the region near the probe, where the largest part of the trapping occurs. Far away from the probe, the SLVP n_i profile is also above FONKS-C one.

Regarding the electron density (dashed lines), there is good agreement among the curves, though again the one obtained with SLVP is slightly below that of the stationary solver. Panel (b) also shows the profile of the emitted electrons. In both cases, the curves follow the expected trend, rapidly decreasing as one moves away from the probe,

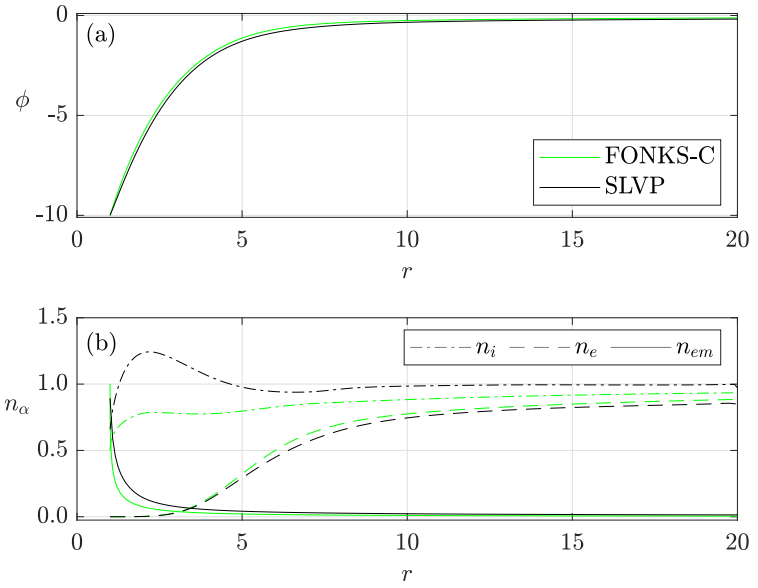

FIGURE 4.5: FONKS-C (green) and SLVP (black) plasma sheath for the set of parameters in Eq. (4.11). Panel (a): electrostatic potential profile; panel (b): densities of plasma ions (dash-dotted), plasma electrons (dashed) and emitted electrons (solid).

though in the case of the semi-Lagrangian solver the steepness of the decay is smoother. This slight difference can be explained by the different numerical resolutions used by the two codes. In fact, FONKS-C allows to define a much finer mesh in the energy-ζ domain than SLVP. Given that the population of emitted electrons is particularly sensitive to the resolution in the ζ-direction, this can explain the difference that arises in the region near the probe.

Nonetheless, the results are useful in understanding the influence of the population of the emitted electrons on the particle trapping. In fact, by comparing the profile of the plasma ions with the corresponding one in Fig. 4.2, the former is significantly higher than the one in absence of emitted electrons. Therefore, in presence of electron emission, the trapped population is enhanced. Accordingly, Table 4.3 highlights that the current of plasma ions is approximately 10% bigger than the one collected when no electrons are emitted at the probe contour Γ (see value in Table 4.2). Regarding the current of emitted electrons, it is interesting to highlight that the value of SLVP is in agreement with that of FONKS-C, which is consistent with the current emitted by a half-Maxwelllian $|j_{em0}/\lambda_{De}| = 2\beta\sqrt{\delta_{em}} = 6.76\times10^{-4}\,\mathrm{A/m}$. This is expected because both solvers predicts that the probe operate under non-SCL conditions.

Since the semi-Lagrangian solver is computationally expensive, the previous results were computed assuming that the mass of the ions is equal to that of the electrons (i.e, $\mu_i = 1$). Although unphysical, the discussion provides an insight about the mechanism of particle trapping and how it affects the plasma sheath around the probe with and without electron emission. In order to verify whether the previous conclusions still hold for a more

β	Solver	$I_e\,[\mathrm{A/m}]$	$I_i\,[\mathrm{A/m}]$	$I_{em}\,[\mathrm{A/m}]$
10	FONKS-C	2.45×10^{-9}	2.23×10^{-6}	6.76×10^{-4}
	SLVP	3.05×10^{-9}	2.80×10^{-4}	6.68×10^{-4}

TABLE 4.3: Magnitude of the currents of plasma electrons (I_e), plasma ions (I_i) and emitted electrons (I_{em}) at the plasma-material interface, obtained with FONKS-C and SLVP for the set of parameters in Eq. (4.11).

realistic case, a parametric analysis was carried out with CPIC to quantify for a cylindrical probe and the set of non-dimensional parameters

$$b_p = 1,\ \delta_i = 1,\ \mu_i = 1836,\ \phi_p = -10,\ \delta_{em} = 0.32,\ \beta = \{0, 10, 30\}. \tag{4.12}$$

Besides verifying whether previous conclusions drawn from the case of $\mu_i = 1$ still hold for a more realistic case considering hydrogen ions ($\mu_i = 1836$), several values of electron emission are considered in order to quantify the influence of the trapped population on the transition between the non-SCL and SCL regime for an emissive cylindrical probe. In addition, the occurrence of multiple solutions for the same values of the parameters is investigated by considering two different initial conditions for CPIC: (i) an empty computational domain, and (ii) a computational domain filled with a Maxwellian plasma. Since the amount of trapped particles depends on the transient phases and the initial conditions, the same set of physical parameter can give different steady solutions in non-stationary simulations.

Figure 4.6 displays a comparison between the solutions obtained with FONKS-C (solid green lines) and those of CPIC starting from an empty domain ($f_0 = 0$, dash-dotted blue line) and a Maxwellian plasma ($f_0 = f_M$, dashed magenta line). When $f_0 = 0$, the population of trapped particles seems to be zero or very small because the density profiles of the ions obtained with CPIC resemble those of the stationary solver. However, when the initial condition is a Maxwellian plasma ($f_0 = f_M$), the n_i profiles display a bump close to the probe boundary. This region of enhanced density is the footprint of the particle trapping, whose magnitude happens to depend on the history of the system. Different initial conditions yield different steady-states. This outcome was also observed in Vlasov-Poisson simulations of the expansion of a collisionless plasma in a magnetic nozzle [151].

Compared to the results shown in Fig. 4.2 (see corresponding discussion in Sec. 4.3.2), one observes that the trapped population is lower for higher values of μ_i. The final amount of trapped particles depends also on the emission level β. The top right ($\beta = 10$) and bottom left ($\beta = 30$) panels of Fig. 4.6 show that the population of trapped particles increases with it. For $\beta = 30$, the ions density close to the probe becomes even greater than the unperturbed plasma density (i.e., $n_i > 1$). In this condition, the current emitted at the plasma-probe interface is SCL due to the presence of a potential well close to the Γ boundary (see inset in the bottom right panel). However, the population of trapped ions makes the potential well less pronounced, thus delaying the onset of the SCL regime and mitigating its effect on current emission. As a result, the emitted current for $\beta = 30$ is

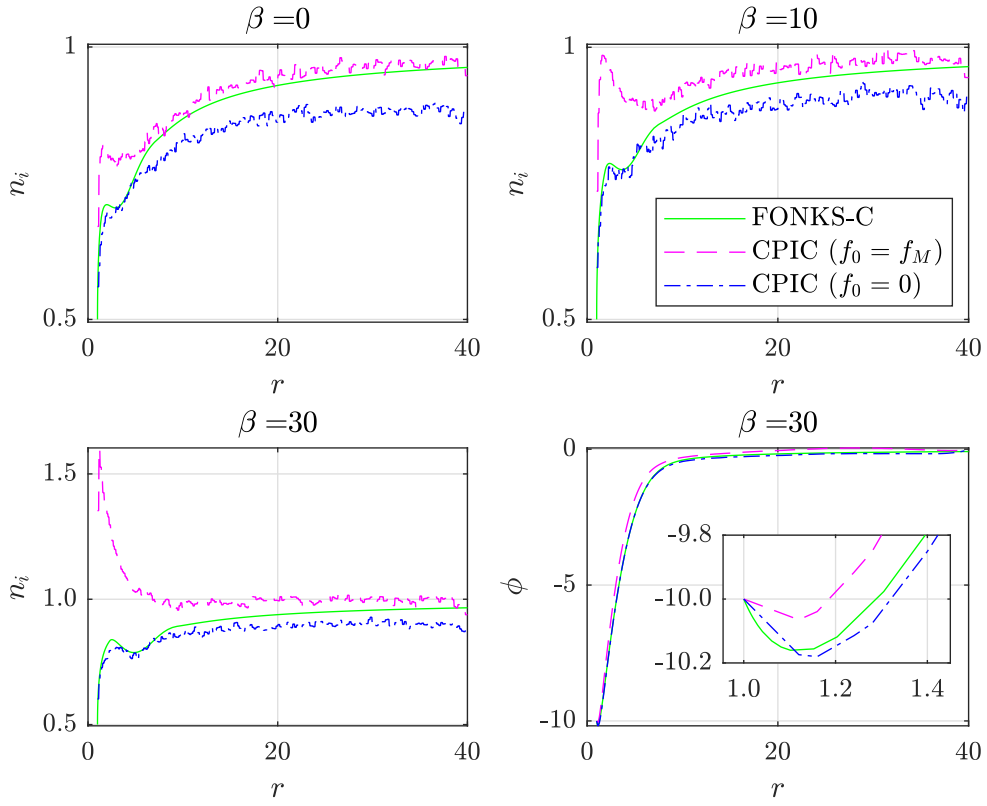

FIGURE 4.6: FONKS-C (solid green) and CPIC results for the set of parameters in Eq. (4.12). CPIC results are shown for $f_0 = 0$ (dash dotted blue) and $f_0 = f_M$ (dashed magenta). Top left, top right and bottom left panels show the ions density for $\beta = 0$, $\beta = 10$ and $\beta = 30$, respectively. Bottom right panel shows the electrostatic potential for $\beta = 30$.

approximately 20% bigger with respect to the case where the trapping is neglected, as shown in Table 4.4.

Disregarding the numerical error that causes the discrepancies between the results of the stationary solver and CPIC started with $f_0 = 0$, it emerges how particle trapping not only enhances the emitted current under the SCL regime (i.e., $\beta = 30$), but also increases the collected current (I_i) under any operational condition. In fact, while CPIC ions current for $f_0 = 0$ is typically smaller than that of FONKS-C, it becomes bigger than the latter when particle trapping occurs (i.e., $f_0 = f_M$). The increase in the collected current is in the order of $7-8\%$, which is aligned with what observed with the SLVP solver for $\mu_i = 1$ (see Table 4.3 and related discussion).

Overall, this is an interesting result for LWTs applications because it suggests that the presence of trapped particles mitigates the SCL effects, thus improving the overall performances of the tether. Quantifying and measuring the population of trapped particles is also convenient in order to improve current models implemented in plasma diagnostics

β	Solver	$I_e\,[\mathrm{A/m}]$	$I_i\,[\mathrm{A/m}]$	$I_{em}\,[\mathrm{A/m}]$
0	FONKS-C	2.71×10^{-9}	5.21×10^{-6}	/
	CPIC ($f_0=0$)	2.51×10^{-9}	4.88×10^{-6}	/
	CPIC ($f_0=f_M$)	2.76×10^{-9}	5.33×10^{-6}	/
10	FONKS-C	2.71×10^{-9}	5.21×10^{-6}	6.76×10^{-4}
	CPIC ($f_0=0$)	3.09×10^{-9}	4.99×10^{-6}	6.68×10^{-4}
	CPIC ($f_0=f_M$)	2.52×10^{-9}	5.35×10^{-6}	6.68×10^{-4}
30	FONKS-C	2.45×10^{-9}	5.21×10^{-6}	1.34×10^{-3}
	CPIC ($f_0=0$)	2.25×10^{-9}	4.94×10^{-6}	1.29×10^{-3}
	CPIC ($f_0=f_M$)	2.71×10^{-9}	5.42×10^{-6}	1.67×10^{-3}

TABLE 4.4: Magnitude of the currents of plasma electrons (I_e), plasma ions (I_i) and emitted electrons (I_{em}) at the plasma-material interface, obtained with FONKS-C and CPIC for the set of parameters in Eq. (4.12).

with emissive probes [112].

Chapter 5

Conclusions and Future work

This final Chapter discusses[1] the main contributions of the present work and provides an overview of the foreseen activities that are being planned in order to continue the analysis started with the present thesis.

5.1 Summary of contributions

Motivated by the need to extend OMT-based models to geometrical configurations that are relevant for LWTs applications, the present work led to the development, from scratch, of two novel Vlasov-Poisson solvers for the investigation of the plasma sheath around two-dimensional electron-emitting objects immersed in an unmagnetised, collisionless, Maxwellian plasmas.

The first software, registered under the name FONKS-G, solves self-consistently the *stationary* Vlasov-Poisson system of equation adopting a kinetic description of all the charged species. Built toward guaranteeing both accuracy and capability to adapt to different geometries, it features different solvers that are coupled together according to the case of interest. Some of its most relevant aspects are:

- *Physical space discretization*: discretisation of the computational domain with both *structured* and *non-structured* meshes. This enhances the versatility of the code, which can address plasma-material interfaces of any two-dimensional geometry.
- *Backward Liouville method*: the distribution function is discretised onto a four-dimensional (2D-2V) Eulerian grid in phase-space and, at each node, its value is inferred from a backward numerical integration of the Vlasov characteristics. This choice guarantees high accuracy of the results, which are free from the statistical noise induced by the macro-particle discretisation implemented in the widely-used PIC method.

[1] Part of the summaries of the main contributions and the future activities is adapted from those provided in Ref. [128, 129].

- *Orbit integrators and electric field reconstruction*: the code includes different numerical integrators for computing the trajectories of the particles. Depending on the strategy adopted for the reconstruction of the electric field along the orbit, the propagators show different conservation properties. In particular, an energy-conserving hybrid Crank-Nicolson scheme was adapted from PIC applications in order to guarantee the conservation of the energy.

- *Parallelisation strategy*: the tasks of the Vlasov solver, which is the most demanding part of the algorithm from a computational standpoint, are distributed among an arbitrary number of processors. The current strategy involves assigning to each process an (almost) equal set of nodes in the physical space. After defining a discrete domain in the velocity space, the processes computes the distribution function there according to the backward Liouville method discussed above.

An extensive verification campaign was carried out against numerical results obtained with FONKS-C and CPIC. The former is an Eulerian Vlasov-Poisson solver developed at UC3M and used for simulating emissive probes with cylindrical cross-section. The second is a PIC code developed at Los Alamos National Laboratory for the modelling of plasma-material interaction in curvilinear configurations. A good agreement was found between the results obtained with different solvers of FONKS-G and those generated with the above tools for both cylindrical and elliptical geometries. This provided a solid proof of the correct implementation of the novel algorithm. Compared to the PIC algorithm, FONKS-G captures interesting features of the sheath, such as the potential well in presence of SCL emission, even if a lower resolution in physical space is used. In addition, its results are free of the statistical noise.

5.1.1 Limitations of stationary Vlasov-Poisson solvers

A first simulation campaign allowed to investigate some limitations that are intrinsic to stationary Vlasov solvers based on backward Liouville methods. This section summarises its findings, which helped identifying a set of good practices for the development of such solvers.

First, a detailed analysis of the dynamics of the charges attracted by a cylindrical probe revealed that conservation laws of physical invariants (energy and angular momentum) cannot be recovered unless specifically designed algorithms are implemented. The long-living trapped particles are the most affected population. Rather than the orbital propagator, the major culprit for the above inaccuracies turned out to be the algorithm in charge of computing the electric field along the orbits from the values of the electrostatic potential at the grid points. A structured mesh proved to work better with respect to an unstructured one. Also, energy-conserving algorithms are necessary for a highly detailed and accurate analysis of the kinetic features. The Crank-Nicolson scheme implemented in this work represents a valuable example.

A second step involved studying the trajectories of particles trapped in sheath around an elliptic probe. This revealed the presence of chaotic dynamics that creates, regardless of the numerical algorithm adopted, complex structures in the distribution function. In fact, boundaries in velocity space separating regions yielding different kinds of orbits display a fractal structure. This is a physical feature, overlooked in previous works on probe theory, that appears independently of the numerical strategy followed to compute the solution. Therefore, assessing the integrable or non-integrable character of the physical system under analysis is essential during the development of a stationary Vlasov-Poisson solver based on a backward Liouville method.

Integrable problems, such as the case of a cylindrical probe, admit using arc-length algorithms that computes solely the location of the empty-full boundaries of the distribution function rather than its value at every point of the velocity space grid. This solution is obviously beneficial from a computational point of view. On the contrary, in view of the filamented structure of the distribution function, the arc-length approach is non-feasible when the problem becomes non-integrable (e.g., elliptic probe). The distribution function must then be computed at every point of the mesh, which filters out the finest structures. The appearance of filamentation in abscence of azimuthal symmetry may also explain convergence issues that were detected in previous works [123] involving stationary VP solvers that overlooked this aspect.

Previous considerations are important for the definition of an optimum for N_{tr} (i.e., the numerical parameter that measures the number of loops around the probe after which a particle is deemed as trapped). For integrable configurations (i.e., round probes), if the numerical integrator has good conservation properties, a parametric analysis gradually increasing N_{tr} is recommendable. However, if the chosen integrator does not conserve the invariants exactly, increasing indefinitely N_{tr} would cause more particles that should be trapped to be deflected towards one of the boundaries of the computational domain in response to the accumulation of numerical errors. On the other hand, a too small N_{tr} would incorrectly classify as trapped particles that should not. Recalling that large values of N_{tr} increase the computational cost, a trade-off analysis is recommendable to select the optimum N_{tr}. When the configuration is non-integrable, the distribution function is filamented regardless of the numerical integrator used. Therefore, one might follow a similar trade-off procedure to the one described for the numerical integrator that does not conserve the energy applied to integrable configurations. In fact, a large value of N_{tr} would yield an overestimation of the density even when using energy-conserving propagators because trapped and non-trapped orbits are mixed in phase space.

Despite the above limitations, stationary Vlasov-Poisson solvers based on a backward Liouville method remain valuable for the numerical study of plasma-material interaction in a wide range of conditions, including those of interest for LWTs. Since most studies mainly focus on estimating the collected and emitted fluxes at the interface and the structure of the electrostatic potential, relatively rough tools like the FEM-RK solver combined with an unstructured mesh can perform well when complex geometries (beyond cylinders and ellipses) are considered. However, if a detailed and fine analysis of kinetic features

is sought for, then better-behaved algorithm like the FDM-CN solver coupled with structured meshes are preferable.

5.1.2 Parametric analysis of electron-emitting elliptical probes

The present section summarises the results of an extensive analysis that covered a wide range of plasma parameters representative of an ionospheric plasma, where the hypotheses of the OMT at the basis of the solver hold reasonably. While the code can address any two-dimensional configuration, the investigation focused on the characterization of the steady-state sheath around *elliptic* probes. In addition to representing *per se* a novel contribution, the elliptical geometry is a convenient choice from multiple points of views.

First, it represents the natural link between infinite prisms with round and tape cross-sections that can be recovered as limit cases when the eccentricity goes to 0 or 1, respectively. In the latter case, the results of this work are relevant for EDT devices. In particular, when electron-emission from the body is taken into account, the configuration resembles the cathodic segment of a LWT. Second, since the eccentricity of the ellipse acts as an integrability-breaking parameter, moving gradually from a cylindrical to an elliptical geometry triggers the appearance of fine structures in the velocity space distribution function that have a significant impact on the properties of the numerical algorithm, as discussed previously.

The analysis allowed to characterise the transitions of elliptical probes into different operational regimes (e.g., OML/non-OML current collection and SCL/non-SCL emission). In addition to probes for plasma diagnostics and EDTs, the findings can be relevant for fundamental studies regarding the interaction between non-spherical dust grains in plasma and plasma-sheath lenses. The characteristic dimension-to-Debye length ratio (b_p), the emission level (β) and the eccentricity (e_p) were the governing parameters that were varied during the study. A first set of results showed that the dependence of the macroscopic quantities on the azimuthal angle decreases with the size of the probe, while it is more pronounced for higher values of both the emission level and the eccentricity.

Regarding current collection, this proved to be particularly sensitive to the slenderness of the object. For a fixed set of parameters, the number of Γ-originated particles (i.e. orbits connecting to the plasma-probe interface when integrated backward in time) increases with e_p. When this overcomes a certain threshold, the collected current falls below the one predicted by the OML theory. It was shown that the critical value of the eccentricity at which the OML/non-OML transition occurs falls in the range $0.90 < e_p < 0.95$, in agreement with previous analytical results found for oblate spheroids in the Laplace limit [108]. A second comparison measuring the drop of current with that predicted by asymptotic analysis in the limit of high bias revealed that a high bias [94] mitigates the impact of the geometry of Γ on the collected current. For a fixed perimeter, the reduction in the collected current turned out to be more severe ($\approx 8\%$) for elliptical probes than for cyindrical one.

The above results were explained by highlighting a the strong correlation between the curvature of the plasma-material interface and the current distribution along its perimeter. Generally speaking, the higher the curvature, the more likely the current complies with the OML predictions, though the absolute minimum does not coincide with the point of minimum curvature (i.e., the semi-minor axis for an ellipse). In presence of electron emission, both the magnitude of the reduction in the current collection in non-OML conditions and its dependence with the eccentricity were shown to decrease. The range of validity of the OML theory is therefore enhanced in applications where emission plays a significant role (e.g., LWT devices), regardless of the shape of the plasma-material interface.

Finally, a parametric analysis varying the emission level for a certain configuration proved that a potential well develops gradually from the point of minimum curvature, which is the first to enter SCL conditions. A transitional regime where the ellipse is partially SCL follows, until the emission is so high that the whole surface emits under SCL conditions. A comparison with the current emitted by cylinders in the same conditions showed that ellipses in SCL conditions behaves like cylinders with radius equal to the semi-major axis. In relation to LWT-plasma interaction, this is an important result because it justifies using existing database of current-voltage characteristics for electron-emitting cylinders, which are much less costly to generate from a computational standpoint.

5.1.3 Emissive probes in non-stationary conditions

While the largest part of the analysis focuses on the investigation of the sheath around ellipses in stationary conditions, a second *semi-Lagrangian* software was developed for the investigation of non-stationary scenarios. In addition to greatly increasing the analysis capability, extending it for instance to configurations where the probe is in relative motion with respect to the background plasma, this second software can help understanding more deeply the impact of some of the hypotheses of the stationary model on the final solution. A relevant example is the role of the trapped population that cannot be taken into account in a stationary setting.

A comparison with the results of FONKS-C and CPIC obtained for a Langmuir cylindrical probe allowed to verify the correct implementation of the SLVP and provided an insight about the trapping mechanism and its effect on the structure of the plasma sheath and the current collection. A second analysis using the SLVP showed the influence of the electron emission on the population of trapped particles. The latter increases when electrons are emitted at the plasma-probe contour and current collection is enhanced accordingly. Due to the computational cost involved by using the semi-Lagrangian solver, these first analyses considered non-physical ions with mass equal to that of the electrons.

Taking advantage of the lower computational cost of CPIC, a more realistic analysis considering hydrogen ions was carried out in order to assess whether the above conclusions still hold. By gradually varying the emission level, it showed that the final population of trapped depends on the history of the system, with different initial conditions giving rise to different sheaths.The mass of the attracted species and the electron-emission

level also proved to have a deep impact on the final structure of the sheath. In particular, the population of trapped particles increases with the emission level and opposes the onset of the SCL regime. As a result, the drop in the emitted current is weaker than in the case when trapped particles are neglected. Regarding current collection, a similar growth to that obtained for the case of an electron-positron plasma was observed in the simulations.

5.2 Future activities

Both codes can be used to target additional scenarios relevant for LWTs devices and other space-related applications. Simulations involving configurations where electrons are emitted non-uniformly along the probe contour can be carried out with FONKS-G in order to measure the impact of a non-uniform emission on the behaviour of the object under SCL conditions. This would be extremely relevant for LWTs applications, since only part of the tether is exposed directly to the sunlight.

Regarding the novel backward semi-Lagrangian Vlasov-Poisson solver, the short-term objective is that of complementing its verification by a thorough comparison with the results obtained with CPIC for the case of an emissive cylindrical probe. Later, an extensive parametric analysis will be carried out to characterise deeply the impact of the trapped population on the characteristics of the sheath around electron-emitting objects. After reproducing the results already obtained with CPIC in order to assess the role of the numerical noise, the analysis will be extended in order to target

- A wider parametric space for cylindrical emissive probes in order to provide a better insight of the role of the trapped population on the non-SCL/SCL transition
- Objects with elliptic cross-sections. Similarly to what done for the stationary case, this will provide results that are more representative for LWTs applications
- Investigation of charging of cylindrical and elliptic electron-emitting objects immersed in Maxwellian plasmas. This could be of particular interest for applications regarding dusty plasmas.
- Extension of the model to configurations featuring flowing plasmas

Numerical simulations of some of these scenarios with CPIC is already on-going, and their results will be compared with numerical results from the Eulerian code.

Appendix A

Basic formulae for ellipses and circumferences

The parametric equations[1] of an ellipse of eccentricity e_p and semi-minor axis b_p are

$$x(\gamma) = \frac{b_p}{\sqrt{1-e_p^2}}\cos\gamma, \tag{A.1a}$$

$$y(\gamma) = b_p \sin\gamma, \tag{A.1b}$$

where γ is the *eccentric anomaly*. The arc-length measured from the x-axis is

$$s(\gamma) = b_p \int_0^{\gamma} \sqrt{\frac{\sin^2 t}{1-e_p^2} + \cos^2 t}\, dt. \tag{A.2}$$

Along the ellipse contour, the curvature is given by

$$\kappa(\gamma) = \frac{1-e_p^2}{b_p} \frac{1}{\left[\sin^2\gamma + (1-e_p^2)\cos^2\gamma\right]^{3/2}}. \tag{A.3}$$

For $e_p = 0$, equations (A.1)- (A.2)-(A.3) provide the parametrisation, the arc length and the curvature of a circumference of radius b_p. In this case, $\gamma \equiv \theta$ identifies the aziumuthal angle measured from the x-axis in the counter-clockwise direction.

[1] The content of this Appendix is adapted from the Appendix in Ref. [129]

Appendix B

Poisson Solver: numerical outer boundary condition

Following Ref. [123], we provide the explicit formulae for the computation of the coefficients appearing in Eq. (2.28). These are given by

$$A_0 = \frac{1}{2\pi}\int_0^{2\pi} \phi(r_{max},\theta)d\theta \approx \frac{1}{2\pi}\sum_{i=1}^{N_b} a_0^i \phi(r_{max}^i,\theta^i) \tag{B.1a}$$

$$A_n = \frac{1}{\pi}\int_0^{2\pi} \phi(r_{max},\theta)\cos n\theta d\theta \approx \frac{1}{2\pi}\sum_{i=1}^{N_b} a_n^i \phi(r_{max}^i,\theta^i) \tag{B.1b}$$

$$B_n = \frac{1}{\pi}\int_0^{2\pi} \phi(r_{max},\theta)\sin n\theta d\theta \approx \frac{1}{2\pi}\sum_{i=1}^{N_b} b_n^i \phi(r_{max}^i,\theta^i) \tag{B.1c}$$

where N_b represents the number of points at the outer boundary Γ_{max}, $n = 1,\ 2,\ \ldots,\ N_{modes}$ identifies the mode of the harmonic and the numerical coefficients a_0^i, a_n^i and b_n^i are computed at the i^{th}-node along the external boundary as

$$a_0^i = \frac{1}{2}[mod(\theta^{i+1}-\theta^i,2\pi)\ +\ mod(\theta^i-\theta^{i-1},2\pi)] \tag{B.2a}$$

$$a_n^i = \frac{\cos n\theta^i - \cos n\theta^{i-1}}{n^2 mod(\theta^i-\theta^{i-1},2\pi)} - \frac{\cos n\theta^{i+1} - \cos n\theta^i}{n^2 mod(\theta^{i+1}-\theta^i,2\pi)} \tag{B.2b}$$

$$b_n^i = \frac{\sin n\theta^i - \sin n\theta^{i-1}}{n^2 mod(\theta^i-\theta^{i-1},2\pi)} - \frac{\sin n\theta^{i+1} - \sin n\theta^i}{n^2 mod(\theta^{i+1}-\theta^i,2\pi)} \tag{B.2c}$$

with $mod(arg_1,arg_2)$ the remainder of the division arg_1/arg_2.

By definition [see Eqs. (2.22) and (2.26)] r_{max} is the same for all the nodes lying on Γ_{max} when the computational domain is discretised onto an unstructured Cartesian mesh or structured meshes in polar coordinates. In these cases, the numerical computation of the coefficients given in Eqs. (B.1) is straightforward. However, when structured elliptic meshes are used, the procedure is different. Although the higher the value of L_ξ, the more

the ellipse at the external boundary $\xi_{max} = L_\xi \xi_p$ resembles a circumference, the radial distance of the nodes lying on Γ_{max} varies along the outer boundary.

In order to be able to compute the coefficients of Eqs. (B.1), the algorithm defines an auxiliary *virtual* plasma boundary

$$\Gamma^v_{max} = \{(r,\theta) \mid r = b_{max},\ 0 \leq \theta \leq \pi/2\} \tag{B.3}$$

where b_{max} is the normalized semi-minor axis of the ellipse ξ_{max}. The red line in the left panel in Fig. B.1 identifies the virtual plasma boundary. The value of the potential at each of the node lying on it boundary is computed through bi-linear interpolation from the values at the nodes of the computational domain. The right panel in Fig. B.1 illustrates how the procedure works. After identifying the cell that contains the query point $P^i_q \in \Gamma^v_{max}$, the value of the electrostatic potential there is approximated as

$$\phi^i_q \approx \frac{\Delta\chi^i_p \Delta\eta^i_p \phi^i_1 - \Delta\chi^i_m \Delta\eta^i_p \phi^i_2 - \Delta\chi^i_p \Delta\eta^i_m \phi^i_3 + \Delta\chi^i_m \Delta\eta^i_m \phi^i_4}{(\Delta\chi^i_m + \Delta\chi^i_p)\,(\Delta\eta^i_m + \Delta\eta^i_p)}, \tag{B.4}$$

where the sub-indexes match the enumeration in the figure, while the super-index identifies the node along the boundary. Equation (B.4) applies for the $i = 2,\ 3,\ \ldots,\ N_b - 1$

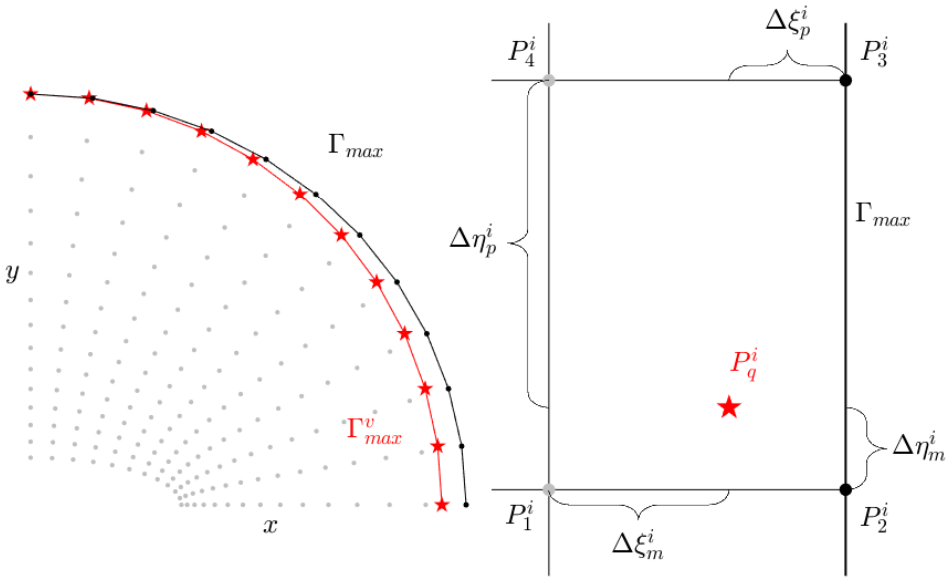

FIGURE B.1: Left: Elliptical mesh with plasma boundary Γ_{max} (solid black curve with dots) and virtual plasma boundary Γ^v_{max} (solid red curve with star) highlighted. Right: detail in the logical space (ξ, η) of the bi-linear interpolation procedure to compute the value of the potential at the i^{th}-node of the virtual plasma boundary.

internal nodes of the virtual plasma boundary Γ^v_{max}. At $(x,y) = (b_{max}, 0)$ the interpolation

reduces to a one-dimensional one in the ξ-direction

$$\phi_q^1 \approx \frac{\Delta\chi_p^1\phi_1^1 - \Delta\chi_m^1\phi_2^1}{(\Delta\chi_m^1 + \Delta\chi_p^1)}, \tag{B.5}$$

while $(x,y) = (b_{max}, \pi/2)$ the virtual plasma boundary coincides with Γ_{max} and no interpolation is needed. Once the procedure is completed along the entire virtual boundary, coefficients A_0, A_n and B_n can be computed by taking $\phi(r_{max}^i = b_{max}, \theta^i) = \phi_q^i$.

Appendix C

Numerical integrators

The present analysis considers three different algorithms[1] for the integration of the Vlasov characteristic equations. For every time step, the reconstruction of the electric field $\boldsymbol{E}$ from the values of the electrostatic potential at the nodes depends on the type of mesh (see Appendix D). The first integrator is an explicit time-adaptive *Runge-Kutta-Fehlberg* (RK) algorithm. Adapted from the corresponding function in Ref. [153], it is used indifferently for unstructured and structured meshes. In tandem with a finite difference (finite element) Poisson solver, it constitutes what is here referred to as FDM-RK (FEM-RK) solver (see Table 2.4).

A second-order (symplectic) *LeapFrog* (LF) scheme [153] can also be used for both types of discretisation, and therefore coupled with both the finite element and finite difference $\mathscr{P}$ to give the FEM-LF and FDM-LF solvers, respectively. The LF scheme was implemented in an attempt to improve the conservation properties of the numerical integrator, since the RK algorithm is known to be prone to energy drift. Nonetheless, results of the analysis of the conservation properties of the different schemes showed that the numerical integrator itself does not bring significant improvement of the conservation properties if an adequate reconstruction of the electric field is not achieved. In order to solve this problem and improve the conservation properties of the solver, a third integrator was implemented.

The latter is an implicit *Crank-Nicolson* (CN) scheme that was originally proposed for particle-in-cell applications [160, 163, 178]. Contrary to the RK and LF schemes, it is only used with curvilinear structured meshes. In fact, it is a hybrid integrator that integrates in time

$$\dot{\chi}^k = \boldsymbol{v} \cdot \boldsymbol{a}^k \quad k = 1,2 \tag{C.1a}$$

$$\dot{\boldsymbol{v}} = \frac{e_\alpha}{\delta_\alpha} \boldsymbol{E}. \tag{C.1b}$$

[1] The description of the numerical integrators is adapted from that provided in Appendix A.3 of Ref. [128]

From the equations above, one observes that the CN algorithm updates the position in the logical curvilinear space (χ^1, χ^2), while velocities are still updated in Cartesian space. As explained in detail in [160], this choice enhances the performances of the algorithm. In fact, updating the position in the logical makes the localization of a particle along its trajectory trivial, unlike what occurs when the unstructured meshes are used (see discussion at the end of Sec. D.2).

Using superscript ν and $\nu+1$ to identify the values of the variables at the instant $\tau = \tau_\nu$ and $\tau = \tau_\nu + \Delta\tau$, and defining the contravariant base vectors $\boldsymbol{a}^k = \nabla\chi^k$ and the covariant base vectors $\boldsymbol{a}_k = \partial\boldsymbol{r}/\partial\chi^k$ with $k = 1,\ 2$, the discrete form of Eqs. (C.1) according to the implicit CN scheme read

$$\frac{\chi^{k,\nu+1} - \chi^{k,\nu}}{\Delta\tau} = \boldsymbol{v}^{\nu+1/2} \cdot \boldsymbol{a}^{k,\nu+1/2} \quad k = 1,2 \tag{C.2a}$$

$$\frac{\boldsymbol{v}^{\nu+1} - \boldsymbol{v}^{\nu}}{\Delta\tau} = \frac{e_\alpha}{2\delta_\alpha} E_k^{\nu+1/2} \boldsymbol{a}^{k,\nu+1/2}, \tag{C.2b}$$

In Eqs. (C.2), Einstein summation convention was adopted and $\boldsymbol{v}^{\nu+1/2} = (\boldsymbol{v}^{\nu+1} + \boldsymbol{v}^{\nu})/2$, $\boldsymbol{a}^{k,\nu+1/2} = (\boldsymbol{a}^{k,\nu+1} + \boldsymbol{a}^{k,\nu})/2$. The computation of the covariant electric field components $E_k = \boldsymbol{E} \cdot \boldsymbol{a}_k$ is described in Appendix D, and it is an adaptation of the procedure described in Ref. [160] to the two-dimensional, stationary problem addressed in the present analysis.

C.1 Criterion for trapped particles

As explained in Sec. 2.2.3, a particle is classified as trapped if its orbit does not connect with neither Γ nor Γ_{max} after carrying out N_{tr} full revolutions about the origin of the computational domain. In order to stop the integration when the latter condition is satisfied, the numerical integrator updates the angular displacement according to

$$\theta^{\nu+1} = \theta^{\nu} + \omega^{\nu} \cdot \Delta\tau, \tag{C.3}$$

with

$$\omega^{\nu} = \frac{-v_x^{\nu} y^{\nu} + v_y^{\nu} x^{\nu}}{(x^{\nu} + y^{\nu})^2}. \tag{C.4}$$

Setting $\theta^0 = 0$, the integration is stopped at $\tau = \tau_f$, when it holds that $\theta^f \geq 2\pi \cdot N_{tr}$. The role of the numerical parameter N_{tr}, which can impact significantly the accuracy and the performances of the algorithm, is discussed in detail in Sec. 3.2.1.2.

Appendix D

Reconstruction of the electric field

From Eq. (2.38b) it appears clear that, regardless the scheme implemented, an algorithm that computes the value of the electric field at any point contained in the computational domain from the value of the electrostatic potential profile at the nodes of the mesh is necessary. The different strategies to reconstruct the gradient of the potential along the orbits are described in detail in the following sections[1].

D.1 Unstructured meshes

For unstructured meshes, two different strategies were implemented in the code. Consistently with the approximation of Eq. (2.30), a first option involves assuming the value of the electric field as constant within the each triangular element. From the point of view of the computational cost, this is a convenient choice and it also allows for the analytical computation of the trajectory (see tracking algorithm in Ref. [123]). However, the outcome is a piece-wise constant electric field whose discontinuities might introduce significant numerical errors in the integration of the particle trajectories if the size of the elements is not small enough where the magnitude of the gradient becomes large.

Alternatively, one can build a piece-wise polynomial approximation of the electric field across the domain. At each node (x_0, y_0), this is done by first computing the second order polynomial

$$\begin{aligned}\phi_f(x,y) - \phi(x_0,y_0) &= c_f^1(x-x_0) + c_f^2(y-y_0) + \\ &+ c_f^3(x-x_0)^2 + c_f^4(y-y_0)^2 + c_f^5(x-x_0)(y-y_0),\end{aligned} \tag{D.1}$$

that best fits (in the least-square sense [153]) the electrostatic potential profile locally. In order to obtain the coefficients appearing in the equation above, it is necessary to solve

[1] The description of the strategies for the reconstruction of the electric field is adapted from that provided in Appendix A.3 of Ref. [128]

numerically the system of equations

$$\bar{\boldsymbol{G}}_f^T \, \bar{\boldsymbol{G}}_f \, \boldsymbol{c}_f = \bar{\boldsymbol{G}}_f^T \, \boldsymbol{b}_f \tag{D.2}$$

with matrix $\bar{\boldsymbol{G}}_f \in \mathscr{R}^{N_f \times 5}$ and vector $\boldsymbol{b}_f \in \mathscr{R}^{N_f}$ defined as

$$\bar{\boldsymbol{G}}_f \equiv \begin{bmatrix} \Delta x_1 & \Delta y_1 & \Delta x_1^2 & \Delta y_1^2 & \Delta x_1 \cdot \Delta y_1 \\ \vdots & \vdots & \vdots & \vdots & \vdots \\ \Delta x_i & \Delta y_i & \Delta x_i^2 & \Delta y_i^2 & \Delta x_i \cdot \Delta y_i \\ \vdots & \vdots & \vdots & \vdots & \vdots \\ \Delta x_{N_f} & \Delta y_{N_f} & \Delta x_{N_f}^2 & \Delta y_{N_f}^2 & \Delta x_{N_f} \cdot \Delta y_{N_f} \end{bmatrix}, \quad \boldsymbol{b}_f \equiv \begin{Bmatrix} \Delta\phi_1 \\ \vdots \\ \Delta\phi_i \\ \vdots \\ \Delta\phi_{N_f} \end{Bmatrix}. \tag{D.3}$$

In the equations above, $\Delta x_i = x_i - x_0$, $\Delta y_i = y_i - y_0$, $\Delta\phi_i = \phi_i - \phi_0$, with sub-index $i = 1,\ldots,N_f$ identifies the quantities computed at the i^{th}-node connected with the node of interest (x_0, y_0). A second-order polynomial like that of Eq. (D.1) requires $N_f \geq 5$. In the eventuality that a given node does not present a sufficient amount of direct connections (e.g., nodes at the boundaries of the computational domain), the code takes into account an additional number of $5 - N_f$ nodes, selected in order of proximity to the one of interest.

Once the polynomial ϕ_f is obtained, the value of the electric field at the nodes of mesh is obtained through analytic derivation. The components of the electric field are then gathered at a generic point along an orbit through interpolation from the values at the nodes. To this purpose, a *natural neighbor interpolation* scheme [179] is used, which is particularly suitable for unstructured meshes and guarantees a smoother reconstruction of the electric field with respect to the piece-wise constant representation previously discussed.

D.1.1 Tracking procedure

Regardless of the technique implemented, the computation of the gradient requires first identifying in which element of the mesh the particle is located at any time step. To this purpose, it is convenient to define the barycentric coordinates of the query point (x_q, y_q), which identifies the position of the orbit at a given time step, as

$$\lambda_1^q = \frac{(y_2 - y_3)\cdot(xq - x_3) + (x_3 - x_2)\cdot(yq - y_3)}{2\Delta^{elm}}, \tag{D.4a}$$

$$\lambda_2^q = \frac{(y_1 - y_3)\cdot(xq - x_3) + (x_3 - x_1)\cdot(yq - y_3)}{2\Delta^{elm}}, \tag{D.4b}$$

$$\lambda_3^q = 1 - (\lambda_1^q + \lambda_2^q), \tag{D.4c}$$

with sub-indexes identifying the vertexes of the triangle in counter-clockwise order, and Δ^{elm} defined in Eq. (2.31). Geometrically, (x_q, y_q) lies inside the triangular element as long as $\lambda_i^q \geq 0$ for $i = 1,2,3$. Since the typical number of elements used for discretising

a domain is of the order $\sim 10^{3-4}$, evaluating the above-mentioned condition at each elements is computationally expensive. In order to improve the efficiency of the localization algorithm, the code exploits the information of the position of the particle at the previous step and the information about the connectivity of the elements in order to lower the number of times the above condition is assessed. In the pre-processing phase, for each element, the code defines subsequently higher level *patches* (i.e., a lists of elements that share with an element a node or a face). This information is then used during the numerical integration of the characteristics to identify the location of the particle at a certain time.

A graphical representation of the localization procedure is shown in Fig. D.1. At a given time step, the code checks whether the particle is still inside the element elm_0 in which it was lying at the previous time step (black triangle in Fig. D.1). If the outcome is negative, the algorithm scans the 1^{st}-level patch of triangles confining with the element of interest (magenta triangles in Fig. D.1). If the query point is still not found, the codes scans the 2^{nd}-level patch (i.e., cyan triangles) and so on. This recursive procedure terminates once the particle is localised within a certain triangle. Since the time step adopted is relatively small, the localization procedure takes place onto a limited area of the computational domain, which is convenient from a computational point of view.

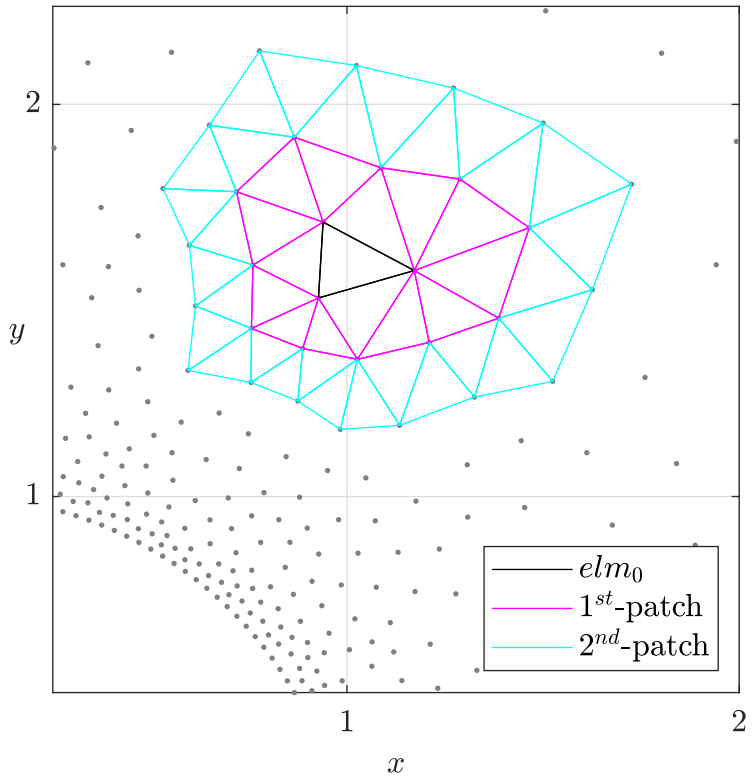

FIGURE D.1: Localization procedure for an orbit integrated onto an unstructured mesh.

D.2 Structured meshes

Similarly to the previous case, the code implements two alternative strategies for reconstructing the electric field along the orbits when structured meshes are used. The first one involves approximating the values of the electric field at the nodes of the mesh through second-order finite differences. The centred scheme of Eqs. (2.34b)-(2.37) is applied for the internal nodes, while a *forward* ($^+$) and a *backward* ($^-$) schemes are used at the inner and outer boundary of the computational domain, respectively. For a generic distribution of nodes, one has the following approximations

$$\left.\frac{\partial\phi}{\partial r}\right|_{i,j} \approx \frac{1}{D^+}\left[-\frac{1}{Q^+}\phi_{i+2,j}+\left(\frac{1}{Q^+}+2+Q^+\right)\phi_{i+1,j}-(Q^++2)\phi_{i,j}\right], \tag{D.5a}$$

$$\left.\frac{\partial\phi}{\partial r}\right|_{i,j} \approx \frac{1}{D^-}\left[(Q^-+2)\phi_{i,j}-\left(Q^-+2+\frac{1}{Q^-}\right)\phi_{i-1,j}+\frac{1}{Q^-}\phi_{i-2,j}\right], \tag{D.5b}$$

where gradients along r were taken as example and the coefficients are defined as

$$Q^+ \equiv \frac{\Delta r_{i+2}}{\Delta r_{i+1}}, \quad D^+ \equiv \Delta r_{i+2}+\Delta r_{i+1}, \tag{D.6a}$$

$$Q^- \equiv \frac{\Delta r_{i-1}}{\Delta r_i}, \quad D^- \equiv \Delta r_{i-1}+\Delta r_i. \tag{D.6b}$$

Similarly to what discussed for the centred scheme in Sec. 2.2.2.2, in case the nodes along the direction of interested are uniformly distributed ($\Delta r_i = \Delta r_{i+1} = \Delta r$), the coefficients become $Q^+ = Q^- = 1$, $D^+ = D^- = 2\Delta r$, resulting in

$$\left.\frac{\partial\phi}{\partial r}\right|_{i,j} \approx \frac{-\phi_{i+2,j}+4\phi_{i+1,j}-3\phi_{i,j}}{2\Delta r}, \tag{D.7a}$$

$$\left.\frac{\partial\phi}{\partial r}\right|_{i,j} \approx \frac{3\phi_{i,j}-4\phi_{i-1,j}+\phi_{i-2,j}}{2\Delta r}. \tag{D.7b}$$

Once the gradient is known at the nodes of the computational domain, *bi-linear interpolation* [153] is then applied in order to provide an estimation of the electric field along the orbit. This requires identifying previously where the particle is located. For structured meshes, this operation is straightforward and, at the time step τ_ν, the computational cell $[\chi^1_{i^\nu}, \chi^1_{i^\nu+1}] \times [\chi^2_{j^\nu}, \chi^2_{j^\nu+1}]$ in which the particle lies is found through

$$i^\nu = 1 + floor\left(\frac{\chi^{1,\nu}-\chi^1_1}{\Delta\chi^1}\right), \quad j^\nu = 1 + floor\left(\frac{\chi^{2,\nu}-\chi^2_1}{\Delta\chi^2}\right), \tag{D.8}$$

with $floor()$ a built-in function in Fortran returning the less or equal integer to its argument.

The same localization procedure is applied when the gradient along the orbit is computed through *B-spline* interpolation. This alternative strategy was adapted from the algorithm presented in [160] to the stationary, two-dimensional problem addressed here. For convenience, the following treatment describes the case for a uniform mesh (i.e., $\Delta\chi^k \equiv \chi_i^k - \chi_{i+1}^k = \chi_i^k - \chi_{i-1}^k = constant$, with $k = 1,2$). In addition, integer sub-indexes (i,j) and semi-integer sub-indexes $(i+1/2, j+1/2)$ to denote quantities computed at the faces and centres of the grid cells, respectively, with

$$\chi_{i+1/2}^k = \frac{\chi_i^k + \chi_{i+1}^k}{2}, \quad k = 1,2,\ i = 1,\ldots,N_{\chi^k} \tag{D.9}$$

The code computes the electric field at the *faces* of each cells from the values of the electrostatic potential profile at the centres of the two cells sharing that face. The latter is obtained as the mean values of ϕ at the vertices of the cell as

$$\phi_{i+1/2,j+1/2}^c = \frac{\phi_{i,j} + \phi_{i+1,j} + \phi_{i,j+1} + \phi_{i+1,j+1}}{4}. \tag{D.10}$$

The values of the electric field at the faces (i.e., at the nodes of the computational grid) are then found from

$$E_{\chi^1,(i,j)} = -\frac{\phi_{i+1/2,j+1/2}^c - \phi_{i-1/2,j+1/2}^c}{\Delta\chi_i^1}, \tag{D.11a}$$

$$E_{\chi^2,(i,j)} = -\frac{\phi_{i+1/2,j+1/2}^c - \phi_{i+1/2,j-1/2}^c}{\Delta\chi_j^2}. \tag{D.11b}$$

The B-spline shape functions are then gathered into vectors

$$\boldsymbol{S}_1^{\chi^k} = \left\{ \begin{array}{c} 1 - \left(\frac{\chi^{k,\nu_h} - \chi_{i^{\nu_h}}^k}{\Delta\chi^k} \right) \\ \\ \left(\frac{\chi^{k,\nu_h} - \chi_{i^{\nu_h}}^k}{\Delta\chi^k} \right) \end{array} \right\}^T, \quad \boldsymbol{S}_2^{\chi^{k,\nu}} = \left\{ \begin{array}{c} \frac{1}{2}\left[\frac{1}{2} - \left(\frac{\chi^{k,\nu} - \chi_{i^{\nu}-1/2}^k}{\Delta\chi^k} \right) \right]^2 \\ \\ \left[\frac{3}{4} - \left(\frac{\chi^{k,\nu} - \chi_{i^{\nu}-1/2}^k}{\Delta\chi^k} \right) \right]^2 \\ \\ \frac{1}{2}\left[\frac{1}{2} + \left(\frac{\chi^{k,\nu} - \chi_{i^{\nu}-1/2}^k}{\Delta\chi^k} \right) \right]^2 \end{array} \right\} \tag{D.12}$$

where super-scripts ν, ν_p and ν_h denote quantities computed at times $\tau_{\nu_p} = \tau_{\nu+1} = \tau_\nu + \Delta\tau$ and $\tau_{\nu_h} = \tau_{\nu+1/2} = 0.5(\tau_\nu + \tau_{\nu+1})$, respectively. After defining the matrix

$$\bar{\boldsymbol{E}}_k^{\nu_h,\nu} \equiv \left[\begin{array}{ccc} E_{k,i^{\nu_h}-1,j^\nu-1} & E_{k,i^{\nu_h}-1,j^\nu} & E_{k,i^{\nu_h}-1,j^\nu+1} \\ \\ E_{k,i^{\nu_h},j^\nu-1} & E_{k,i^{\nu_h},j^\nu} & E_{k,i^{\nu_h},j^\nu+1} \end{array} \right] \tag{D.13}$$

the components of the electric field at point $(\chi^{1,\nu_h}, \chi^{2,\nu_h})$ [see right-hand-side of Eq. (C.2b)] are

$$E_1^{\nu_h} = \frac{1}{2}\left(\boldsymbol{S}_1^{\chi^1} \cdot \bar{\boldsymbol{E}}_1^{\nu_h,\nu} \cdot \boldsymbol{S}_2^{\chi^{2,\nu}} + \boldsymbol{S}_1^{\chi^1} \cdot \bar{\boldsymbol{E}}_1^{\nu_h,\nu_p} \cdot \boldsymbol{S}_2^{\chi^{2,\nu_p}} \right), \tag{D.14}$$

$$E_2^{\nu_h} = \frac{1}{2}\left(\boldsymbol{S}_1^{\chi^2} \cdot \bar{\boldsymbol{E}}_2^{\nu_h,\nu} \cdot \boldsymbol{S}_2^{\chi^{1,\nu}} + \boldsymbol{S}_1^{\chi^2} \cdot \bar{\boldsymbol{E}}_2^{\nu_h,\nu_p} \cdot \boldsymbol{S}_2^{\chi^{1,\nu_p}} \right). \tag{D.15}$$

Regarding the boundary conditions along χ^1, these are imposed by adding *ghost cells* inside Γ and outside Γ_{max}. At these locations, the value of the electrostatic potential profile is computed through quadratic extrapolation in χ^1 for each value of χ^2. For convenience, Table D.1 summarises the different strategies implemented for the reconstruction of the electric field.

Mesh	$\boldsymbol{E}$ reconstruction
Unstructured	Piecewise constant [123]
Unstructured	Polynomial fitting + Natural neighbor interpolation [179]
Structured	FDM + Bilinear interpolation [153]
Structured	B-spline [160]

TABLE D.1: Summary of the different algorithms for the reconstruction of the electric field.

Appendix E

Tikhonov regularization procedure

Since the problem is ill-conditioned, updating the solution according to the simple Newton-Raphson map of Eq. (2.53) might yield convergence issues. Therefore, the stationary Eulerian solver presented in Chapter 2 implements a *progressive Tikhonov regularisation*. Since a detailed explanation of the latter is found in Ref. [123] and references therein, the following description provides only a summary of the various steps that the algorithm follows in order to update the space charge density vector.

Let us start by re-writing the Newton map as the generic linear system

$$\bar{\boldsymbol{A}}\,\boldsymbol{x} = \boldsymbol{b} \tag{E.1}$$

where $\bar{\boldsymbol{A}}$ coincides with the $N \times N$ Jacobian matrix $\boldsymbol{J}|_{\boldsymbol{\rho}_n}$, $\boldsymbol{x} = \boldsymbol{\rho}_{n+1} - \boldsymbol{\rho}_n$ and the right-hand-side (RHS) vector $\boldsymbol{b}$ is equal to $\boldsymbol{G}(\boldsymbol{\rho}_n)$. A first reduction of the condition number of matrix $\bar{\boldsymbol{A}}$ is obtained by applying the right diagonal preconditioning

$$\underbrace{\bar{\boldsymbol{A}}\,\bar{\boldsymbol{D}}}_{\bar{\boldsymbol{A}}'}\,\underbrace{(\bar{\boldsymbol{D}}^{-1}\,\boldsymbol{x})}_{\boldsymbol{x}'} = \boldsymbol{b}, \tag{E.2}$$

where $\bar{\boldsymbol{D}}$ is a $N \times N$ diagonal matrix whose elements are given by

$$D(i,j) = \begin{cases} \frac{1}{\|\bar{\boldsymbol{D}}(:,i)\|_2} & j = i \\ 0 & j \neq i \end{cases} \tag{E.3}$$

Since the diagonal preconditioning is not, in general, sufficient to prevent the amplification of numerical errors in the computation of the RHS, the algorithm implements a Tikhonov regularisation. Using singular value decomposition [153], one obtains $\bar{\boldsymbol{A}}' = \bar{\boldsymbol{U}}\,\mathrm{diag}\{\boldsymbol{\sigma}\}\,\bar{\boldsymbol{V}}^T$, where $\bar{\boldsymbol{U}}$ and $\bar{\boldsymbol{V}}$ are $N \times N$ orthogonal matrixes and $\mathrm{diag}\{\boldsymbol{\sigma}\}$ is a diagnoal matrix whose elements correspond to the singular values of $\bar{\boldsymbol{A}}'$. Substituting into Eq. (E.2)

gives

$$\mathrm{diag}\{\boldsymbol{\sigma}\}\ \underbrace{\bar{\boldsymbol{V}}^T\boldsymbol{x}}_{\tilde{\boldsymbol{x}}} = \underbrace{\bar{\boldsymbol{U}}^T\boldsymbol{b}}_{\tilde{\boldsymbol{b}}}. \tag{E.4}$$

Since $\mathrm{diag}\{\boldsymbol{\sigma}\}$ is diagonal, the components of the unknown vector $\tilde{\boldsymbol{x}}$ are

$$\tilde{x}_i = \frac{\tilde{b}_i}{\sigma_i}, \quad i = 1,2,\ldots,N. \tag{E.5}$$

However, if $\bar{\boldsymbol{A}}'$ is ill-conditioned, some of its singular values can be extremely small, resulting in a magnification of the numerical errors affecting vector $\tilde{\boldsymbol{b}}$. To avoid this issue, the algorithm applies the *low-pass* filter

$$\tilde{x}_i = \frac{\sigma_i}{\sigma_i^2 + \lambda^2}\,\tilde{b}_i, \tag{E.6}$$

which prevents singular values smaller than the Tikhonov parameter λ to affect the solution. The optimal λ is selected such that $\|\boldsymbol{b}\|_2$ is halved at each iteration. Following Ref. [123], one has

$$\sum_{i=1}^{N} \frac{\lambda^4}{(\sigma_i^2 + \lambda^2)^2}\,\tilde{b}_i = \frac{1}{4}\sum_{i=1}^{N}\tilde{b}_i, \tag{E.7}$$

which, in the present implementation, is solved numerically with a bi-section method. Once the optimal Tikhonov parameter is found, the unknown vector is obtained

$$\boldsymbol{\rho}_{n+1} - \boldsymbol{\rho}_n = \boldsymbol{x} = \bar{\boldsymbol{D}}\,\bar{\boldsymbol{V}}\,\tilde{\boldsymbol{x}}, \tag{E.8}$$

with $\tilde{\boldsymbol{x}}$ computed according to Eq. (E.6).

Appendix F

CIC Interpolation module

Since it provides the evolution in time of the distribution function, the interpolation module is a key aspect in a semi-Lagrangian backward scheme. The first version of the present algorithm implements the so-called *cloud-in-cell* (CIC) method [180]. In a n-dimensional phase space, each cell of the discrete Eulerian grid is identified by an hyperrectangle of dimension n with sides $[a^h, b^h]|_{h=1}^{n}$, with a^h and b^h the limits of the cell along the h-dimension. Together with the vertices of such hyperrectangle, the query point x_q^h (i.e., the origin of the characteristic) at which one wants to compute the unknown distribution function divides the cell into 2^n sub-hyperrectangles. The CIC model assigns to each vertex of the cell a weight equal to the ratio between the volume of the sub-hyperrectangle opposite to it and the total volume of the cell in the phase space. In the presental analysis we have $n = 4$. After defining the variables

$$\Delta x^h \equiv b_h - a_h, \tag{F.1}$$

$$w_q^h \equiv \frac{\{x_q^h - a_h,\ b_h - x_q^h\}}{\Delta x^h} \tag{F.2}$$

$$\tag{F.3}$$

the interpolated value at the query point is given by

$$f_q = \sum_{i,j,k,l=1}^{2} f_{i,j,k,l} \cdot w_q^{i,j,k,l}, \tag{F.4}$$

$$w_q^{i,j,k,l} = \prod_{h=1}^{4} w_q^h(ii^h), \quad ii^h = mod(i^h, 2) + 1 \tag{F.5}$$

where $f^{i,j,k,l}$ and $w_q^{i,j,k,l}$ identify the value of the distribution function and the weight associated with the vertices of the hyperrectangle. In Eq. (F.5), $mod(i^h, 2)$ is the remainder of the ratio $i^h/2$ and i^h identifying the vertex along the h-dimension (i.e., $i^1 = i$, $i^2 = j$, etc..).

Figure F.1 shows the corresponding representation for the simplified case of a 1D-1V phase space. Once normalized to the total area of the cell, areas of different colours identify the weight associated to the sample of the distribution function corresponding to the node denoted by the round marker of the same colour. In other words, the purple area

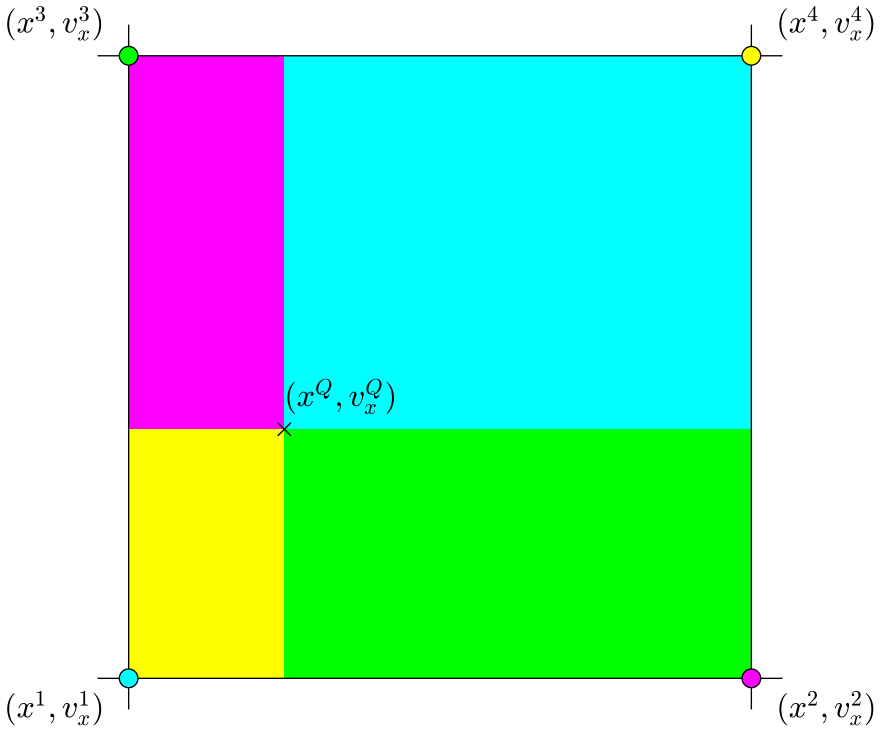

FIGURE F.1: Cloud-in-cell interpolation in two-dimensional phase space.

Bibliography

[1] Arthur P. Cracknell and Costas A. Varotsos. Editorial and cover: Fifty years after the first artificial satellite: from sputnik 1 to envisat. *International Journal of Remote Sensing*, 28(10):2071–2072, 2007.

[2] V.D. Kuznetsov, V.M. Sinelnikov, and S.N. Alpert. Yakov alpert: Sputnik-1 and the first satellite ionospheric experiment. *Advances in Space Research*, 55(12):2833–2839, 2015.

[3] ESA Space Debris Office. Esa's annual space environment report. Technical Report GEN-DB-LOG-00288-OPS-SD, European Space Agency, Darmstadt, Germany, April 2022.

[4] H. Stokes, Y. Akahoshi, C. Bonnal, R. Destefanis, Y. Gu, A. Kato, A. Kutomanov, A. LaCroix, S. Lemmens, A. Lohvynenko, D. Oltrogge, P. Omaly, J. Opiela, H. Quan, K. Sato, M. Sorge, and M. Tang. Evolution of iso's space debris mitigation standards. *Journal of Space Safety Engineering*, 7(3):325–331, 2020. Space Debris: The State of Art.

[5] Iadc space debris mitigation guidelines. Technical Report IADC-02-01 Rev. 3, Inter-Agency Space Debris Coordination Committee, 2021.

[6] Donald J. Kessler and Burton G. Cour-Palais. Collision frequency of artificial satellites: The creation of a debris belt. *Journal of Geophysical Research: Space Physics*, 83(A6):2637–2646, 1978.

[7] J.C Liou, Anilkumar A K, Benjamin Virgili, Toshiya Hanada, Holger Krag, Hugh Lewis, M. Raj, M Rao, A Rossi, and Ram Sharma. Stability of the future leo environment – an iadc comparison study. 04 2013.

[8] A. C. Boley and M. Byers. Satellite mega-constellations create risks in low earth orbit, the atmosphere and on earth. *Scientific Reports*, 11(1):10642, 2021.

[9] C. Priyant Mark and Surekha Kamath. Review of active space debris removal methods. *Space Policy*, 47:194–206, 2019.

[10] P. Zhao, J. Liu, and C. Wu. Survey on research and development of on-orbit active debris removal methods. *Science China Technological Sciences*, 63(11):1869–1900, 2020.

[11] Robert L. Forward, Robert P. Hoyt, and Chauncey W. Uphoff. Terminator tether: A spacecraft deorbit device. *Journal of Spacecraft and Rockets*, 37(2):187–196, 2000.

[12] Satomi Kawamoto, Takeshi Makida, Fumiki Sasaki, Yasushi Okawa, and Shin ichiro Nishida. Precise numerical simulations of electrodynamic tethers for an active debris removal system. *Acta Astronautica*, 59(1):139–148, 2006. Space for Inspiration of Humankind, Selected Proceedings of the 56th International Astronautical Federation Congress, Fukuoka, Japan, 17-21 October 2005.

[13] C. Pardini, T. Hanada, and P. H. Krisko. Benefits and risks of using electrodynamic tethers to de-orbit spacecraft. *Acta Astronautica*, 64(5):571–588, 2009.

[14] Juan R. Sanmartin, Enrico C. Lorenzini, and Manuel Martinez-Sanchez. Electrodynamic tether applications and constraints. *Journal of Spacecraft and Rockets*, 47(3):442–456, 2010.

[15] Juan Sanmartin, Shaker Khan, Claudio Bombardelli, Enrico Lorenzini, Giacomo Colombatti, D. Zanutto, J.-F Roussel, Pierre Sarrailh, J.D. Williams, Garrett Metz, J.K. Thomas, Jose Carrasco, Francisco Garcia de Quiros, O. Kroemer, R. Rosta, T. Zoest, J. Lasa, and J. Marcos. Propellantless deorbiting of space debris by bare electrodynamic tethers. *62nd International Astronautical Congress 2011, IAC 2011*, 3:2239–2248, 01 2011.

[16] Changqing Wang, Gangqiang Li, Zheng H. Zhu, and Aijun Li. Mass ratio of electrodynamic tether to spacecraft on deorbit stability and efficiency. *Journal of Guidance, Control, and Dynamics*, 39(9):2192–2198, 2016.

[17] G. Sánchez-Arriaga, J.R. Sanmartín, and E.C. Lorenzini. Comparison of technologies for deorbiting spacecraft from low-earth-orbit at end of mission. *Acta Astronautica*, 138:536–542, 2017. The Fifth International Conference on Tethers in Space.

[18] S. Drell, H. Foley, and M. A. Ruderman. Drag and propulsion of large satellites in the ionosphere: An alfvén propulsion engine in space. *Journal of Geophysical Research*, 70:3131–3145, 1965.

[19] G. Parks. *Physics Of Space Plasmas: An Introduction, Second Edition*. Avalon Publishing, 2003.

[20] G. Sánchez-Arriaga. Course on electrodynamic tethers. https://uc3m-phd-aerospace.es/course-on-electrodynamic-tethers/. Accessed: 2022-01-01.

[21] Irwin E. Vas, Thomas J. Kelly, and Ethan A. Scarl. Space station reboost with electrodynamic tethers. *Journal of Spacecraft and Rockets*, 37(2):154–164, 2000.

[22] Les Johnson, Joe Carroll, Robert Estes, Enrico Lorenzini, Brian Gilchrist, Manuel Martinez-Sanchez, Juan Sanmartin, and Irwin Vas. *Electrodynamic tethers for reboost of the International Space Station and spacecraft propulsion*.

[23] J. R. Sanmartin, M. Charro, J. Pelaez, I. Tinao, S. Elaskar, A. Hilgers, and M. Martinez-Sanchez. Floating bare tether as upper atmosphere probe. *Journal of Geophysical Research: Space Physics*, 111(A11), 2006.

[24] G. Sánchez-Arriaga and J.R. Sanmartín. Electrical model and optimal design scheme for low work-function tethers in thrust mode. *Aerospace Science and Technology*, 96:105519, 2020.

[25] Yanfang Li, Aijun Li, Changqing Wang, and Haochang Tian. Dynamic analysis and libration control of electrodynamic tether for reboost applications. *IEEE Access*, 9:77894–77904, 2021.

[26] Peter Yao and Timothy Sands. Micro satellite orbital boost by electrodynamic tethers. *Micromachines*, 12(8), 2021.

[27] G. Sánchez-Arriaga, S. Naghdi, K. Wätzig, J. Schilm, E.C. Lorenzini, M. Tajmar, E. Urgoiti, L. Tarabini Castellani, J.F. Plaza, and A. Post. The e.t.pack project: Towards a fully passive and consumable-less deorbit kit based on low-work-function tether technology. *Acta Astronautica*, 177:821–827, 2020.

[28] R. Moore. *The geomagnetic thrustor - A high performance "Alfven wave"propulsion system utilizing plasma contacts*. 1996.

[29] J. R. Sanmartin, M. Martinez-Sanchez, and E. Ahedo. Bare wire anodes for electrodynamic tethers. *Journal of Propulsion and Power*, 9(3):353–360, 1993.

[30] J. D. Williams, J. R. Sanmartin, and L. P. Rand. Low work-function coating for an entirely propellantless bare electrodynamic tether. *IEEE Transactions on Plasma Science*, 40(5):1441–1445, 2012.

[31] J. R. Sanmartín, Xin Chen, and G. Sánchez-Arriaga. Analysis of thermionic bare tether operation regimes in passive mode. *Physics of Plasmas*, 24(1):013515, 2017.

[32] Xin Chen and J. R. Sanmartín. Bare-tether cathodic contact through thermionic emission by low-work-function materials. *Physics of Plasmas*, 19(7):073508, 2012.

[33] G. Sanchez-Arriaga and Xin Chen. Modeling and performance of electrodynamic low-work-function tethers with photoemission effects. *Journal of Propulsion and Power*, 34(1):213–220, 2018.

[34] Gonzalo Sánchez-Arriaga, Gabriel Borderes-Motta, and Luca Chiabó. A code for the analysis of missions with electrodynamic tethers. *Acta Astronautica*, 198:471–481, 2022.

[35] M. Tajmar and G. Sánchez-Arriaga. A bare-photovoltaic tether for consumableless and autonomous space propulsion and power generation. *Acta Astronautica*, 180:350–360, 2021.

[36] J.M. Grimwood, B.C. Hacker, and P.J. Vorzimmer. *Project Gemini: Technology and Operations: A Chronology*. NASA SP. Scientific and Technical Information Division, National Aeronautics and Space Administration, 1969.

[37] M. van Pelt. *Space Tethers and Space Elevators*. Springer New York, 2009.

[38] Yi Chen, Rui Huang, Xianlin Ren, Liping He, and Ye He. History of the tether concept and tether missions: A review. *ISRN Astronomy and Astrophysics*, 2013, 2013.

[39] Kenneth J. Szalai, Carlo Bonifazi, Paul Joyce, Robert J. Schwinghamer, Robert White, Kenneth D. Bowersox, William Charles Schneider, John H. Stadler, and David W. Whittle. Tss-1r mission failure investigation board. 1996.

[40] Nobie Stone. *Electrodynamic characteristics of the Tethered Satellite System during the TSS-1R mission*.

[41] D. C. Thompson, C. Bonifazi, B. E. Gilchrist, S. D. Williams, W. J. Raitt, J.-P. Lebreton, W. J. Burke, N. H. Stone, and K. H. Wright Jr. The current-voltage characteristics of a large probe in low earth orbit: Tss-1r results. *Geophysical Research Letters*, 25(4):413–416, 1998.

[42] S. D. Williams, B. E. Gilchrist, V. M. Agüero, R. S. Indiresan, D. C. Thompson, and W. J. Raitt. Tss-1r vertical electric fields: Long baseline measurements using an electrodynamic tether as a double probe. *Geophysical Research Letters*, 25(4):445–448, 1998.

[43] N.H. Stone, W.J. Raitt, and K.H. Wright. The tss-1r electrodynamic tether experiment: Scientific and technological results. *Advances in Space Research*, 24(8):1037–1045, 1999. Active Experiments in Space Plasmas.

[44] Victor M. Aguero, Brian E. Gilchrist, Scott D. Williams, William J. Burke, Linda Krause, and Louise C. Gentile. Current collection model characterizing shuttle charging during the tethered satellite system missions. *Journal of Spacecraft and Rockets*, 37(2):212–217, 2000.

[45] Nobie H. Stone. Unique results and lessons learned from the tss missions. 2016.

[46] Chung-Jen Chang. Electrodynamic behavior of pmg-delta. Technical report, NAVAL POSTGRADUATE SCHOOL MONTEREY CA, 1994.

[47] Mario D. Grossi. Plasma Motor Generator (PMG) electrodynamic tether experiment. Final Report, 15 Sep. 1992 - 30 Sep. 1995 Smithsonian Astrophysical Observatory, Cambridge, MA., June 1995.

[48] Joseph A. Carroll and J. C. Oldson. Tethers for small satellite applications. 1995.

[49] Thomas L. Wilson, Dean Chlouber, and R. Jerry Jost. Electrodynamic tether currents in the day/night ionosphere: Correlations during the plasma motor generator mission. *Journal of Geophysical Research: Space Physics*, 101(A10):21657–21688, 1996.

[50] Les Johnson, Robert David Estes, Enrico C. Lorenzini, Manual Martinez-Sanchez, and J. R. Sanmartín. Propulsive small expendable deployer system experiment. *Journal of Spacecraft and Rockets*, 37:173–176, 2000.

[51] Les Johnson, Brian Gilchrist, Enrico Lorenzini, Nobie Stone, and Ken Wright. *Propulsive Small Expendable Deployer System (ProSEDS) Experiment: Mission Overview & Status*.

[52] Jason Vaughn, Leslie Curtis, Brian Gilchrist, Sven Bilen, and Enrico Lorenzini. *Review of the ProSEDS Electrodynamic Tether Mission Development*.

[53] Hironori A. Fujii, Takeo Watanabe, Hirohisa Kojima, Koh-Ichiro Oyama, Tairo Kusagaya, Yoshiki Yamagiwa, Hirotaka Ohtsu, Mengu Cho, Susumu Sasaki, Koji Tanaka, John Williams, Binyamin Rubin, Charles Les Johnson, George Khazanov, Juan R. Sanmartin, Jean-Pierre Lebreton, Erick J. van der Heide, Michiel Kruijff, Fabio De Pascal, and Pavel M. Trivailo. Sounding rocket experiment of bare electrodynamic tether system. *Acta Astronautica*, 64(2):313–324, 2009.

[54] L. Tarabini Castellani, A. Ortega, A. Giménez, E. Urgoiti, G. Sánchez-Arriaga, G. Borderes-Motta, E.C. Lorenzini, M. Tajmar, K. Wätzig, A. Post, and J.F. Plaza. Low work-function tether deorbit kit. *Journal of Space Safety Engineering*, 7(3):332–339, 2020. Space Debris: The State of Art.

[55] Zheng Hong Zhu. *Mission Design for a CubeSat Deorbit Experiment Using an Electrodynamic Tether*.

[56] Iverson C. Bell, Brian E. Gilchrist, Jesse K. McTernan, and Sven G. Bilén. Investigating miniaturized electrodynamic tethers for picosatellites and femtosatellites. *Journal of Spacecraft and Rockets*, 54(1):55–66, 2017.

[57] Udai Bindra, Latheepan Murugathasan, Vidushi Jain, Gangqiang Li, Junjie Kang, Chonggang Du, Zheng Hong Zhu, Franz T. Newland, Mike Alger, Oluwatayo Shonibare, and Anton de Ruiter. *DESCENT: Mission Architecture and Design Overview*.

[58] Gunter D. Krebs. Tepce 1, 2. https://space.skyrocket.de/doc_dat/tepce.htm. Accessed: 2022-01-01.

[59] Sven Bilen. Space tethers to demonstrate propellantless propulsion, deorbiting satellites. https://aerospaceamerica.aiaa.org/year-in-review/space-tethers-to-demonstrate-propellantless-propulsion-deorbiting-satellites/. Accessed: 2022-01-01.

[60] Sven Bilen. Tethers demonstrate propellantless propulsion in low-earth orbit. https://aerospaceamerica.aiaa.org/year-in-review/tethers-demonstrate-propellantless-propulsion-in-low-earth-orbit/. Accessed: 2022-01-01.

[61] Caleb Henry. Tethers unlimited says early results of deorbit hardware test promising. https://spacenews.com/tethers-unlimited-says-early-results-of-deorbit-hardware-test-promising/. Accessed: 2022-01-01.

[62] ESA Earth Observational Portal. Tepce (tether electrodynamics propulsion cubesat experiment). https://eoportal.org/web/eoportal/satellite-missions/content%20/-/article/tepce, 2020. Accessed: 2022-01-01.

[63] Debra Werner. Dragracer to demonstrate the value of tethers for satellite deorbit. https://spacenews.com/dragracer-to-demonstrate-the-value-of-tethers-for-satellite-deorbit/. Accessed: 2022-05-27.

[64] Debra Werner. Electrodynamic tethers speed up satellite reenty timelines. https://spacenews.com/tethers-unlimited-terminator-tape-smallsat-2021/. Accessed: 2022-05-27.

[65] Sven Bilen. Space tethers demonstrate deorbit capability. https://aerospaceamerica.aiaa.org/year-in-review/space-tethers-demonstrate-deorbit-capability/. Accessed: 2022-01-01.

[66] S. Coffey et al. Tepce: A tethered electrodynamic propulsion cubesat experiment. Technical report, U.S. Naval Research Laboratory, Washington, DC, February 2022.

[67] Sven Bilen, Jesse McTernan, Brian Gilchrist, Iverson Bell, Nestor Voronka, and Robert Hoyt. *Electrodynamic Tethers for Energy Harvesting and Propulsion on Space Platforms*.

[68] R. Mantellato, L. Olivieri, and E.C. Lorenzini. Study of dynamical stability of tethered systems during space tug maneuvers. *Acta Astronautica*, 138:559–569, 2017. The Fifth International Conference on Tethers in Space.

[69] Gangqiang Li and Zheng H. Zhu. Multiphysics finite element modeling of current generation of bare flexible electrodynamic tether. *Journal of Propulsion and Power*, 33(2):408–419, 2017.

[70] Scott Robertson. Sheaths in laboratory and space plasmas. *Plasma Physics and Controlled Fusion*, 55(9):093001, jul 2013.

[71] Scott D Baalrud, Brett Scheiner, Benjamin T Yee, Matthew M Hopkins, and Edward Barnat. Interaction of biased electrodes and plasmas: sheaths, double layers, and fireballs. *Plasma Sources Science and Technology*, 29(5):053001, may 2020.

[72] Juan Ramón Sanmartín, Eric Choinière, Brian E. Gilchrist, Jean-Benoit Ferry, and Manuel Martínez-Sánchez. Bare-tether sheath and current: comparison of asymptotic theory and kinetic simulations in stationary plasma. *IEEE Transactionc on Plasma Science*, 36(5):2851–2858, 2008.

[73] P Sarrailh, JF Roussel, JM Siguier, V Inguimbert, G Murat, and J SanMartin. Leo drifting plasma collection by a positive biased tether wire: Time-dependant simulations using spis. In *Proc. 12th Spacecraft Charging Technol. Conf.*, 2012.

[74] John A. Janeski, Wayne A. Scales, and Christopher D. Hall. Investigation of the current collected by a positively biased satellite with application to electrodynamic tethers. *Journal of Geophysical Research: Space Physics*, 119(9):7824–7840, 2014.

[75] J. P. Sheehan, E. V. Barnat, B. R. Weatherford, I. D. Kaganovich, and N. Hershkowitz. Emissive sheath measurements in the afterglow of a radio frequency plasma. *Physics of Plasmas*, 21(1):013510, 2014.

[76] V. A. Godyak and B. M. Alexandrovich. Comparative analyses of plasma probe diagnostics techniques. *Journal of Applied Physics*, 118(23):233302, 2015.

[77] Codrina Ionita, Bernd Sebastian Schneider, Stefan Costea, Ovidiu Vasilovici, Jernej Kovacic, Tomaz Gyergyek, Volker Naulin, Jens Juul Rasmussen, Nicola Vianello, Monica Spolaore, Ronald Starz, and Roman Schrittwieser. Plasma potential probes for hot plasmas. *The European Physical Journal D*, 73(4):73, Apr 2019.

[78] V. I. Demidov, M. E. Koepke, I. P. Kurlyandskaya, and M. A. Malkov. Basic factors for acquiring, correcting, and interpreting probe current-voltage characteristic in moderate-collisional plasma for determining electron energy distribution. *Physics of Plasmas*, 27(2):020501, 2020.

[79] Chi-Shung Yip, Chenyao Jin, Wei Zhang, Guo Sheng Xu, and Noah Hershkowitz. Experimental investigation of sheath effects on i-v traces of strongly electron emitting probes. *Plasma Sources Science Technology*, 29(2):025025, February 2020.

[80] Akinola Olowookere and Richard Marchand. Fixed bias probe measurement of a satellite floating potential. *IEEE Transactions on Plasma Science*, 49(2):862–870, 2021.

[81] Z Jílek, J Čaloud, P Zikán, A Obrusník, and D Trunec. PIC/MC calculation of current–voltage characteristic of emissive probe. *Plasma Sources Science and Technology*, 31(3):035014, mar 2022.

[82] G. L. Delzanno, G. Lapenta, and M. Rosenberg. Attractive potential around a thermionically emitting microparticle. *Phys. Rev. Lett.*, 92:035002, Jan 2004.

[83] Xian-Zhu Tang and Gian Luca Delzanno. Orbital-motion-limited theory of dust charging and plasma response. *Physics of Plasmas*, 21(12):123708, 2014.

[84] Gian Luca Delzanno and Xian-Zhu Tang. Charging and heat collection by a positively charged dust grain in a plasma. *Phys. Rev. Lett.*, 113:035002, Jul 2014.

[85] S. L. G. Hess, P. Sarrailh, J.-C. Matéo-Vélez, B. Jeanty-Ruard, F. Cipriani, J. Forest, A. Hilgers, F. Honary, B. Thiébault, S. R. Marple, and D. Rodgers. New spis capabilities to simulate dust electrostatic charging, transport, and contamination of lunar probes. *IEEE Transactions on Plasma Science*, 43(9):2799–2807, Sep. 2015.

[86] Pierre Sarrailh, Jean-Charles Matéo-Vélez, Sébastien L. G. Hess, Jean-François Roussel, Benoit Thiébault, Julien Forest, Benjamin Jeanty-Ruard, Alain Hilgers, David Rodgers, Fabrice Cipriani, and Denis Payan. Spis 5: New modeling capabilities and methods for scientific missions. *IEEE Transactions on Plasma Science*, 43(9):2789–2798, 2015.

[87] Benoit Thiébault, Benjamin Jeanty-Ruard, Pierre Souquet, Julien Forest, Jean-Charles Matéo-Vélez, Pierre Sarrailh, David Rodgers, Alain Hilgers, Fabrice Cipriani, Denis Payan, and Nicolas Balcon. Spis 5.1: An innovative approach for spacecraft plasma modeling. *IEEE Transactions on Plasma Science*, 43(9):2782–2788, Sep. 2015.

[88] Johansson, F. L., Eriksson, A. I., Gilet, N., Henri, P., Wattieaux, G., Taylor, M. G. G. T., Imhof, C., and Cipriani, F. A charging model for the rosetta spacecraft. *A&A*, 642:A43, 2020.

[89] Kai Zhang, Shiying Cai, Chunpei Cai, and David L. Cooke. A parallel particle-in-cell code for spacecraft charging problems. *Journal of Plasma Physics*, 86(3):905860308, 2020.

[90] J. A. Bittencourt. *Fundamentals of Plasma Physics*. Fundamentals of Plasma Physics, Third Edition by J.A. Bittencourt. Published by Springer-Verlag, New York, Inc.; 2004. ISBN 0-387-20975-1., third edition, 2004.

[91] J E Allen, R L F Boyd, and P Reynolds. The collection of positive ions by a probe immersed in a plasma. *Proceedings of the Physical Society. Section B*, 70(3):297–304, mar 1957.

[92] Ira B. Bernstein and Irving N. Rabinowitz. Theory of electrostatic probes in a low-density plasma. *Phys. Fluids*, 2(2):112–121, 1959.

[93] J. G. Laframboise. *Theory of Spherical and Cylindrical Langmuir Probes in a Collisionless, Maxwellian Plasma at Rest.* PhD thesis, University of Toronto (Canada)., 1966.

[94] J. R. Sanmartín and R. D. Estes. The orbital-motion-limited regime of cylindrical langmuir probes. *Phys. Plasmas*, 6(1):395–405, 1999.

[95] M. Y. Ye and S. Takamura. Effect of space-charge limited emission on measurements of plasma potential using emissive probes. *Physics of Plasmas*, 7(8):3457–3463, 2000.

[96] S. Takamura, N. Ohno, M. Y. Ye, and T. Kuwabara. Space-charge limited current from plasma-facing material surface. *Contributions to Plasma Physics*, 44(1-3):126–137, 2004.

[97] G. L. Delzanno, A. Bruno, G. Sorasio, and G. Lapenta. Exact orbital motion theory of the shielding potential around an emitting, spherical body. *Physics of Plasmas*, 12(6):062102, 2005.

[98] Lorin S. Matthews and Truell W. Hyde. Charging and growth of fractal dust grains. *IEEE Transactions on Plasma Science*, 36(1):310–314, 2008.

[99] Scott Robertson. Reformulation of laframboise' probe theory in cylindrical geometry and the absence of an ion saturation current. *IEEE Transactions on Plasma Science*, 38(4):781–787, 2010.

[100] Scott Robertson. The electron sheath around an emissive wire in vacuum. *IEEE Transactions on Plasma Science*, 40(10):2678–2685, 2012.

[101] C. T. N. Willis, M. Coppins, M. Bacharis, and J. E. Allen. Floating potential of large dust grains in a collisionless flowing plasma. *Phys. Rev. E*, 85:036403, Mar 2012.

[102] A. Autricque, S. A. Khrapak, L. Couëdel, N. Fedorczak, C. Arnas, J.-M. Layet, and C. Grisolia. Electron collection and thermionic emission from a spherical dust grain in the space-charge limited regime. *Physics of Plasmas*, 25(6):063701, 2018.

[103] N. Rizopoulou and M. Bacharis. Emitting large dust grains: Floating potential and potential wells. *Physics of Plasmas*, 25(6):063703, 2018.

[104] Joseph I. Samaniego, Xu Wang, and Scott Robertson. Sheath around a spherical probe in a photoelectron environment. *IEEE Transactions on Plasma Science*, 48(2):418–425, 2020.

[105] L. Schiesko, D. Wünderlich, and I. M. Montellano. Kinetic sheath in presence of multiple positive ions, negative ions, and particle wall emission. *Journal of Applied Physics*, 127(3):033302, 2020.

[106] Giulia Sarego, Lorenzo Olivieri, Andrea Valmorbida, Alice Brunello, Enrico C. Lorenzini, Lorenzo Tarabini Castellani, Eduardo Urgoiti, Asier Ortega, Gabriel Borderes-Motta, and Gonzalo Sánchez-Arriaga. Deployment requirements for deorbiting electrodynamic tether technology. *CEAS Space Journal*, 13:567–581, 2021.

[107] H. M. Mott-Smith and Irving Langmuir. The theory of collectors in gaseous discharges. *Phys. Rev.*, 28:727–763, Oct 1926.

[108] J. G. Laframboise and L. W. Parker. Probe design for orbit-limited current collection. *Phys. Fluids*, 16(5):629–636, 1973.

[109] R. D. Estes and J. R. Sanmartín. Cylindrical langmuir probes beyond the orbital-motion-limited regime. *Physics of Plasmas*, 7(10):4320–4325, 2000.

[110] Kuo Wei Chang and George K. Bienkowski. Effects of electron emission on electrostatic probes at arbitrary pressures. *The Physics of Fluids*, 13(4):902–920, 1970.

[111] A. Fruchtman, D. Zoler, and G. Makrinich. Potential of an emissive cylindrical probe in plasma. *Phys. Rev. E*, 84:025402, Aug 2011.

[112] J. P. Sheehan, Yevgeny Raitses, Noah Hershkowitz, and Michael McDonald. Recommended practice for use of emissive probes in electric propulsion testing. *Journal of Propulsion and Power*, 33(3):614–637, 2017.

[113] Xin Chen and G. Sanchez-Arriaga. Orbital motion theory and operational regimes for cylindrical emissive probes. *Phys. Plasmas*, 24(2):023504, 2017.

[114] Shaker Bayajid Khan and Juan R. Sanmartin. Survival probability of round and tape tethers against debris impact. *Journal of Spacecraft and Rockets*, 50(3):603–608, 2013.

[115] Shaker Bayajid Khan, A. Francesconi, C. Giacomuzzo, and E.C. Lorenzini. Survivability to orbital debris of tape tethers for end-of-life spacecraft de-orbiting. *Aerospace Science and Technology*, 52:167–172, 2016.

[116] A. Francesconi, C. Giacomuzzo, L. Bettiol, and E. Lorenzini. A new ballistic limit equation for thin tape tethers. *Acta Astronautica*, 129:325–334, 2016.

[117] J.R. Sanmartín, A. Sánchez-Torres, S.B. Khan, G. Sánchez-Arriaga, and M. Charro. Optimum sizing of bare-tape tethers for de-orbiting satellites at end of mission. *Advances in Space Research*, 56(7):1485 – 1492, 2015.

[118] P. M. Bellan. Why interstellar ice dust grains should be elongated. *The Astrophysical Journal*, 905(2):96, dec 2020.

[119] E. Stamate and H. Sugai. Modal focusing effect of positive and negative ions by a three-dimensional plasma-sheath lens. *Phys. Rev. Lett.*, 94:125004, Apr 2005.

[120] E. Stamate and H. Sugai. Discrete focusing effect of positive ions by a plasma-sheath lens. *Phys. Rev. E*, 72:036407, Sep 2005.

[121] E Stamate. Discrete and modal focusing effects: principles and applications. *Plasma Physics and Controlled Fusion*, 54(12):124048, nov 2012.

[122] J. R. Sanmartín and R. D. Estes. Interference of parallel cylindrical langmuir probes. *Physics of Plasmas*, 8(9):4234–4239, 2001.

[123] E. Choiniere. Theory and experimental evaluation of a consistent steady-state kinetic model for 2-d conductive structures in ionospheric plasmas with application to bare electrodynamic tethers in space, 2004.

[124] W. J. Miloch, S. V. Vladimirov, H. L. Pécseli, and J. Trulsen. Numerical simulations of potential distribution for elongated insulating dust being charged by drifting plasmas. *Phys. Rev. E*, 78:036411, Sep 2008.

[125] J. T. Holgate and M. Coppins. Charging of nonspherical macroparticles in a plasma. *Phys. Rev. E*, 93:033208, Mar 2016.

[126] D M Thomas and J T Holgate. A treecode to simulate dust–plasma interactions. *Plasma Physics and Controlled Fusion*, 59(2):025002, dec 2016.

[127] Xin Chen and G. Sanchez-Arriaga. Kinetic features of collisionless sheaths around polarized cylindrical emitters from the orbital motion theory. *Physics of Plasmas*, 24(10):103515, 2017.

[128] L. Chiabó and G. Sánchez-Arriaga. Limitations of stationary vlasov-poisson solvers in probe theory. *Journal of Computational Physics*, 438:110366, 2021.

[129] L. Chiabó, S. Shahsavani, and G. Sánchez-Arriaga. Kinetic analysis of the plasma sheath around an electron-emitting object with elliptic cross section. *Phys. Rev. E*, 104:055204, Nov 2021.

[130] Richard Marchand. Test-particle simulation of space plasmas. *Communications in Computational Physics*, 8(3):471–483, 2010.

[131] V.L. Pisacane. *The Space Environment and Its Effects on Space Systems*. AIAA education series. American Institute of Aeronautics and Astronautics, 2008.

[132] Francis Chen. *Introduction to Plasma Physics and Controlled Fusion*. 01 2016.

[133] P. et al. Alken. International geomagnetic reference field: the thirteenth generation. *Earth, Planets and Space*, 73(1), 2021.

[134] G. V. Khazanov, N. H. Stone, E. N. Krivorutsky, and M. W. Liemohn. Current-produced magnetic field effects on current collection. *Journal of Geophysical Research: Space Physics*, 105(A7):15835–15842, 2000.

[135] G. V. Khazanov, N. H. Stone, E. N. Krivorutsky, K. V. Gamayunov, and M. W. Liemohn. Current-induced magnetic field effects on bare tether current collection: A parametric study. *Journal of Geophysical Research: Space Physics*, 106(A6):10565–10579, 2001.

[136] J. R. Sanmartín and R. D. Estes. Magnetic self-field effects on current collection by an ionospheric bare tether. *Journal of Geophysical Research: Space Physics*, 107(A11):SIA 2–1–SIA 2–7, 2002.

[137] R.C. Tolman. *The Principles of Statistical Mechanics*. Dover Books on Physics. Dover Publications, 1979.

[138] J P Verboncoeur. Particle simulation of plasmas: review and advances. *Plasma Physics and Controlled Fusion*, 47(5A):A231–A260, apr 2005.

[139] D. Tskhakaya, K. Matyash, R. Schneider, and F. Taccogna. The particle-in-cell method. *Contributions to Plasma Physics*, 47(8-9):563–594, 2007.

[140] Gianpiero Colonna and Antonio D'Angola, editors. *Plasma Modeling*. 2053-2563. IOP Publishing, 2016.

[141] F. Filbet and E. Sonnendrücker. Comparison of eulerian vlasov solvers. *Comput. Phys. Commun.*, 150(3):247 – 266, 2003.

[142] M. Shoucri. Eulerian codes for the numerical solution of the vlasov equation. *Communications in Nonlinear Science and Numerical Simulation*, 13(1):174 – 182, 2008.

[143] M. Shoucri, editor. *Eulerian Codes for the Numerical Solution of the Kinetic Equations of Plasmas*. Nova Science Publishers Inc, 2010.

[144] Alexander J Klimas. A method for overcoming the velocity space filamentation problem in collisionless plasma model solutions. *J. Comput. Phys.*, 68(1):202 – 226, 1987.

[145] J Candy and RE Waltz. An Eulerian gyrokinetic-Maxwell solver. *J. Comput. Phys.*, 186(2):545–581, 2003.

[146] A. Ghizzo, F. Huot, and P. Bertrand. A non-periodic 2d semi-lagrangian vlasov code for laser–plasma interaction on parallel computer. *J. Comput. Phys.*, 186(1):47 – 69, 2003.

[147] M. Shoucri, H. Gerhauser, and K. H. Finken. Oscillations of the collisionless sheath at grazing incidence of the magnetic field. *Phys. Plasmas*, 16(10), 2009.

[148] Takayuki Umeda, Jun-ichiro Miwa, Yosuke Matsumoto, Takuma K. M. Nakamura, Kentaro Togano, Keiichiro Fukazawa, and Iku Shinohara. Full electromagnetic vlasov code simulation of the kelvin–helmholtz instability. *Phys. Plasmas*, 17(5):052311, 2010.

[149] E. Camporeale, G.L. Delzanno, B.K. Bergen, and J.D. Moulton. On the velocity space discretization for the vlasov–poisson system: Comparison between implicit hermite spectral and particle-in-cell methods. *Comput. Phys. Commun.*, 198:47 – 58, 2016.

[150] Götz Lehmann. Efficient semi-lagrangian vlasov-maxwell simulations of high order harmonic generation from relativistic laser-plasma interactions. *Commun. Comput. Phys.*, 20(3):583–602, 2016.

[151] G. Sanchez-Arriaga, J. Zhou, E. Ahedo, M. Martinez-Sanchez, and J. J. Ramos. Kinetic features and non-stationary electron trapping in paraxial magnetic nozzles. *Plasma Source Science & Technology*, 27(3), 2018.

[152] Stephen J. Chapman. *Fortran 90/95 for Scientists and Engineers*. McGraw-Hill, Inc., USA, 2 edition, 2003.

[153] William H. Press, Saul A. Teukolsky, William T. Vetterling, and Brian P. Flannery. *Numerical Recipes in FORTRAN (2nd Ed.): The Art of Scientific Computing*. Cambridge University Press, USA, 1992.

[154] Numerical recipes home page. http://numerical.recipes/. Accessed: 2022-01-13.

[155] William Gropp, Ewing Lusk, and Anthony Skjellum. *Using MPI: Portable Parallel Programming with the Message-Passing Interface*. The MIT Press, 2014.

[156] Mpich home page. https://www.mpich.org/. Accessed: 2022-01-13.

[157] Quincey Koziol. *HDF5*, pages 827–833. Springer US, Boston, MA, 2011.

[158] Hdf5 home page. https://www.hdfgroup.org/solutions/hdf5/. Accessed: 2022-01-13.

[159] Geuzaine, Christophe and Remacle, Jean-Francois. Gmsh.

[160] L. Chacón and G. Chen. A curvilinear, fully implicit, conservative electromagnetic pic algorithm in multiple dimensions. *Journal of Computational Physics*, 316:578 – 597, 2016.

[161] J E Allen. Probe theory - the orbital motion approach. *Physica Scripta*, 45(5):497–503, may 1992.

[162] S Shahsavani, X Chen, and G Sanchez-Arriaga. Parametrization of current–voltage characteristics and operation domains of cylindrical emissive probes in collisionless maxwellian plasmas at rest. *Plasma Physics and Controlled Fusion*, 63(11):115018, oct 2021.

[163] G. L. Delzanno, E. Camporeale, J. D. Moulton, J. E. Borovsky, E. A. MacDonald, and M. F. Thomsen. Cpic: A curvilinear particle-in-cell code for plasma–material interaction studies. *IEEE Transactions on Plasma Science*, 41(12):3577–3587, 2013.

[164] L. Chiabò and G. Sánchez-Arriaga. Limitations of stationary vlasov-poisson solvers in probe theory (dataset), 2020.

[165] V. Pletnev and J. G. Laframboise. Current collection by a cylindrical probe in a partly ionized, collisional plasma. *Phys. Plasmas*, 13(7):073503, 2006.

[166] G. Sánchez-Arriaga. A direct vlasov code to study the non-stationary current collection by a cylindrical langmuir probe. *Phys. Plasmas*, 20(1):013504, 2013.

[167] M. Martinez-Sanchez, J. Navarro-Cavallé, and E. Ahedo. Electron cooling and finite potential drop in a magnetized plasma expansion. *Phys. Plasmas*, 22(5):053501, 2015.

[168] J. R. Sanmartín. *CNES-Space Technology Course: Prevention of Risks Related to Spacecraft Charging*. Edited by J.P. Catani (Cepadus, Toulouse, France), 2002.

[169] G. Sánchez-Arriaga and D. Pastor-Moreno. Direct vlasov simulations of electron-attracting cylindrical langmuir probes in flowing plasmas. *Phys. Plasmas*, 21(7):073504, 2014.

[170] A V Gurevich. Distribution of captured particles in a potential well in the absence of collisions. *Zh. Eksp. Teor. Fiz., 53: 953-64(Sept. 1967).*, 1 1967.

[171] A. A. Kiselyov, M. S. Dolgonosov, and V. L. Krasovsky. Formation of trapped-ion population in the process of charging of an absorbing sphere in a collisionless plasma. *EPL*, 111(1), JUL 2015.

[172] Victor L. Krasovsky and Alexander A. Kiselyov. On trapped-particle effect on shielding in collisionless plasmas. *IEEE Transactions on Plasma Science*, 46(3):631–635, 2018.

[173] Eric Sonnendrücker, Jean Roche, Pierre Bertrand, and Alain Ghizzo. The semi-lagrangian method for the numerical resolution of the vlasov equation. *Journal of Computational Physics*, 149(2):201–220, 1999.

[174] Minna Palmroth, Urs Ganse, Yann Pfau-Kempf, Markus Battarbee, Lucile Turc, Thiago Brito, Maxime Grandin, Sanni Hoilijoki, Arto Sandroos, and Sebastian von Alfthan. Vlasov methods in space physics and astrophysics. *Living Reviews in Computational Astrophysics*, 4, 2018.

[175] Lukas Einkemmer. A performance comparison of semi-lagrangian discontinuous galerkin and spline based vlasov solvers in four dimensions. *Journal of Computational Physics*, 376:937–951, 2019.

[176] Denis Lorenzon, Sergio A. Elaskar, and Andrés M. Cimino. Numerical simulations using eulerian schemes for the vlasov–poisson model. *International Journal of Computational Methods*, 18(09):2150031, 2021.

[177] Jacob Williams. jacobwilliams/bspline-fortran: 7.0.0, February 2022.

[178] L. Chacón, G. Chen, and D.C. Barnes. A charge- and energy-conserving implicit, electrostatic particle-in-cell algorithm on mapped computational meshes. *Journal of Computational Physics*, 233:1 – 9, 2013.

[179] Robin Sibson. *Interpolating Multivariate Data*. Chichester: John Wiley, 1981.

[180] Charles K. Birdsall and A. Bruce Langdon. *Plasma physics via computer simulation*. Taylor and Francis, New York, 2005.